



Bachelor's Thesis

XFLOW - CFD Analysis of the A350-900 Temperature Control System

Submitted by: Michael Fürweger

Registration Number: 1010587010

Supervisors: Dr. Martin Schmid (Airbus Operations GmbH Hamburg)
Dipl.-Ing. (FH) Christian Kussmann (qpunkt GmbH)
FH-Prof. Priv.-Doz. Dr.rer.nat. Wolfgang Hassler
(FH Joanneum Graz)

Date of Submission: 17th, September 2013

Affidavit

I hereby affirm in lieu of an oath that the present bachelor's thesis entitled
"XFLOW - CFD Analysis of the A350-900 Temperature Control System"

has been written by myself without the use of any other resources than those indicated and quoted.

Graz, 17th September 2013

Michael Fürweger

Preface

This thesis was written during my internships at qpunkt GmbH Graz and Airbus Operations GmbH Hamburg. I had a great time in Graz and also in Hamburg, where I probably found one of the greatest places to live at, apart from the bad weather in northern Germany. I would like to express my gratitude to both parties for offering me the necessary resources and supporting me while increasing my knowledge. Especially, I would like to thank my supervisors Martin and Christian for their patience in answering my questions.

Also I would like to thank my family for supporting the internship abroad and of course many thanks to Ursi for visiting me twice and calling me all the time to shorten the time without you. I miss you!

I am looking forward to finishing my Bachelor's degree at the FH-Joanneum. Thank you Wolfgang for supervising also my second Bachelor's thesis and for THE correction of my mistakes.

Hamburg, July 2013

Contents

| | |
|---|-----|
| Abstract | v |
| Kurzfassung | vi |
| List of Figures | vii |
| List of Abbreviations | x |
| 1 Introduction | 1 |
| 2 Methods | 3 |
| 2.1 Introduction to XFLOW | 3 |
| 2.1.1 The Maxwell-Boltzmann Distribution Function | 5 |
| 2.1.2 The Boltzmann Equation | 6 |
| 2.1.3 The Lattice for the Lattice Boltzmann Method | 8 |
| 2.2 XFLOW and The Command Line | 10 |
| 3 CFD Investigation | 11 |
| 3.1 Test Case - Thermal Mixing in a T-Junction Pipe | 11 |
| 3.1.1 Geometry and Setup | 12 |
| 3.1.2 Results of T-Junction Investigation | 14 |
| 3.1.3 Summary of T-Junction Investigation | 28 |
| 3.2 Investigation of Trim Tapping Design | 28 |
| 3.2.1 Geometry and Setup | 28 |
| 3.2.2 Results of Trim Tapping Design Investigation | 29 |
| 3.2.3 Summary of Trim Tapping Investigation | 32 |
| 3.3 Investigation of the TCS | 33 |
| 3.3.1 Geometry and Setup | 33 |
| 3.3.2 Hardware Issues and Cluster Problems | 35 |
| 4 Results | 36 |
| 4.1 TZ 1 | 38 |
| 4.2 TZ 2 | 41 |
| 4.3 TZ 3 (non humidified) | 43 |
| 4.4 TZ 4 | 49 |
| 4.5 TZ 5 | 52 |
| 4.6 TZ 6 | 54 |
| 4.7 TZ 7 | 57 |
| 4.8 Flight Crew Rest Compartment (FCRC) | 59 |
| 4.9 Cabin Crew Rest Compartment (CCRC) | 62 |
| 4.10 Flight Deck (F/D) | 63 |
| 4.11 Summary of Results | 65 |
| 4.12 Mixing Devices | 67 |

| | |
|--|-----------|
| 4.12.1 TZ 3 with Mixing Device | 68 |
| 4.13 Remark on Results | 70 |
| 5 Discussion | 76 |
| 6 Summary and Outlook | 77 |
| References/Bibliography | 78 |

Abstract

The temperature control system is a vital and complex system for safety and comfort of passengers in aircraft. For the new Airbus A350-900 this system is investigated in terms of thermal mixing. It is important for the regulation of the system that the temperature sensors are located in areas where cold and injected hot air is mixed properly. Only if the correct temperature is measured inside the temperature control system the cabin temperature can be regulated precisely for passenger comfort.

Thermal mixing at high Reynold numbers and for non-stationary flow in complex geometry is a difficult task for Computational Fluid Dynamics (CFD) software. This case seems to be well-suited for benchmarking of new software like XFLOW. XFLOW is a discrete, particle Lattice Boltzmann Method (LBM) based CFD software with promising appearance on distributed computation performance with Large Eddy Simulation (LES). Also promising is the applicability on complex geometries because manual meshing is no longer necessary.

This thesis describes the underlying principles of the LBM and contains a standard T-junction thermal mixing test-case with comparison to experimental results for XFLOW validation. Further, it is depicted how the current design of the temperature control system performs in terms of thermal mixing and where possibilities for improvements are.

Kurzfassung

Das Temperatur Control System (TCS) stellt einen wichtigen Bestandteil eines Flugzeugs dar, indem es für Sicherheit und Wohlbefinden von Crew und Passagieren sorgt. Das TCS des neuen Airbus A350-900 wird hinsichtlich der Performance von thermischer Mischung untersucht. Um die Kabinentemperatur überhaupt regeln zu können ist es wichtig, dass die Temperatursensoren innerhalb des TCS verlässliche Werte liefern. Dafür muss garantiert sein, dass die Sensoren an repräsentativen Stellen im TCS platziert sind, wo kalte und zugemischte heiße Luft ausreichend durchmischt sind.

Simulationen von thermischer Mischung bei instationären Strömungen mit hohen Reynolds-Zahlen in komplexen Geometrien stellen Computational Fluid Dynamics (CFD) Software vor große Herausforderungen. Grund genug, diesen Fall als Benchmark für neuartige Software wie XFLOW zu verwenden. XFLOW ist eine diskrete, auf Lattice Boltzmann Methoden (LBM) basierende CFD Software, welche sehr vielversprechend im Hinblick auf Performance bei verteilten Simulationen am Cluster und bei komplexen Geometrien scheint. Weiter wird die notwendige Zeit zum Aufsetzen von Simulationen minimiert, da manuelle Vernetzung nicht mehr nötig ist.

In dieser Arbeit werden die grundlegenden Gleichungen der LBM erläutert, bevor anhand eines standard Testfalles thermische Mischung mit experimentellen Messungen verglichen wird um verschiedene Modelle zu testen. Weiter wird die thermische Mischung im TCS überprüft und mögliche Verbesserungen werden aufgezeigt.

List of Figures

| | | |
|------|--|----|
| 1.1 | Overview on Temperature Control System | 1 |
| 1.2 | A detailed view on the temperature sensor. | 2 |
| 2.3 | Three different scopes for approaching numerical fluid simulation. | 4 |
| 2.4 | Maxwell-Boltzmann distribution function for O_2 | 6 |
| 2.5 | $D2Q9$ and $D3Q19$ as example arrangements for lattices. | 9 |
| 3.6 | Geometry of the T-junction pipe. | 12 |
| 3.7 | Definition of refinement transition length. | 13 |
| 3.8 | Literature results for average velocity in symmetry plane of T-junction | 14 |
| 3.9 | XFLOW Case 1 results for average velocity in symmetry plane of T-junction | 15 |
| 3.10 | XFLOW Case 2 results for average velocity in symmetry plane of T-junction | 15 |
| 3.11 | XFLOW Case 3 results for average velocity in symmetry plane of T-junction | 16 |
| 3.12 | Literature results for the average temperature in symmetry plane of T-junction | 17 |
| 3.13 | Average temperature in symmetry plane of T-junction for XFLOW Case 1 | 17 |
| 3.14 | Average temperature in symmetry plane of T-junction for XFLOW Case 2 | 18 |
| 3.15 | Average temperature in symmetry plane of T-junction for XFLOW Case 3 | 18 |
| 3.16 | Streamwise velocity profiles at $z = 2.6D$ compared to experimental results | 19 |
| 3.17 | Streamwise velocity profiles at $z = 6.6D$ compared to experimental results | 20 |
| 3.18 | Streamwise velocity velocity fluctuations at $z = 6.6D$ compared to experimental results | 21 |
| 3.19 | Bottom wall temperature of XFLOW compared to ANSYS CFX/FLUENT and experimental data | 22 |
| 3.20 | Left wall temperature of XFLOW compared to ANSYS CFX/FLUENT and experimental data | 22 |
| 3.21 | Top wall temperature of XFLOW compared to ANSYS CFX/FLUENT and experimental data | 23 |
| 3.22 | Location of refinement region for refined cases | 24 |
| 3.23 | Time averaged, streamwise velocity profiles at $z = 2.6D$ for the refined cases. | 25 |
| 3.24 | Time average streamwise velocity profiles at $z = 6.6D$ for the refined cases. | 25 |
| 3.25 | Bottom wall temperature plotted for the refined cases. | 26 |
| 3.26 | Left wall temperature plotted for the refined cases. | 27 |
| 3.27 | Top wall temperature plotted for the refined cases. | 27 |

| | | |
|------|--|----|
| 3.28 | Overview of geometry with boundary conditions for trim tapping investigation. | 29 |
| 3.29 | Total pressure field for sharp trim tapping. | 30 |
| 3.30 | Total pressure field for 5 mm rounded trim tapping. | 30 |
| 3.31 | Temperature field of sharp trim tapping for a trim flow of 20 g/s | 32 |
| 3.32 | Temperature field of rounded trim tapping for a trim flow of 20 g/s | 32 |
| 4.33 | Pressure fluctuations appeared in most simulations. | 36 |
| 4.34 | Pressure fluctuations at the probe located at the temperature sensor. | 36 |
| 4.35 | Problems with temperature boundary conditions. | 37 |
| 4.36 | Instantaneous total pressure field of TZ 1. | 39 |
| 4.37 | Average total pressure field of TZ 1. | 39 |
| 4.38 | Average static pressure field of TZ 1. | 40 |
| 4.39 | Average temperature field of TZ 1. | 40 |
| 4.40 | Average temperature profile for the low trim flow in TZ1. | 41 |
| 4.41 | Wall temperature for TZ 2. | 42 |
| 4.42 | Temperature profile at the sensor cross section. | 43 |
| 4.43 | Overview of TZ3 with detailed plotting line of outlet 2. | 43 |
| 4.44 | Average outlet temperatures for TZ4 at a trim flow of 40 g/s. | 44 |
| 4.45 | The hot stream directly enters the first branch for rising ducts 1 and 2. | 45 |
| 4.46 | Cross sectional temperature profile for the high trim flow of TZ 3. | 45 |
| 4.47 | The wall temperature indicates uniform, mixed temperatures downstream the outlets 1 & 2. | 46 |
| 4.48 | Big deviations of the outlet temperature profiles of outlets 1 and 6 can be monitored for low trim flow of TZ 3. | 47 |
| 4.49 | Temperature profile at outlets 1 & 2 for low trim flow at TZ 3 | 48 |
| 4.50 | The trim flow remains attached to the bottom wall of the main pipe for low trim inlet velocities. | 49 |
| 4.51 | Average wall temperature of TZ 4 at high trim flow. | 50 |
| 4.52 | Average temperature of all outlets over the diameter. | 51 |
| 4.53 | A longitudinal cross section of the average temperature profile in the sensor plane. | 51 |
| 4.54 | Average temperature of all outlets over the diameter for a low trim flow. | 52 |
| 4.55 | A hot stream of air surrounds the sensor of TZ 5 and leads to high sensor indicated temperatures. | 53 |
| 4.56 | There is a hot stream which reaches until the outlet and leads to strongly non-uniform outlet temperature. | 53 |
| 4.57 | Average wall temperature and temperature at the sensor cross section for TZ 5. | 54 |
| 4.58 | Wall temperature for TZ 6 and high trim flow. | 55 |
| 4.59 | The temperature of the probe which is located at the sensor is strongly fluctuating over the time of 2 s. | 56 |
| 4.60 | Outlet temperature for TZ 6 and high trim flow | 56 |
| 4.61 | Wall temperature for the low trim flow of TZ 6. | 57 |

| | | |
|------|---|----|
| 4.62 | Temperature cross section at the sensor of TZ 7 | 58 |
| 4.63 | Wall temperature for the high trim flow of TZ 7 | 58 |
| 4.64 | Wall temperature for the low trim flow of TZ 7 | 59 |
| 4.65 | Temperature profile at the cross section of the temperature sensor | 60 |
| 4.66 | Temperature profile at the longitudinal cross section of the FCRC | 60 |
| 4.67 | The low trim flow results in a different temperature profile at the cross section of the temperature sensor as the hot flow remains attached to the wall. | 61 |
| 4.68 | There is at least 5 K difference between the top and bottom wall temperature in the sensor cross section. | 61 |
| 4.69 | Average wall temperature for high trim flow in CCRC. | 62 |
| 4.70 | Average temperature at the sensor cross section. | 62 |
| 4.71 | The low trim flow hits the sensor of the CCRC. | 63 |
| 4.72 | The hot stream is close to the sensor of the F/D. | 64 |
| 4.73 | Average wall temperature for the F/D and 10 g/s. | 65 |
| 4.74 | Dimensions of the simulated mixing device. | 67 |
| 4.75 | Working principle of the oxyinator. | 68 |
| 4.76 | Additional mixing device within TZ 3. | 68 |
| 4.77 | Average outlet temperature profiles for TZ 3 with 4 bladed mixer. | 69 |
| 4.78 | A non-physical temperature drop appears downstream the 4-bladed mixer. | 69 |
| 4.79 | Average outlet temperature profiles for TZ 3 with 6 bladed mixer. | 70 |
| 4.80 | Average temperature at the cross section of the first riser ducts for TZ3 with the automatic wall function and without pressure fluctuations. | 71 |
| 4.81 | Average temperature profiles for the riser ducts of TZ 3 without pressure fluctuations. | 72 |
| 4.82 | Temperature profiles at the riser ducts of TZ 4 for the automatic (equilibrium wall-function) wall model. | 73 |
| 4.83 | Average temperature at the longitudinal sensor cross section for the automatic wall model. | 73 |
| 4.84 | Average temperature at the longitudinal sensor cross section for the original case with a coarse resolution of 0.01 m. | 74 |
| 4.85 | Average temperature at the longitudinal sensor cross section for the fine resolution with automatic wall model. | 75 |

List of Abbreviations

- CCRC... Cabin Crew Rest Compartment
CFD ... Computational Fluid Dynamics
DNS ... Direct Numerical Simulation
F/D ... Flight Deck
FCRC ... Flight Crew Rest Compartment
GUI ... Graphical User Interface
LBM ... Lattice Boltzmann Method
LES ... Large Eddy Simulation
LGA ... Lattice Gas Automata
MPS ... Multi Purpose
MU ... Mixing Unit
RANS ... Reynolds Averaged Navier Stokes
RMS ... Route Mean Square
RTL ... Refinement Transition Length
TCS ... Temperature Control System
TZ ... Temperature Zone
WALE... Wall Adapting Local Eddy

1 Introduction

The Temperature Control System (TCS) of an aircraft like the Airbus A350-900 ensures safety and well-being of passengers and crew members. The system has to ensure comfortable temperatures and humidity during all phases of flight. A wide range of temperatures, ranging from -50°C at cruising altitude to $+50^{\circ}\text{C}$ on the apron complicates the task of maintaining a constant cabin temperature. A person at rest delivers heating power of roundabout 120 W. As the A350-900 has a capacity of more than 300 passengers this sums up to an impressive heating power of 36 kW that needs to be abolished in addition. But not only the environmental extremes make it difficult for engineers to fulfil their task. Also the demands for lightweight design, little space, efficiency and simplicity of the system forces engineers to put high effort on climate systems in aircraft. As the TCS is one predominant noise-source inside the cabin, engineers are also drawn to minimize the noise emission.

The TCS of the A350-900 (depicted in Figure 1.1) consists of 7 independently controlled Temperature Zones (TZ) for passengers plus extra zones for Flight Deck (F/D), Flight Crew Rest Compartment (FCRC), Cabin Crew Rest Compartment (CCRC) and Multi Purpose (MPS). All these zones are fed with recirculated air from the cabin and fresh air, tempered in the climate system. These flows are mixed in the Mixing Unit (MU) which consists of the pre-mixer and the main-MU. For the purpose of this investigation only the ducts of the different zones and the main-MU are considered. Figure 1.1 shows an overview of the TCS-system with the different TZs.

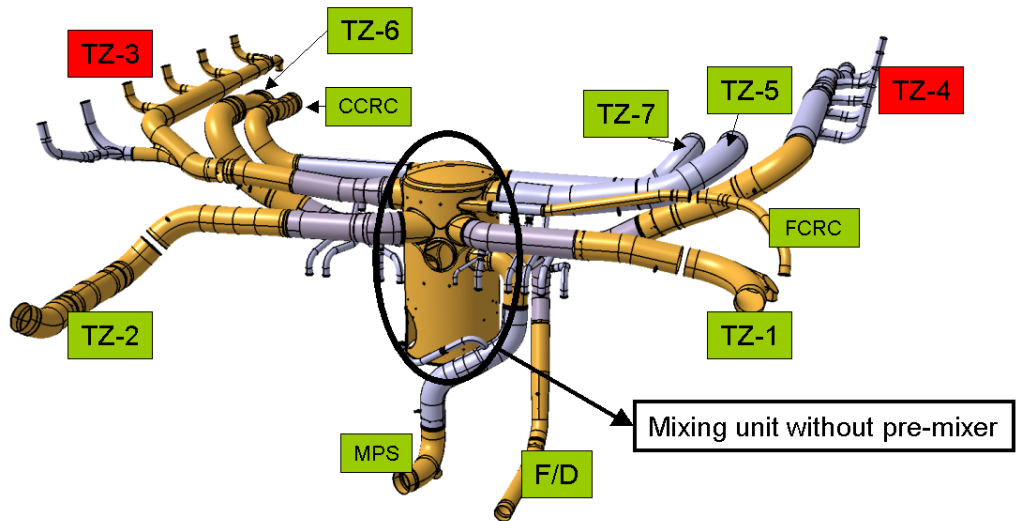


Figure 1.1: Overview of the TCS with the different ducts leading to different TZs.
TZ 3 and 4 are considered critical because the rising ducts that lead to the outlet are very close to the trim intersection and the air has to be at constant, average mixing temperature before leaving the ducts.

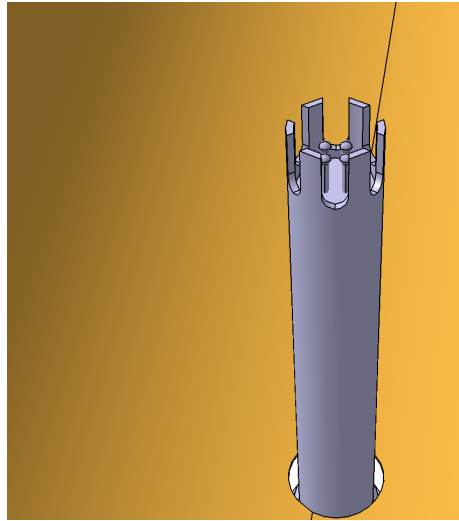


Figure 1.2: A detailed view on the temperature sensor.

Downstream the MU the air temperature is regulated via trim injections which inject hot bleed air, extracted from the engine after the compressor stage. The bleed air is injected with temperatures of about 180 °C and a regulated mass flow, usually between 0 and 40 g/s. In order to be able to regulate the temperature, temperature sensors as depicted in Figure 1.2, are installed downstream the trim intersection. On the one hand, it is important that these sensors are located such that they can measure the average mixing temperature. Therefore they have to be located far downstream the intersection. On

the other hand, space in aircraft usually is little and these sensors have to be accessible for assembly and maintenance. A trade-off between these two aspects has to be made in order to find suitable sensor positions.

The purpose of this investigation is to check the quality of thermal mixing at the location of the temperature sensors for the TCS of the A350-900 (New-Crown) and to validate these sensor-positions. In case the temperature sensor is located in an area of non-mixed cold or hot air, the measured temperature will not correspond to the average mixing temperature and the controller would inject too little or too much trim air. Areas of cold/hot air or oscillation of cabin temperature may be results of improper temperature measurement. If necessary, additional mixing devices are to be investigated and implemented in order to ensure sufficient thermal mixing.

The investigation is conducted with XFLOW, a quite novel software for Computational Fluid Dynamics (CFD) simulation. This investigation will also be a benchmark for XFLOW, its applicability and handiness in engineering problems. An introduction to the fundamental principles of the Lattice Boltzmann Method, used in XFLOW, will be presented within the next section.

The present thesis contains a Methods section where theoretical background of applied tools and methods is presented, followed by a standard test case which should bring clarity on choosing the appropriate simulation setup. The outcome of the investigation of the TCS is depicted in the Results section. Finally, the reader will find a Summary and Outlook section with ideas for future research.

2 Methods

This Methods section will give the reader an overview on applied tools and methods. The most important feature for this investigation of fluid flow is XFLOW, a Computational Fluid Dynamics (CFD) software which works on particle based Lattice Boltzmann Method (LBM). This software and the underlying principles will be discussed within the following section.

2.1 Introduction to XFLOW

The physics of fluids can be considered at different scopes, each one acting on a different length scale. In a top-down approach one could start describing fluids on a macroscopic scope with a finite volume that usually contains a huge number of basic modules, the molecules and atoms the fluid is made of. For this approach, which is also called the continuum approach, only average properties within the finite volume are of interest but not the properties of single atoms, as they do not even exist for these kind of simulations.

Such average properties are known as velocity, pressure and temperature. While reading this paper, the reader gets hit by particles travelling at speeds of several hundreds of metres per second although the ambient fluid is at rest. Despite the extreme speeds of single particles one cannot get notice of these impacts as the momentum is really small. In other words, the behaviour of single, microscopic particles is not of interest for the macroscopic world. Macroscopic properties like velocity, pressure and temperature, as they are known in general, are only slightly dictated by such rapidly moving particles because of averaging over a huge number of particles (usually in the order of the Avogadro number $N_A = 6.022 \cdot 10^{23} \text{ mol}^{-1}$). Remember the definition of pressure which is nothing else than the average force acting per area.

For the computation the fluid domain is discretized with a computational mesh whereas each mesh-volume element corresponds to one of the previously mentioned finite volumes. The average values of the macroscopic fluid properties (velocity, pressure and temperature) can then be saved for example on the mesh nodes. The ruling equations are known as the Navier-Stokes equations which represent mass-, momentum- and energy-conservation. These equations are second-order partial differential equations and usually difficult to solve. Finite volume, finite elements or finite differencing methods are used to derive algebraic equations from the differential equations which can be solved iteratively on the computational grid.

The smallest unity, which is of importance for fluid dynamics, is the molecule, made of more or less atoms depending on the complexity of the molecule. These molecules can be considered as perfectly elastic spheres. Modelling and simulating each molecule individually is the approach from the other side of the scope, the microscopic scope. The Avogadro number which was already mentioned above tells that there is a huge number of particles that has to be handled during simulation

(remember the Avogadro number which corresponds to the number of molecules per mol). Additionally, the temporal resolution has to be extremely high due to very small timesteps between collisions of molecules. These two facts make this approach which is also known as Direct Numerical Simulation (DNS) non-applicable nowadays and in the foreseeable future for problems of technical relevance as the computational effort is immense, even for simplest problems.

In between these two scopes there is a mesoscopic approach where imaginary particles describe the distribution probability of the molecules. Each of those imaginary particles can be described as a collection of many molecules, such that the total number of elements reduces drastically. The fundamental equation is the Boltzmann equation and that is why these methods are called Lattice Boltzmann Methods (LBM). The LBM also relies on conservation principles but on a microscopic level, whereas the continuum approach applies them on a macroscopic level. There is a computational grid/lattice similar to the continuum approach but for the LBM the lattice must fulfil certain criteria of symmetry which will be described later on. Before going more into detail for the LBM of XFLOW Figure 2.3 summarizes the mentioned scopes and schematically depicts the ideas of discretization for each approach.

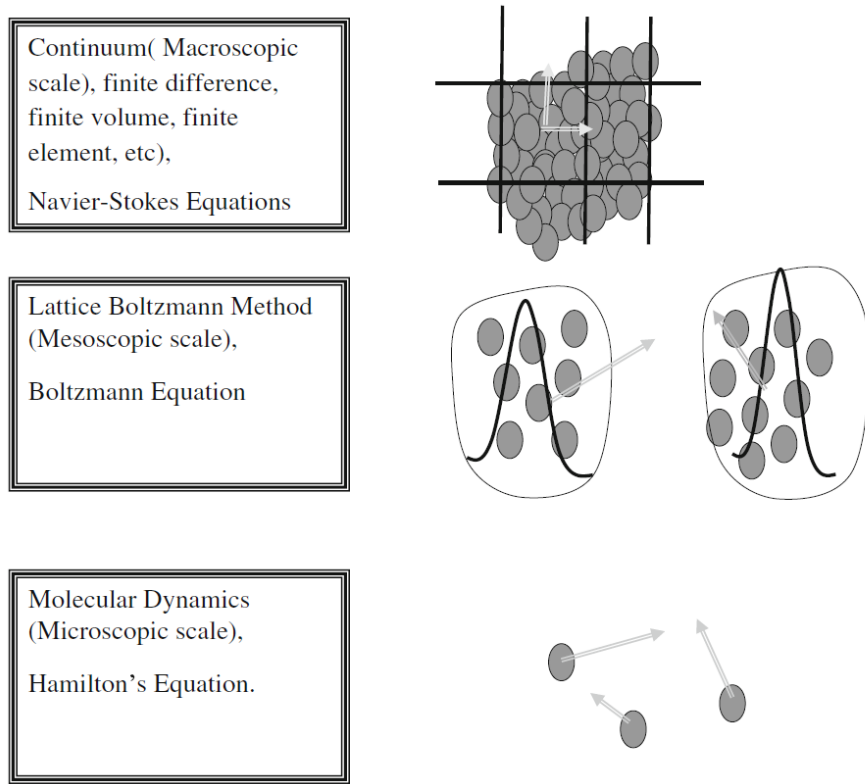


Figure 2.3: Three different scopes for approaching numerical fluid simulation. XFLOW works on a mesoscopic scale which combines advantages of both other approaches. (Mohamad, 2011, p.3)

XFLOW is a commercial CFD software, developed by Next Limit Technologies, a company located in Madrid (Spain), also offering software for graphical illustration and rendering. XFLOW can be used for simulation of *internal* and *external* fluid flow. *Internal flow* can be defined as a flow which is enclosed by geometry (e.g. flow in a duct) whereas *external flow* means that the fluid domain encloses the geometry (e.g. flow around airfoil). In case of the TCS only *internal flow* is of interest, as the whole fluid domain is ducted. The *internal flow* can be distinguished further into *single phase internal* and *free surface internal*: in the example of a ducted flow, *single phase internal* is appropriate if the duct is completely filled with one single fluid, whereas the *free surface internal* model is used in case the duct is only partly filled with fluid 1 (e.g. water) and has a free contact surface adjacent to fluid 2 (e.g. air). XFLOW seems to perform well also for external flow as the XFLOW results for the second AIAA high lift prediction workshop show. For the purpose of this investigation only *single phase internal* flow is of interest.

The basic principles of XFLOW's LBM approach were already introduced within the beginning of this section. The LBM is an advancement of the Lattice Gas Automata (LGA) which was introduced by Frisch, Hasslacher and Pomeau in 1986. The LBM solves the Boltzmann equation on a computational lattice. The Boltzmann equation is a stochastic equation, as the fundamental function is the velocity probability distribution function. This distribution function will be derived in the following subsection before the Boltzmann equation itself is introduced in the subsequent subsection.

2.1.1 The Maxwell-Boltzmann Distribution Function

The previous section has shown that properties of individual molecules are unimportant in a macroscopic scale as the macroscopic quantities themselves are averaged values of many molecules. According to Mohamad, Maxwell was the first who came up with the idea of averaging because he thought that:

“[...]the knowledge of velocity and position of each molecule at every instant of time is not important. The distribution function is the important parameter to characterize the effect of the molecules; what percentage of the molecules in a certain location of a container have velocities within a certain range, at a given instant of time.” (2011, p.7).

The particles obey the conservation principles of mass, momentum and energy according to the rules of particle dynamics (Newton's second law). By transferring momentum and energy from fast particles to slowly moving particles energy is conserved. In order to be able to model representative particles as an averaged number of many molecules a velocity distribution function has to be known. This distribution function tells nothing else than the probability of finding molecules travelling within a certain range of speeds.

Mohamad derives the Maxwell-Boltzmann distribution function (2.1) where the resulting distribution function as a function of velocity appears to (2011, pp.7-9):

$$f(c) = 4\pi \left(\frac{m}{2\pi kT} \right)^{\frac{2}{3}} c^2 e^{-\frac{mc^2}{2kT}} \quad (2.1)$$

In equation (2.1) m represents the molecular mass, c corresponds to the velocity, k is the Boltzmann constant and T is the temperature of the fluid. Integration of (2.1) over all velocities yields unity.

The average velocity can be obtained by integrating the Maxwell-Boltzmann distribution function to:

$$\langle c \rangle = \int_0^\infty c f(c) dc \quad (2.2)$$

Figure 2.4 shows a sample distribution function for O_2 and two different temperatures:

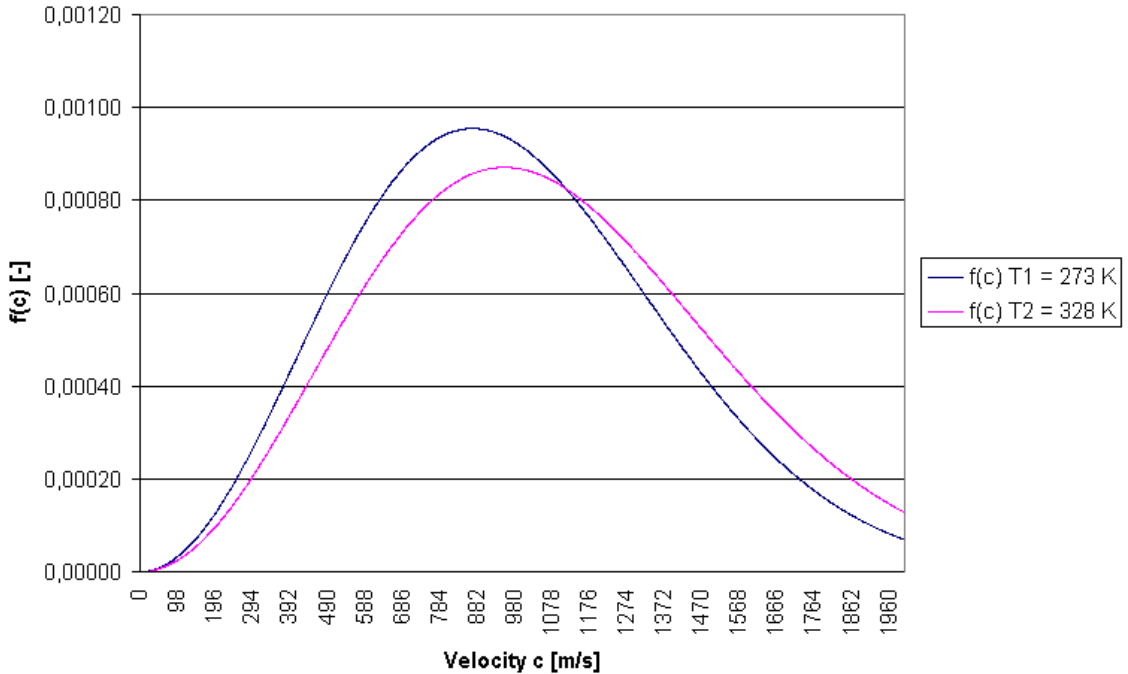


Figure 2.4: Depicted is the Maxwell-Boltzmann distribution function for O_2 and two different temperatures. Note the maximum of the function moves to higher velocities as the temperature increases.

2.1.2 The Boltzmann Equation

Using the previously introduced Maxwell-Boltzmann distribution function one can describe a fluid domain by defining $f(x, c, t)$. Hence the Distribution function is extended for two more independent variables, as there is the time t and the location

in space x . The velocity distribution function is now describing how many molecules one can find between x and $x + dx$ at discrete time t with velocities between c and $c + dc$. Note that the probability of finding a molecule with a discrete velocity c is zero as particles continuously change velocities. Only integration of the probability function $f(x, c, t)$ over a range of velocities and multiplication with the total number of molecules N yields the probable number of particles within the range of speeds.

The resulting Boltzmann equation, which is named after the Austrian physicist Ludwig Eduard Boltzmann (1844-1906) is derived according to Mohamad (2011, pp.15-17).

Consider a number of particles $f(x, c, t)$ at time t and after a small timestep at time $t + dt$. If an external force F acts on the particles for a time dt the velocity of the molecules will change to $c + Fdt$ and the position will change to $x + cdt$.

Drawing a balance on the change of particles before and after applying the force F yields that the overall number of particles remains constant which can be formulated to:

$$f(x + cdt, c + Fdt, t + dt)dxdc - f(x, c, t)dxdc = 0 \quad (2.3)$$

Equation (2.3) is only valid if no collisions between particles took place. If collisions took place, the number of particles changes. In order to account this net-change in particles in the interval $dxdc$ the collision operator Ω is introduced. Hence, equation (2.3) becomes:

$$f(x + cdt, c + Fdt, t + dt)dxdc - f(x, c, t)dxdc = \Omega(f)dxdcdt \quad (2.4)$$

Division by $dxdcdt$ yields:

$$\frac{df}{dt} = \Omega(f) \quad (2.5)$$

The distribution function f is dependent on space x , velocity c and time t . Therefore the total differential of $f(x, c, t)$ can be calculated to:

$$df = \frac{\partial f}{\partial x}dx + \frac{\partial f}{\partial c}dc + \frac{\partial f}{\partial t}dt \quad (2.6)$$

In order to obtain the expression on the left-hand side of (2.5), equation (2.6) is divided by dt :

$$\frac{df}{dt} = \frac{\partial f}{\partial x}\frac{dx}{dt} + \frac{\partial f}{\partial c}\frac{dc}{dt} + \frac{\partial f}{\partial t} \quad (2.7)$$

One can easily see that by introducing the acceleration a , the last expression can be rewritten to:

$$\frac{df}{dt} = \frac{\partial f}{\partial x} \cdot c + \frac{\partial f}{\partial c} \cdot a + \frac{\partial f}{\partial t} \quad (2.8)$$

Finally, after applying Newton's second law to $a = F/m$, the Boltzmann equation (2.5) can be expressed as:

$$\frac{\partial f}{\partial t} + \frac{\partial f}{\partial x} \cdot c + \frac{F}{m} \cdot \frac{\partial f}{\partial c} = \Omega \quad (2.9)$$

The last notation of the Boltzmann equation (rewritten for $F = 0$ in different notation in equation (2.10)) is the equation that needs to be solved for CFD simulation. The fact that Ω is a function of f makes the Boltzmann equation difficult to solve.

$$\frac{\partial f}{\partial t} + c \cdot \nabla f = \Omega \quad (2.10)$$

Because of the collision term the Boltzmann equation is difficult to solve and there is a necessity for simplification. In 1954 Bhatnagar, Gross and Krook introduced the BGK approximation for the collision operator Ω (1954). The goal is to abolish mathematical barriers without foiling physical correctness. BGK redefined the collision operator to:

$$\Omega_{BGK} = \frac{1}{\tau} (f^{eq} - f) \quad (2.11)$$

(Succi, 2001, p.15)

As equation 2.11 shows, an equilibrium distribution function f^{eq} and the so-called relaxation parameter τ which relates to the viscosity of fluids are introduced. Usually, the relaxation parameter has a complex dependency on the distribution function f but assuming a constant value for τ is what makes the BGK approach simple and successful. The Boltzmann equation, in combination with the BGK-collision operator forms the basic equation for CFD simulation as it is what the Navier-Stokes equations are to continuum CFD approaches. In fact, the Navier-stokes equations can be derived from the Boltzmann equation.

At this point the fundamental ideas and the underlying Boltzmann equation for the LBM have been introduced. Another important topic for the LBM is discretization. The Boltzmann equation needs to be solved on a lattice which represents the fluid domain. Depending on the dimensions there are different types of lattices possible. Some of them are presented in the following section.

2.1.3 The Lattice for the Lattice Boltzmann Method

Different from continuum approaches, the computational lattice for the LBM needs to fulfil criteria of symmetry. In general, the lattice is a collection of points inside the fluid domain where particles, represented by distribution functions, are located. These points are interconnected via routes at which particles - respectively their distribution functions - move. There is a certain notation, used from now on, which has the form of: $DnQm$. In this notation n stands for the number of dimensions in

space and m represents the number of connections to neighbouring points, the so called speed model.

Starting from smallest 1-dimensional $D1Q2$ over 2-dimensional $D2Q9$ which is depicted in Figure 2.5 and 3-dimensional $D3Q19$ also depicted in Figure 2.5 many different types of lattices are possible.

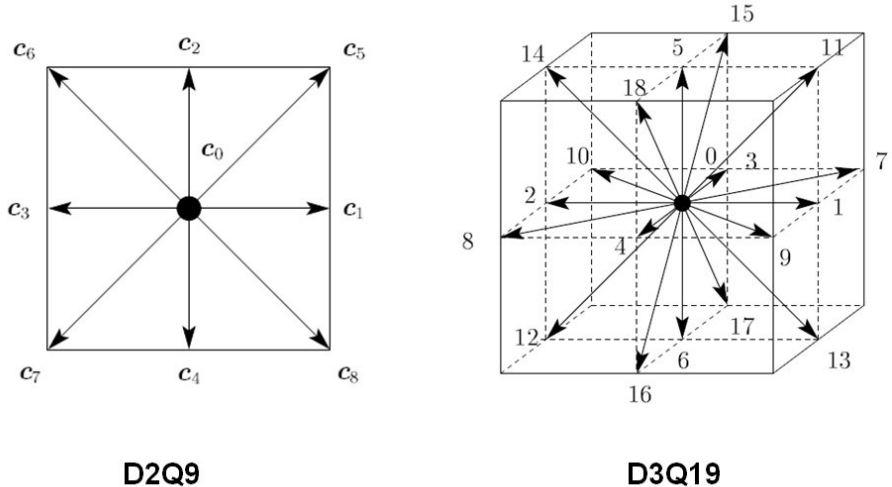


Figure 2.5: $D2Q9$ and $D3Q19$ as example arrangements for lattices in 2- and 3-dimensional space (image from Scholarpedia).

An element of type $D2Q9$ can hold for example 9 particles (represented by distribution functions $f_{0\dots 8}$) travelling at speeds of $c_{0\dots 8}$. The particle velocities is one point where the LBM distinguishes from it's predecessor, the Lattice Gas Automata (LGA). For the LGA in detail the possible velocities for a $D2Q9$ lattice are: $c_0 = (0, 0)$, $c_1 = (1, 0)$, $c_2 = (0, 1)$, $c_3 = (-1, 0)$, $c_4 = (0, -1)$, $c_5 = (1, 1)$ and the like. In other words, the components of the velocity vector for the LGA only takes integer values whereas the LBM allows values different from “0” and “1”. This leads to improvements in statistical noise which is known to be a problem for the LGA (Hussein, 2010, p.18).

For a $D2Q9$ lattice the weighting factors for the distribution functions $f_{0\dots 8}$ are: $4/9, 1/9, 1/9, 1/9, 1/9, 1/36, 1/36, 1/36$ and $1/36$. The same concept can be applied basically also for the $D3Q19$ lattice which allows more degrees of freedom.

Within one timestep particles can move to the neighbouring lattice points according to their velocity vector c_i . It is only allowed for one single particle to move along one connection between two points. Indeed this may seem to be a rather sharp restriction for the movement of particles compared to real fluids but amazingly this simple model is enough to represent realistic fluid behaviour.

Only the basic ideas of the LBM were introduced within this section. There is a lot of theory to study in order to go into the depths of this method but for

basic understanding this information should be enough. The next subsection will introduce the reader into the fundamental commands for XFLOW in bash mode.

2.2 XFLOW and The Command Line

There are several different ways of starting XFLOW simulations. The easiest one is to use the Graphical User Interface (GUI). In the GUI one can find buttons for starting and resuming computations. If the simulation setup was done properly before, the computation starts and the progress can be monitored in the message box.

A second opportunity is to use the GUI for setting up distributed computation. Therefore XFLOW has to be running in LABS mode. The author did not have a version which supported the LABS mode. Therefore it was necessary to run all commands from the command line in the bash mode. No big deal, if the commands are known.

Also in the bash mode it is necessary to do the whole simulation setup via the GUI. It is important to set the right path to the project folder. After setup, the steps to launch the computation can be executed manually in the command line.

The first step is to generate the domain. Assuming, the XFLOW installation path is added to the Linux search path, the command is as follows:

```
$ xflow <project.xfp> -genbinaries
```

If distributed computation is desired, the domain can be split into n partitions with the following command:

```
$ generateDomain3d <project.xfd> -mpi=n
```

As a result, the file *project.xfd.part.n* should show up in the project folder now. Finally, the computation can be launched; for local computation the command looks like:

```
$ engine-3d* <project.xfb>
```

where * needs to be replaced for example by “-t” if thermal analysis is switched on in the project. For other replacements of * refer to the XFLOW user manual.

If a distributed computation is to be launched, the command looks like the following, in case of Open-MPI:

```
$ mpirun -wd /directory/to/project/ -hostfile <list_of_machines> -np <n> engine-3d-*mpi-ompi <project.xfb> -maxcpu=<CPU's/thread>
```

The file *list_of_machines* needs to be stored inside the project folder and has to contain the following data in the following format:

```

list_of_machines:
<node_1> slots=<k>
<node_2> slots=<l>
<node_3> slots=<m>

```

Finally, it is also useful if one can launch the computation without necessarily staying connected to the machine all the time. Therefore each command can be run in the following format:

```
$ bash -c "nohup <command> <options> > out.file 2>&1 &"
```

3 CFD Investigation

3.1 Test Case - Thermal Mixing in a T-Junction Pipe

Before investigating the complex geometry of the TCS, a simplified geometry is investigated as a test case. The goal of this investigation is to find the most suitable model for thermal mixing based on results from literature which will then be applied on investigation of the TCS. For validation of XFLOW's thermal model, the mixing process of cold and hot water in a circular T-junction pipe is investigated. The considered problem is well described in literature: Klören and Laurien (2013) investigated this problem in terms of thermal fatigue of high performance cooling cycles whereas Hirota et al. (2008) investigated T-junctions with rectangular cross sections. The paper of Frank et al. (2009), which will be drawn for consideration here, deals with circular cross sections only.

With Reynolds numbers above 10^5 for both inlets the pipe-flow is expected to be turbulent as the critical Reynolds number for pipe flows is approximately $Re_{crit} = 2000$. For detailed physical setup and boundary conditions see subsection “Geometry and Setup” below.

To model the turbulence, the default and recommended turbulence model in XFLOW, the so called Wall-Adapting Local Eddy (WALE) model, which is an implementation of Large Eddy Simulation (LES) will be used. As wall functions 2 different approaches are examined: first, the Enhanced Wall-function, and second, the Non-equilibrium Enhanced Wall-function. The “Segregated Energy” model, which solves the energy equation (3.12) to model thermal effects, solves the energy equation decoupled from the flow equations. The energy equation reads:

$$\rho C_p \frac{\partial \theta}{\partial t} = \nabla \cdot (k \nabla \theta) + \varphi \quad (3.12)$$

Where ρ is the density, C_p is the specific heat capacity, θ is the temperature, k is the thermal conductivity and φ is the viscous heat dissipation which can be switched on and off in the advanced settings. XFLOW's approach of using the LBM allows easy implementation of thermodynamics whereas for conventional Navier-Stokes solvers this is a difficult task.

The following section will describe the geometrical setup of the investigation according to the investigations from Frank et al. (2009).

3.1.1 Geometry and Setup

The dimensions of the T-junction are chosen according to Frank et al. (2009, p. 10) where the experiment, conducted at Vattenfall Research and Development in 2006, is described in detail. Figure 3.6 shows the geometrical dimensions in CATIA:

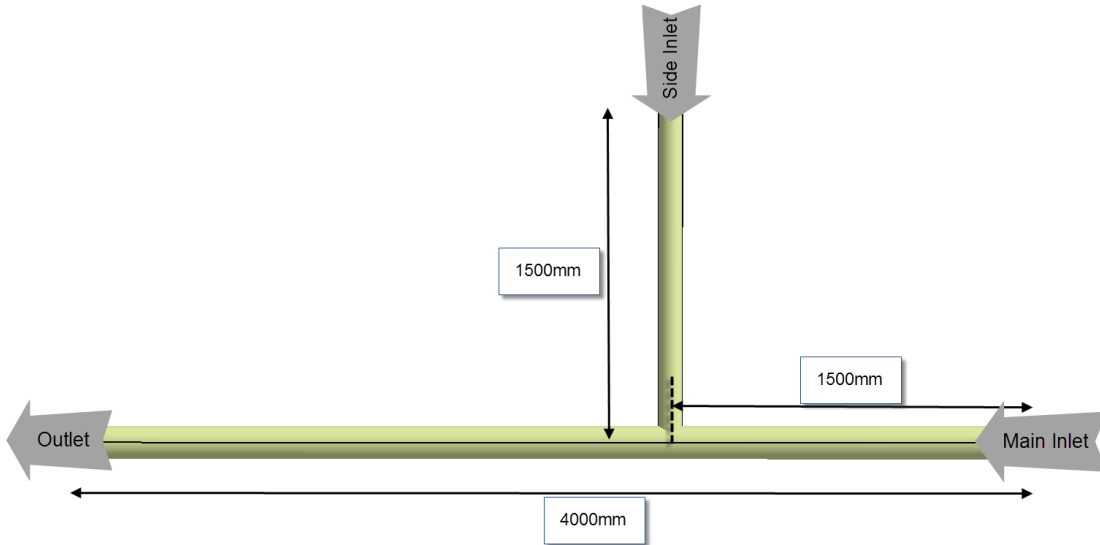


Figure 3.6: The geometrical dimensions of the investigated T-junction pipe. There is one Main Inlet and one Side Inlet where the hot fluid is injected.

Three simulations with different resolutions and different models are executed. Hence these three cases will be named “Case 1, Case 2 and Case 3”. Table 1 shows the difference between those cases:

Table 1: XFLOW’s simulation setup for the considered cases.

| | Case 1 | Case 2 | Case 3 |
|-----------------------|---------------------|-------------------------------------|---------------------|
| XFLOW Version | v5 | v5 | v19 |
| Turbulence Model | WALE | WALE | WALE |
| Wall-model | Enhanced Wall-model | Non-equilibrium Enhanced Wall-model | Enhanced Wall-model |
| Resolution [m] | 0.03 | 0.01 | 0.01 |
| Wake resolution [m] | 0.01 | 0.005 | 0.005 |
| Wall refinement [m] | 0.005 | 0.005 | 0.005 |
| Transition length [-] | 2 | 2 | 2 |

Next Limit defines the Transition length as follows: “The refinement transition length (rtl) refers to the number of element layers between two refinement levels, i.e. it represents the gradient in the transition from fine resolution at the walls to coarse resolution in the far field. Small rtl values lead to quickly growing element sizes while large rtl values lead to smooth transition.” (XFLOW User Guide, 2013, p. 102). Further, Figure 3.7 illustrates refinement transition for $rtl = 2$ and $rtl = 4$, respectively:

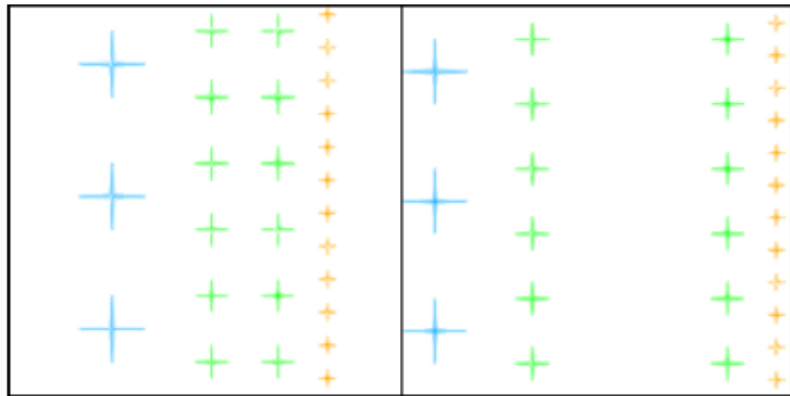


Figure 3.7: Refinement from coarse (blue) to fine (yellow) for $rtl = 2$ (left) and $rtl = 4$ (right) (XFLOW User Guide, 2013, p.102).

From Case 1 to Case 2 the resolution is increased and the wall model is changed from Enhanced Wall-function to Non-equilibrium Enhanced Wall-function. The only difference between Case 2 and Case 3 is that the wall model is changed back to Enhanced Wall-function again whereas the resolution remains the same.

The physical setup consists of two water inlets (see Figure 3.6) and one outlet. At the main-pipe-inlet cool water enters with 15°C at a constant flow rate of $Q_1 = 12l/s$ and at the second inlet hot water enters with 30°C at $Q_2 = 24l/s$ which corresponds to an inlet velocity of about $v = 1.53m/s$ for both inlets which further results in Reynolds numbers $Re > 10^5$ for both ducts and therefore turbulent flow conditions.

At both inlets a mass flow boundary condition with the given temperatures is set. The outlet is modelled with gauge pressure outlet with 0 Pa relative pressure. The wall is modelled according to Table 1 and adiabatic thermal boundary condition is applied. XFLOW’s environment setup is set to 3d “Single phase internal” model with “Segregated energy” model for thermal analysis without radiation. For turbulence modelling the “WALE” model with default settings is set. Further, high order boundary conditions are enabled. Next Limit states that the high order boundary condition is more accurate but less stable, as it uses second order boundary conditions. The whole fluid field is initialized with 15°C .

In the materials section one has to enter the properties of water manually because “Single phase internal” sets air as default fluid. The properties read: molecular

weight: $MW = 18.1u$, density: $\rho = 998kg/m^3$, dynamic viscosity: $\mu = 0.001Pas$, thermal conductivity: $\lambda = 0.58W/mK$ and specific heat capacity: $C_p = 4182J/kgK$.

Frank et al. (2009, p. 17) extract the results after $7.6s$ simulation time, in this case 10 seconds will be simulated. The resolved scale is set according to Table 1. For final data analysis averaged fields are to be saved, where the averaging process begins after $1.5s$ simulation time.

As a next step the results of this investigation will be presented and discussed to find the appropriate setup for simulation of the TCS.

3.1.2 Results of T-Junction Investigation

Velocity fields

As a first result the time averaged velocity is plotted in the symmetry plane of the pipe. The results of Cases 1-3 (Figures 3.9-3.11) can be compared to the results from the literature (Figure 3.8).

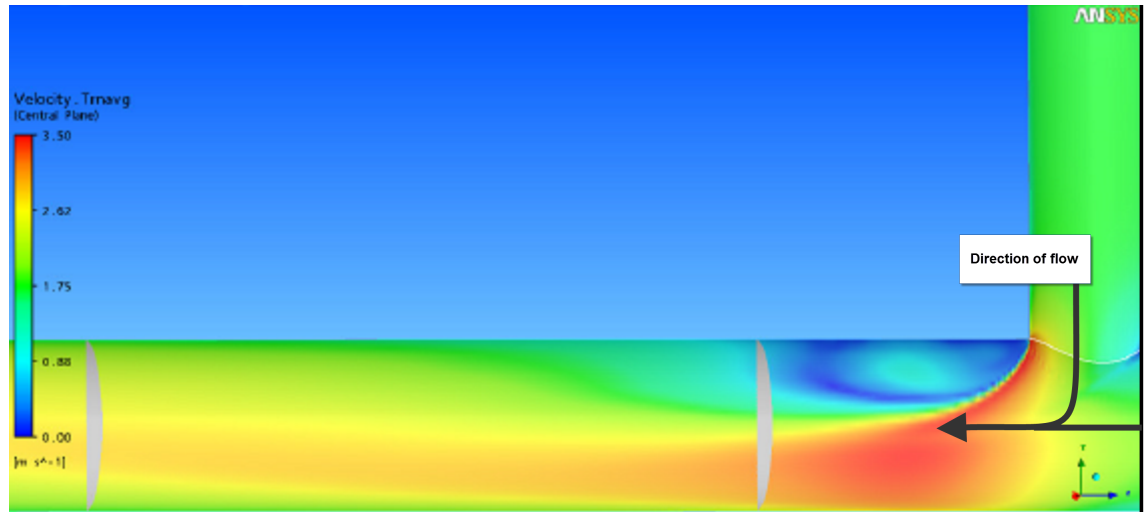


Figure 3.8: Average velocity in symmetry plane. Result from ANSYS with 2.256.320 mesh nodes (Frank et al., 2009, p.15).

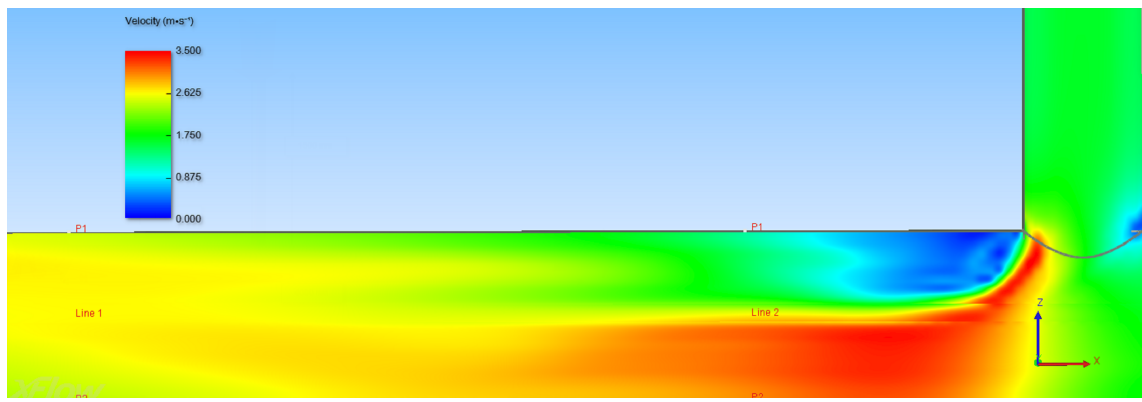


Figure 3.9: Average velocity in symmetry plane. XFLOW result of Case 1 (number of elements ≈ 170.000).

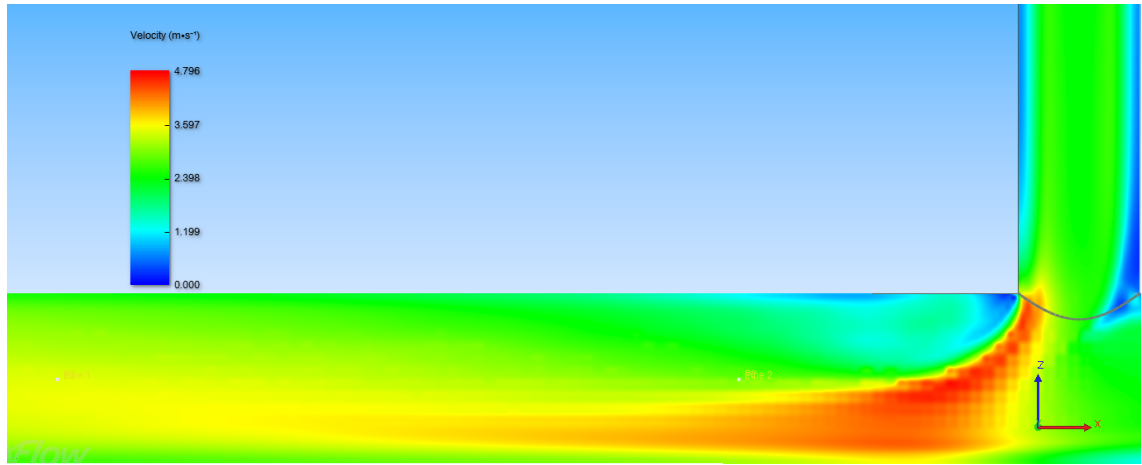


Figure 3.10: Average velocity in symmetry plane. XFLOW result of Case 2 (number of elements ≈ 580.000).

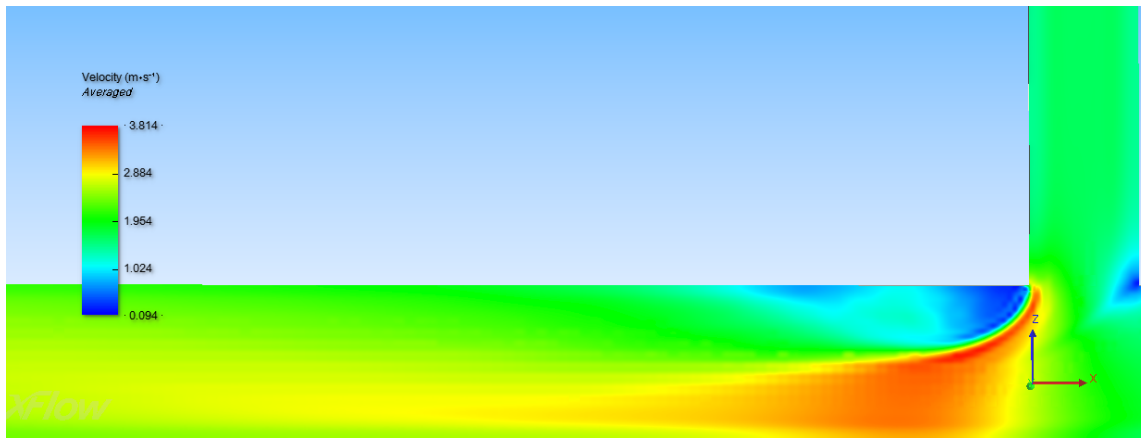


Figure 3.11: Average velocity in symmetry plane. XFLOW result of Case 3 (number of elements ≈ 580.000).

There is a clear difference notable in the extension of the separation bubble after the intersection. XFLOW tends to predict smaller separation bubbles than ANSYS (Figure 3.8) does in this case. Further, the Non-Equilibrium Enhanced Wall-function in Case 2 (Figure 3.10) shows an extensively developed boundary layer in the trim intersection and a very small separation bubble, leading to high thermal mixing as Figure 3.14 will show.

It is important to mention that the literature results from Frank et al. (2009) in Figure 3.8 are not to be seen as a reference, as they partially vary a lot from experimental results which will be depicted later on.

Temperature Fields

The temperature fields are presented in the same manner as the velocity fields. The time averaged temperature field is again plotted in the symmetry plane for ANSYS and XFLOW results.

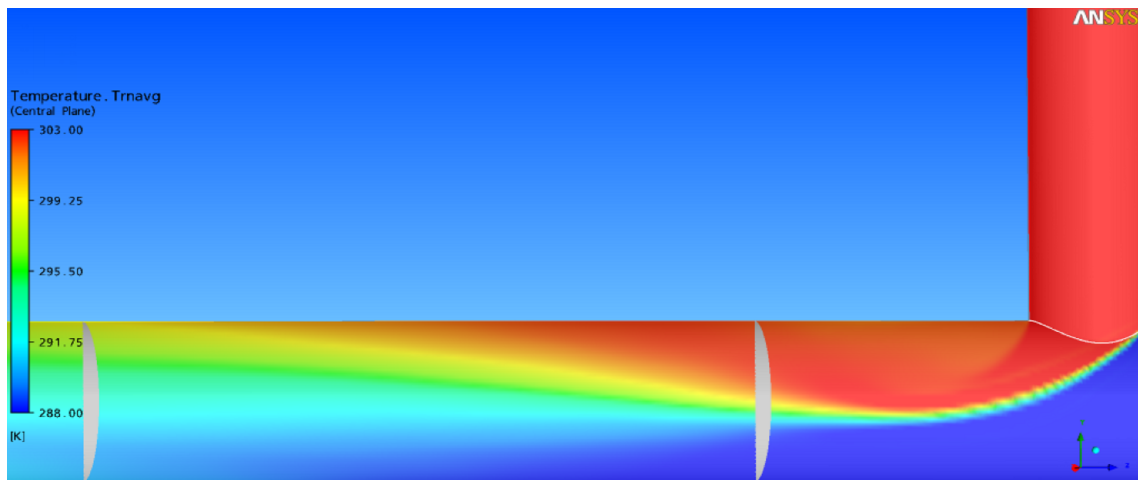


Figure 3.12: Literature results for average temperature in symmetry plane. Result from ANSYS with 2.256.320 mesh nodes (Frank et al., 2009, p.15).

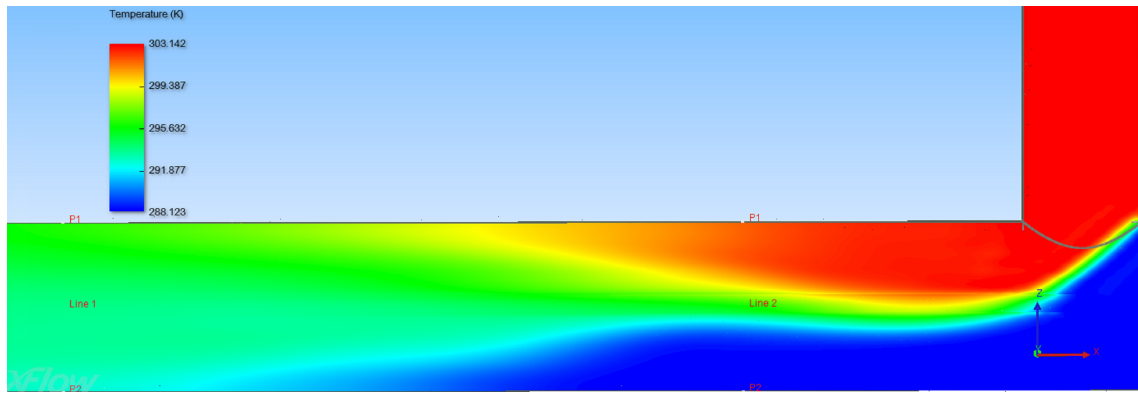


Figure 3.13: Average temperature in symmetry plane. XFLOW Case 1 results with ≈ 170.000 elements.

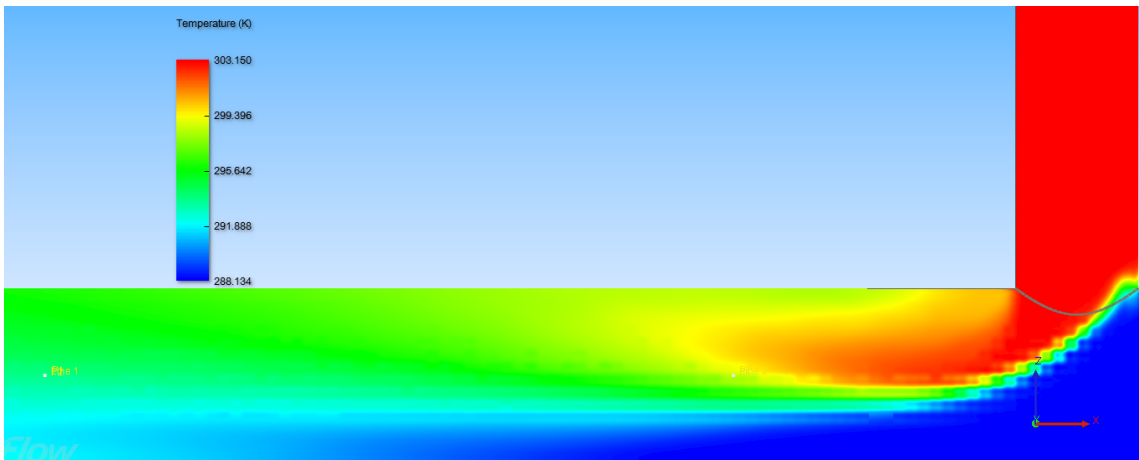


Figure 3.14: Average temperature in symmetry plane. XFLOW Case 2 results with ≈ 580.000 elements.

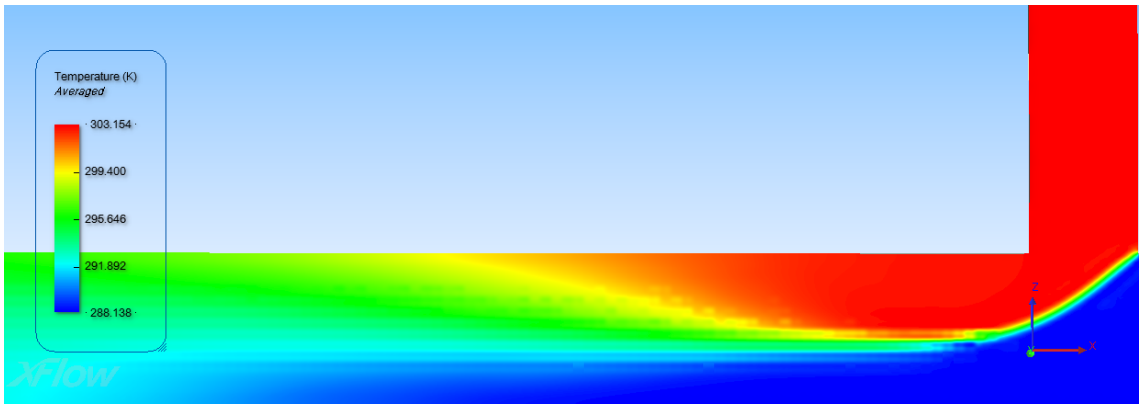


Figure 3.15: Average temperature in symmetry plane. XFLOW Case 3 results with ≈ 580.000 elements.

The symmetry plane temperature fields prove what is expected from the velocity fields in Figures 3.8-3.11. One can monitor that for Case 2 where a smaller separation bubble develops, the mixing distance is decreased. Figure 3.14 (Case 2) is the most extreme result as it has the smallest separation bubble downstream the intersection and the best thermal mixing.

Remember that apart the XFLOW version, the wall model is the only difference between Case 2 and Case 3. Case 2 has been repetitively executed with XFLOW v19 and only little impact on the results was monitored as can be seen in the comparison to experimental results in Figures 3.16 ff. The difference between the Enhanced Wall-function and the Non-equilibrium Enhanced Wall-function is that Non-equilibrium Enhanced Wall-function does take pressure gradients into account

whereas the Enhanced Wall-function does not. The Enhanced Wall-function is a simplification of the Non-equilibrium Enhanced Wall-function, which is well suited for complex flows with separations, reattachment and high gradients. This may lead to the assumption that the wall model of Case 2 is more trustful but the following comparison to experimental results will bring more clarity on that.

Comparison to Experimental Results

The data for experimental and ANSYS/FLUENT results from Frank et al. (2009) have been extracted to MATLAB with a very handy tool called “Plot Digitizer” in order to allow superposing and plotting together with other results from XFLOW in MATLAB.

For the following comparison to the experimental results a horizontal plotting line, normal to the xz-plane (compare Figure 3.10 for xz-plane) at station $z = 2.6D$ and another one at $z = 6.6D$ downstream the intersection is introduced, where D ...pipe diameter (140mm).

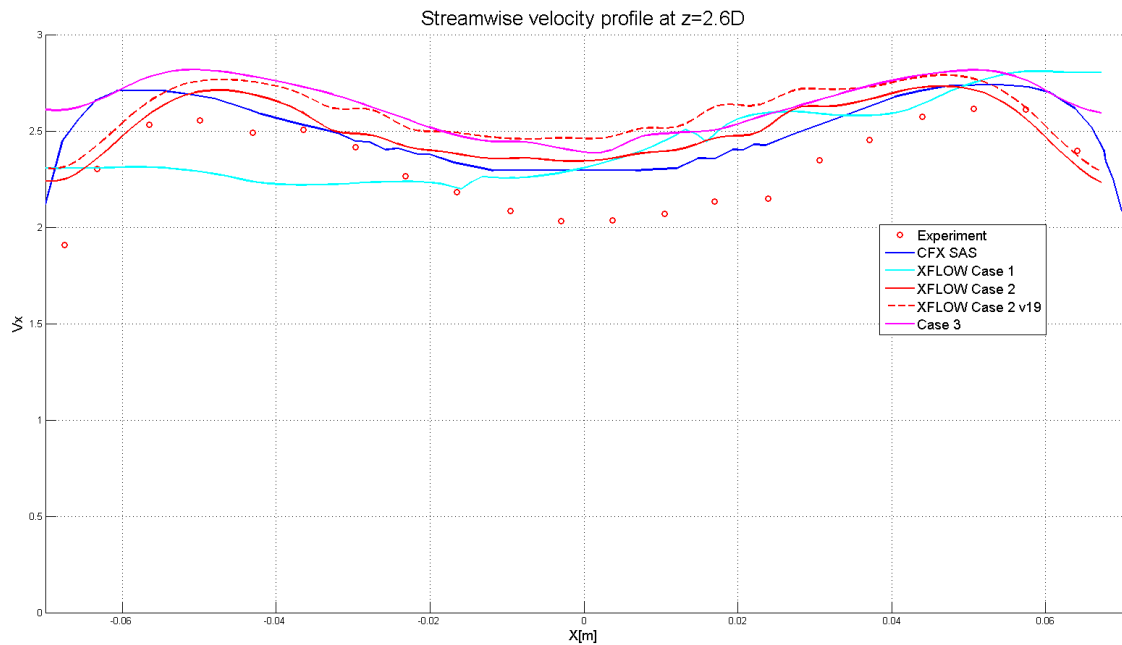


Figure 3.16: Average, streamwise velocity profiles at $z = 2.6D$ compared to experimental results. Experimental data and ANSYS CFX results are extracted from Frank et al. (2009,p.16).

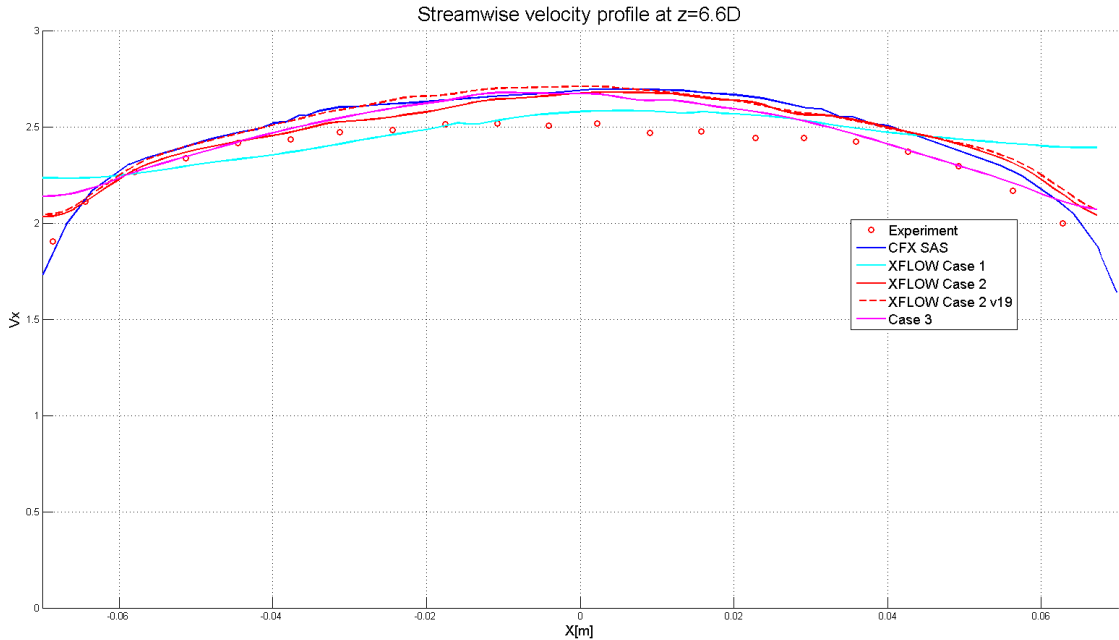


Figure 3.17: Average, streamwise velocity profiles at $z = 6.6D$ compared to experimental results. Experimental data and ANSYS CFX results are extracted from Frank et al. (2009,p.16).

Figures 3.16 and 3.17 show that there is a slight difference in the results of Case 2 between XFLOW v5 and XFLOW v19. But the difference will be negotiable for the results of the temperature fields in the following figures.

Both figures show strange behaviour of XFLOW's velocity fields near the wall, where the velocity usually should approach zero. Further, all results slightly over-predict the mean bulk velocity, which calls the accurateness of the experimental results into question. The velocity profile of Case 1 in Figure 3.16 leads to the assumption that the chosen resolution of Case 1 is too low.

As a next result the velocity fluctuations, calculated from velocity standard deviation (Route Mean Square - RMS) at the same cross section as the previous Figure 3.16 ($z = 2.6D$) is presented. Figure 3.18 shows that the velocity fluctuations are over-predicted by XFLOW, especially near walls.

The author wants to note that the standard deviation for a local sensor in XFLOW is calculated with the overall mean value and not the local mean value. Because of that, the standard deviation in Figure 21 was calculated manually for three different sensors.

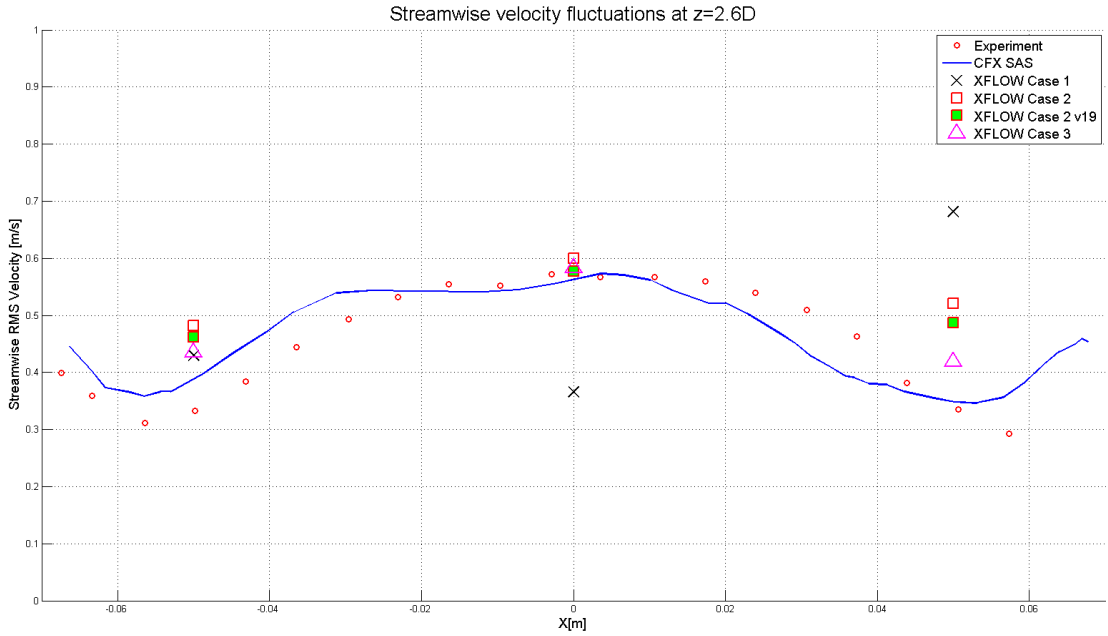


Figure 3.18: Streamwise velocity fluctuations at $z = 2.6D$ of XFLOW and ANSYS CFX compared to experimental results. ANSYS CFX results and experimental data are extracted from Frank et al. (2009,p.16).

The previous velocity and RMS profiles have shown that the models of Case 2 and Case 3 deliver quite similar results, close to but not fully complying with experimental data. As the temperature field in Figure 3.14 delivered different results from others it will be interesting to have a look at the wall temperature profiles now. Therefore 3 plotting lines, starting from the intersection and leading horizontally downstream for 10 diameters, are inserted. These 3 lines are located on top, left and bottom of the duct. The wall temperature T is normalized to:

$$T^* = \frac{T - T_{cold}}{T_{hot} - T_{cold}} \quad (3.13)$$

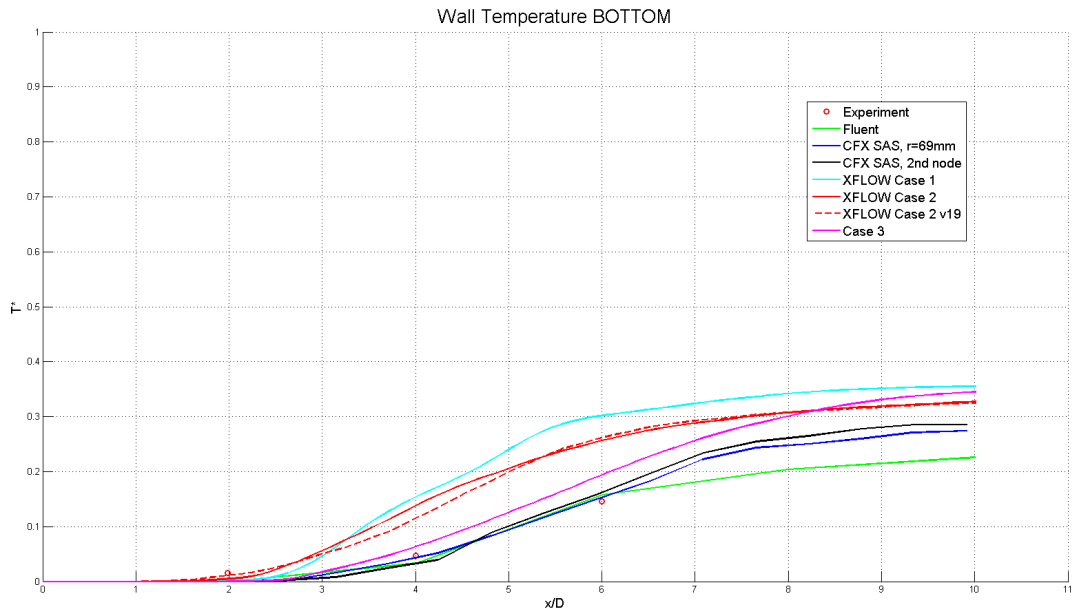


Figure 3.19: Bottom wall temperature of CFD simulations compared to experimental results. ANSYS CFX/FLUENT and experimental data extracted from Frank et al. (2009, p.19)

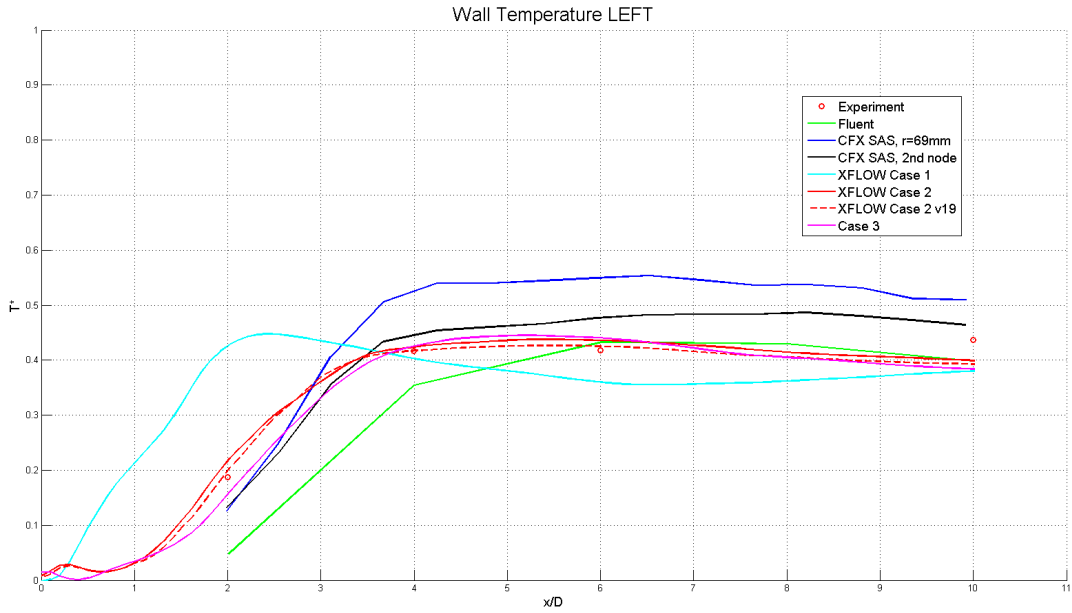


Figure 3.20: Left wall temperature of CFD simulations compared to experimental results. ANSYS CFX/FLUENT and experimental data extracted from Frank et al. (2009, p.19)

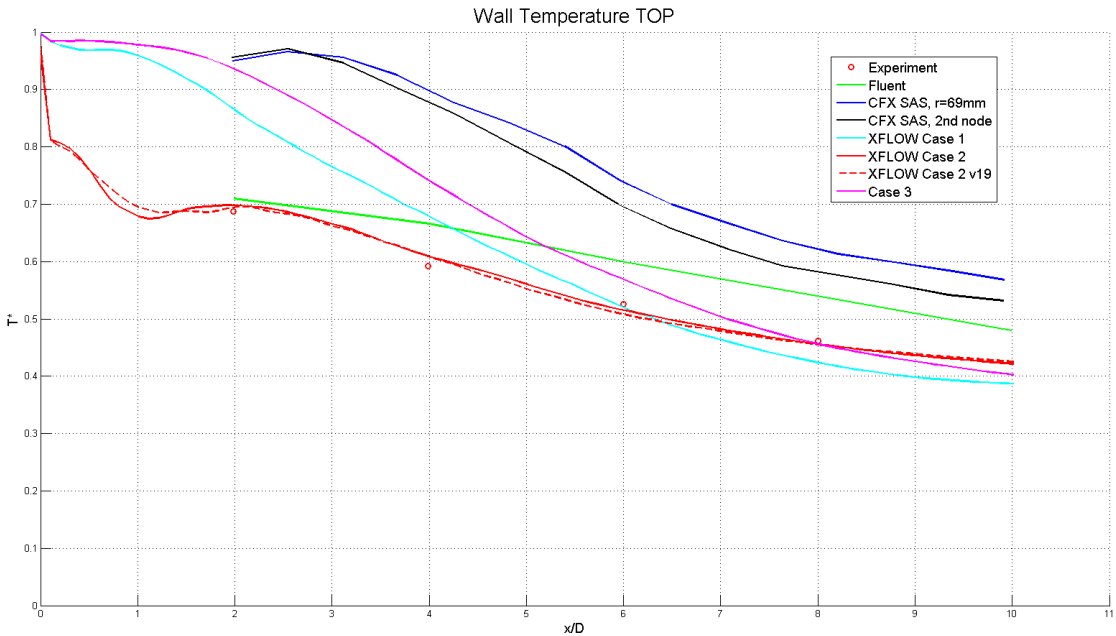


Figure 3.21: Top wall temperature of CFD simulations compared to experimental results. ANSYS CFX/FLUENT and experimental data extracted from Frank et al. (2009, p.19)

The Figures 3.19 to 3.21 show that none of the results fully complies with all experimental data. Fluent and CFX results manage to properly predict the bottom wall temperature but fail to do so for the left and especially for the top wall temperatures. XFLOW Cases 2 & 3 fit the left wall temperature surprisingly well. Case 2 also does so for the top wall temperature where Case 3 differs a lot. For the bottom wall temperature it is the other way around; Case 3 performs good whereas Case 2 fails to comply with measurements.

These circumstances do not allow to decide upon a suitable simulation setup. It is necessary to further increase the resolution and to do additional research on a Refined Case 2 and a Refined Case 3.

Further Investigation

As the previous discussion of results did not come to a conclusion, a refined setup of Cases 2 & 3 is necessary. Table 2 presents the simulation setup for the refined cases. To increase the resolution in the area of the injection a refinement region is defined with an extent as depicted in Figure 3.22.

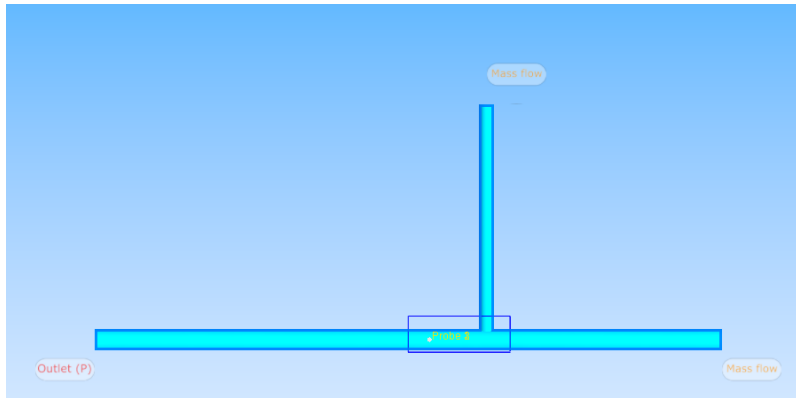


Figure 3.22: The blue rectangle represents the refinement region with constant resolution of 0.0025 m.

Table 2: Simulation setup for the Refined Cases 2 & 3

| Simulation | Refined Case 2 | Refined Case 3 |
|-------------------------|---------------------|-------------------------------------|
| Version | v19 | v19 |
| Turbulence Model | WALE | WALE |
| Wall Model | Enhanced Wall-model | Non-equilibrium Enhanced Wall-model |
| Resolution [m] | 0.01 | 0.01 |
| Wake resolution [m] | 0.0025 | 0.0025 |
| Wall refinement [m] | 0.0025 | 0.0025 |
| Resolution region 1 [m] | 0.0025 | 0.0025 |
| Transition length [-] | 3 | 3 |

The results of these simulations are depicted in the following figures. Due to a lack of time, the simulations were not completely finished and cancelled after 6 seconds. This means that the averaging time was only 4.5 s. Previous simulations have shown that the velocity and temperature profiles do not change remarkably after 6 seconds.

The averaged, streamwise velocity profiles for both Refined Cases 2 and 3, depicted in Figures 3.23 and 3.24, show best compliance with experimental measurements of all simulations conducted so far.

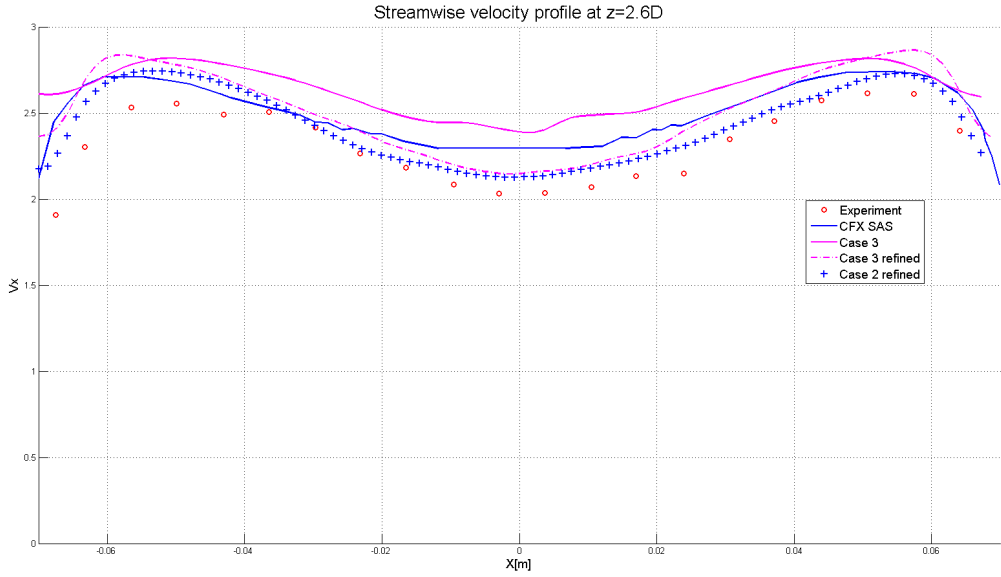


Figure 3.23: Time average streamwise velocity profiles for the refined cases. Only Case 3, which was best-complying from previous results, is depicted again for reference. The refined cases show very good compliance to experiments - best of all: Refined Case 2. Experimental measurements and ANSYS CFX results are extracted from Frank et al. (2009, p.16).

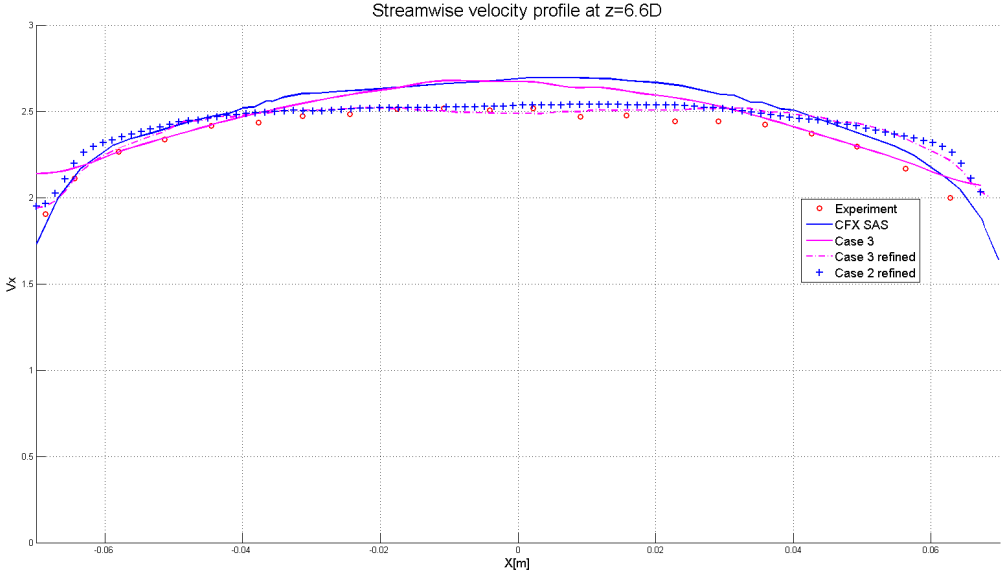


Figure 3.24: Best results also at $z = 6.6D$ for streamwise, average velocity. Also the near-wall velocity seems to be more physical as it tends to approach zero near the wall. Experimental measurements and ANSYS CFX results are extracted from Frank et al. (2009, p.16).

Finally, the wall temperatures for the refined cases are of interest. Remember that Case 2 has shown good results for the left and top wall temperature. Ideally, the appropriate model (Case 2 as it seems by now) approaches the experimental measurements for all locations now. The results for the top and left wall temperature are expected not to change, whereas the top wall temperature hopefully approaches to the values of the experimental data. The following final three Figures 3.25 through 3.27 for this test case shall bring clarity on that.

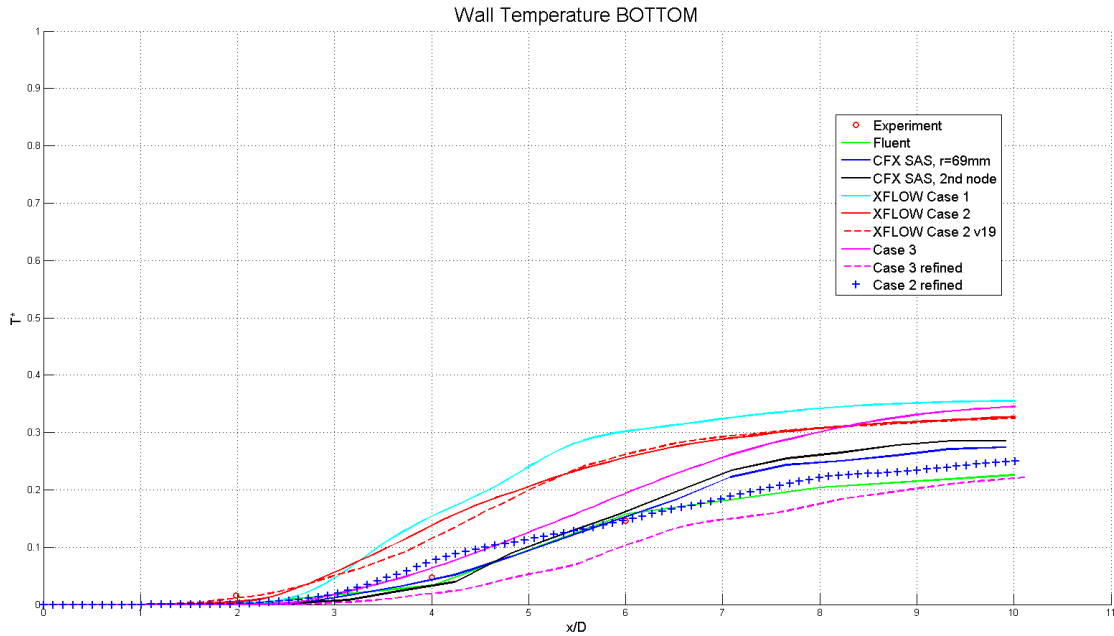


Figure 3.25: As expected, the bottom wall temperature for the Refined Case 2 is now in good compliance with the measurements. The Refined Case 3 slightly under-predicts the actual temperature. Experimental data and ANSYS FLUENT/CFX results according to Frank et al. (2009, p.19).

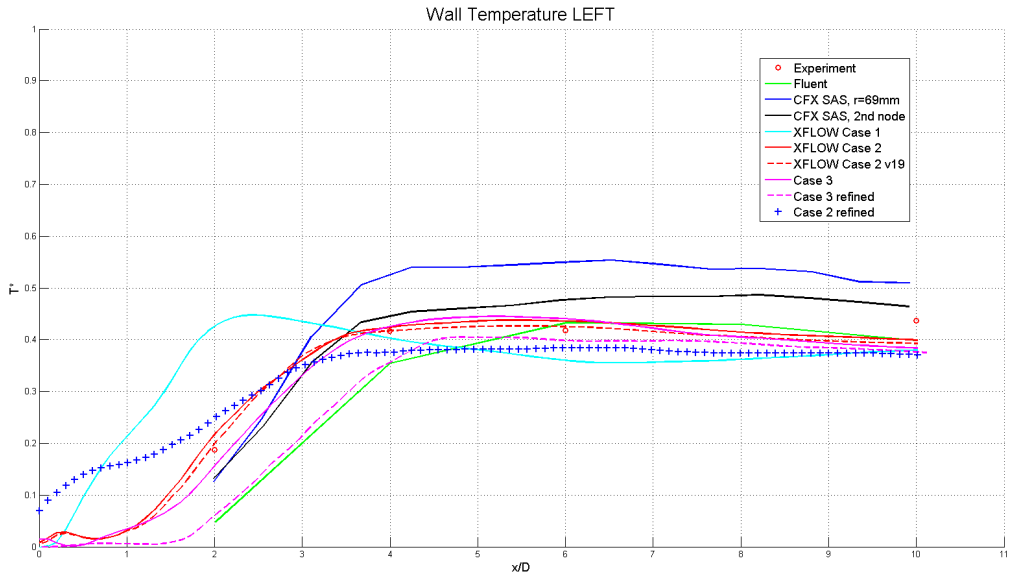


Figure 3.26: As the Refined Case 2 deviates slightly more from measurements than Case 2 these results differ from what is expected. But still the Refined Case 2 performs better than the Refined Case 3. Experimental data and ANSYS FLUENT/CFX results according to Frank et al. (2009, p.19).

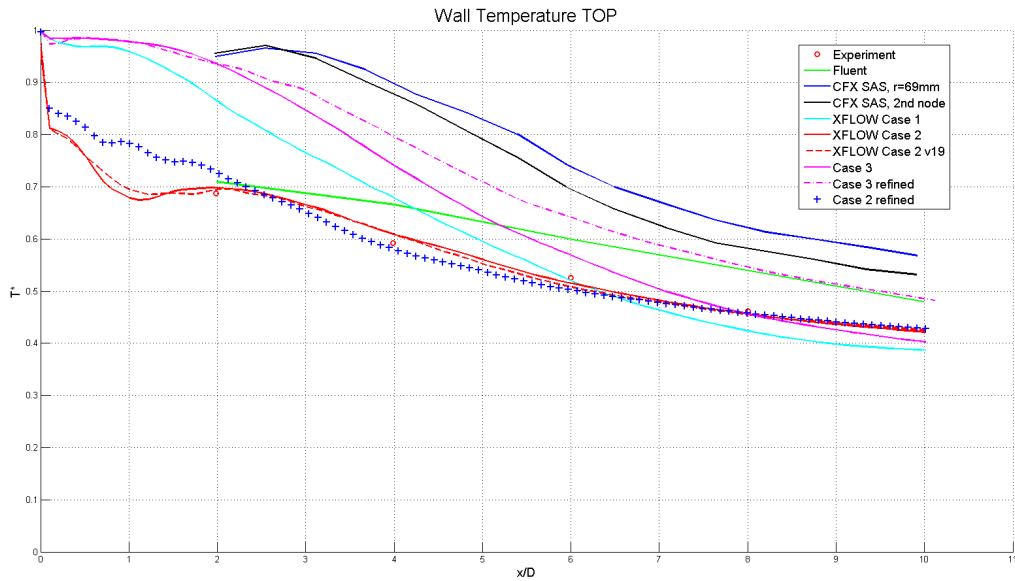


Figure 3.27: The Refined Case 3 fails to predict the top wall temperature whereas the Refined Case 2 remains in good compliance with the experimental data. Experimental data and ANSYS FLUENT/CFX results according to Frank et al. (2009, p.19).

3.1.3 Summary of T-Junction Investigation

The test cases were executed in order to find the most suitable simulation setup for the investigation of the TCS. In the beginning three cases with two different wall models and different resolutions were simulated. As both models only partly complied with the results from the literature, the resolution was refined according to Table 2. Finally, the wall temperature profiles for the refined cases in Figures 3.25, 3.26 and 3.27 have brought clarity.

The reader might wonder why only the wall model and not the turbulence model itself was varied during the simulations. It was not mentioned earlier that, by the way, the Smagorinsky and Dynamic Smagorinsky turbulence-models were simulated with setup of Case 3. Both models failed to predict more accurate results concerning the wall temperatures. Only slight differences, similar to the deviations between Case 2 v5 and Case 2 v19 were noticed. But both models have not been investigated on higher resolution and with the appropriate wall model, the Non-equilibrium Enhanced Wall-function. This could be a starting point for further investigations in the future.

To sum up the results of the refined cases there is to say, that the velocity profiles of both wall models show very good compliance to the literature; better than all simulations before. On the other hand, the temperature predictions for the Enhanced Wall-function (Refined Case 3) differ a lot from what is expected. The Non-equilibrium Enhanced Wall-function, applied in Refined Case 2, shows the best results in all aspects. In other words: the setup of Refined Case 2 with the Non-equilibrium Enhanced Wall-function seems to be an appropriate setup for such problems of turbulent, thermal mixing. The Enhanced Wall-function shows good results for the velocity profiles but the temperature cannot be predicted properly in this case.

Based on this results, the simulation setup for the simulation of the TCS will be similar to the Refined Case 2, using the Non-equilibrium Enhanced Wall-function.

3.2 Investigation of Trim Tapping Design

Another uncertainty is the design of the trim tapping - the design of the trim intersection. It can be either designed using a sharp edge or a rounded edge. For sure a trade-off between production costs and pressure loss has to be made. The sharp edge will lead to lowest production costs as only a hole has to be drilled but the effect on the pressure loss is unknown. In an investigation of the trim tapping these gains and losses are to be quantified. The simulation is executed in ANSYS CFX with the non-transient Reynolds Average Navier Stokes (RANS) model.

3.2.1 Geometry and Setup

Figure 3.28 will give an overview on the simplified geometry. A simple, circular, straight duct with a smaller circular duct as trim inlet is modelled once with sharp

intersection and once with a 5 mm radius at the intersection.

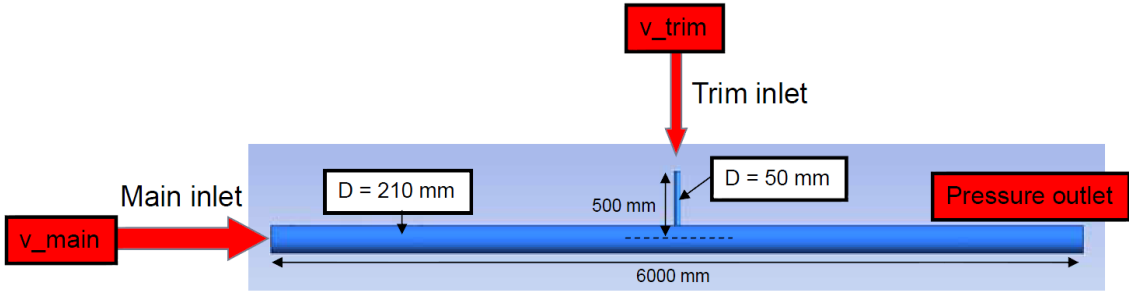


Figure 3.28: A detailed overview of the geometry with dimensions and boundary conditions for the trim tapping investigation.

Two different inlet flows are considered with 0 g/s and 20 g/s, respectively. The boundary conditions for the simulations are set to:

- Main inlet: inlet velocity (650 l/s @ 15 °C)
- Trim inlet: inlet velocity (0 g/s | 20 g/s @ 150 °C)
- Outlet: 0 Pa average relative pressure
- Reference pressure: 1013 hPa
- Mesh: ≈ 4 Mio unstructured elements

3.2.2 Results of Trim Tapping Design Investigation

As a result of the investigation the total pressure field in the plane of symmetry is plotted for the sharp (Figure 3.29) and the rounded (Figure 3.30) pipe with 20 g/s trim flow. A slightly decreased separation bubble for the rounded intersection can be monitored which later on leads to a decreased total pressure loss.

In case of a trim intersection the total pressure loss is not the only important objective function for optimization - the efficiency of thermal mixing and noise abatement are important factors that have to be considered as well. Within this investigation no acoustic analysis is executed. This means that the acoustic factor is still an uncertainty for evaluation. The author expects that the sharp trim tapping produces more noise than the rounded but it is difficult to estimate this quantitatively. For a more detailed research it would be necessary to execute a transient - acoustic analysis as well.

Nevertheless, a thermal analysis has been executed and as Figures 3.31 and 3.32 show, surprisingly, the radius prohibits thermal mixing. The distance for thermal mixing increases as comparison of these figures indicates.

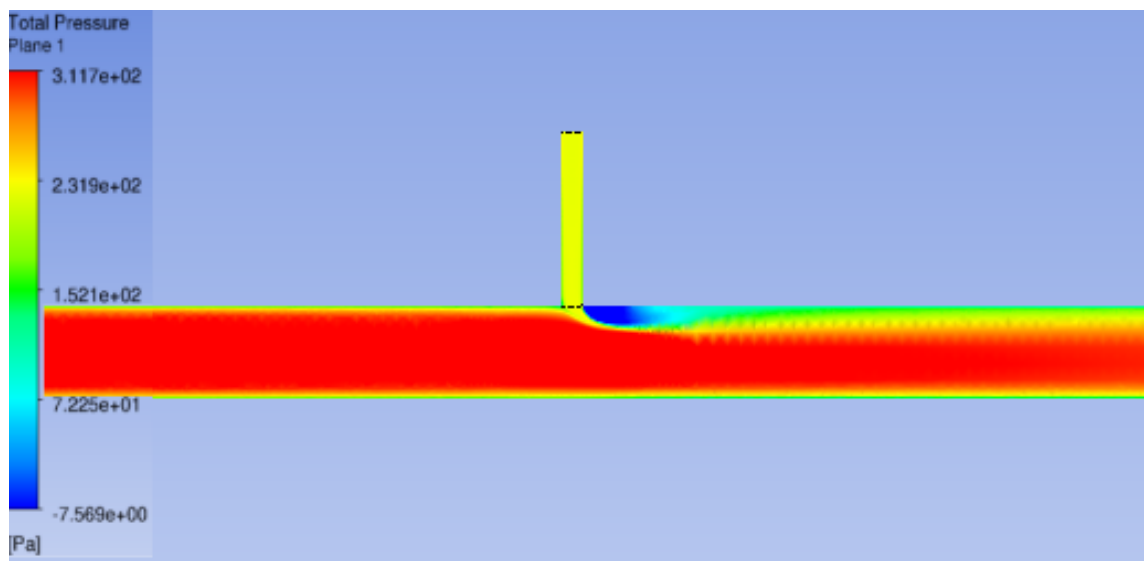


Figure 3.29: The total pressure field for the sharp trim tapping shows a slightly bigger area of separation downstream the tapping.

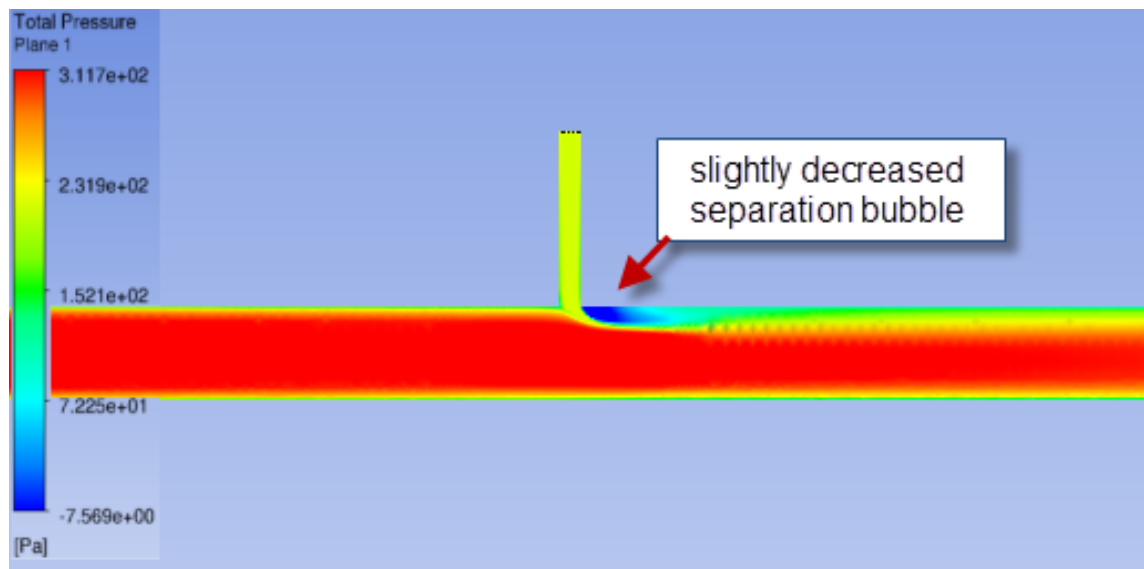


Figure 3.30: Total pressure field for the 5 mm rounded trim tapping.

Table 3: Resultant pressure loss for the two cases of 0g/s and 20g/s for each geometry. The reference pressure is 1013 hPa.

| Geometry | Trim Flow [g/s] | Total Pressure Main Inlet [Pa] | Total Pressure Side Inlet [Pa] | Total Pressure Outlet [Pa] | Total Pressure Loss [Pa] | Total Pressure Loss in % |
|----------|-----------------|--------------------------------|--------------------------------|----------------------------|--------------------------|--------------------------|
| Sharp | 0 | 300.816 | - | 213.717 | 87.099 | 28.95% |
| Round | 0 | 298.444 | - | 213.432 | 85.012 | 28.49% |
| Sharp | 20 | 339.551 | 231.485 | 228.617 | 342.419 | 59.96% |
| Round | 20 | 329.884 | 211.602 | 229.597 | 311.889 | 57.60% |

Table 3 indicates 2.5% gain in total pressure at the outlet if the trim flow is 0 g/s and with 9.8% slightly more gain in case of a trim flow of 20 g/s. 9.8%, or approximately 30 Pa in this case, may not seem to be a remarkable improvement. Only in case there were several trim tappings in serial the sum of the total pressure gains would sum up to noticeable values. In this case, with 30 Pa the gain is probably not worth the drawbacks a rounded trim tapping brings with.

Finally, the results of the thermal analysis are depicted in the following figures. As already mentioned, the distance for thermal mixing increases if a radius is used. This certainly is not a desired effect as the goal is to minimize the distance for thermal mixing in order to ensure uniform temperature at the outlet. It is now necessary to make a trade-off between the gain in terms of pressure loss and the loss in terms of thermal mixing.

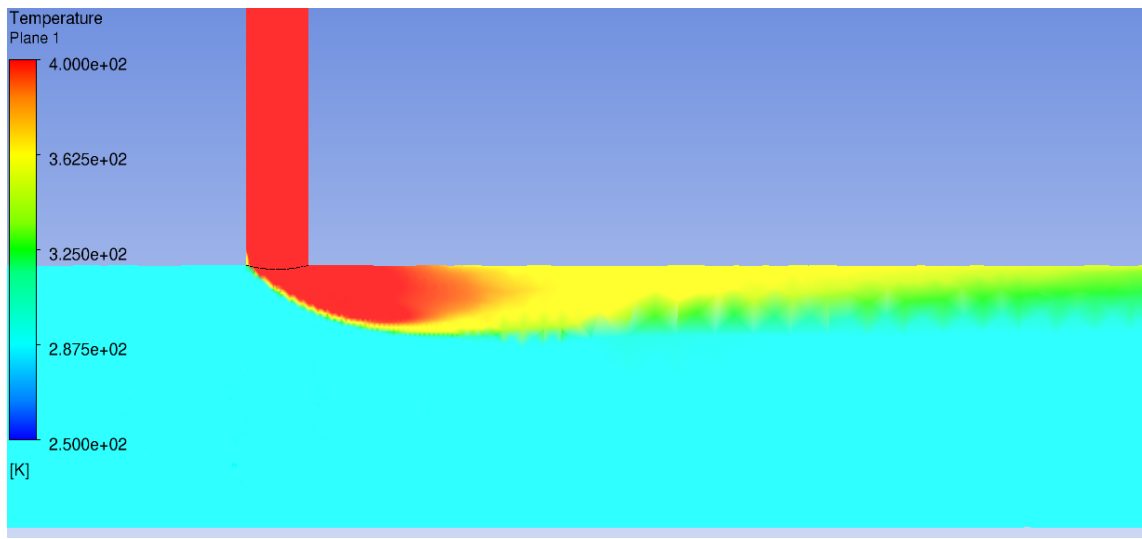


Figure 3.31: Temperature profile for the sharp trim tapping. The hot stream at a trim flow of 20 g/s shows less longitudinal extent than the rounded trim tapping below.

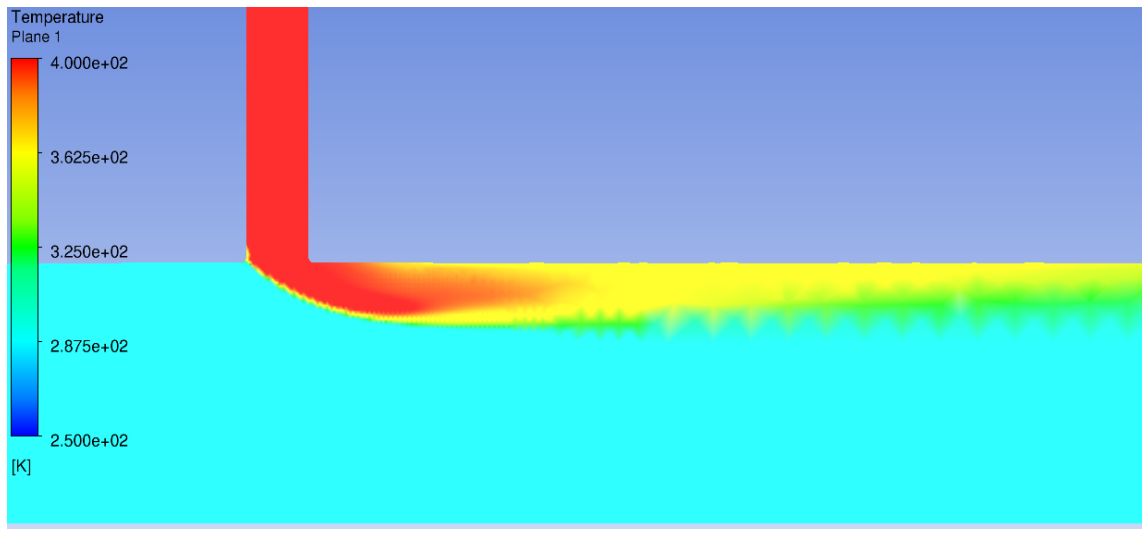


Figure 3.32: Temperature profile for the rounded trim tapping at a trim flow of 20 g/s. Comparison to Figure 3.31 yields that the radius increases the distance for thermal mixing.

3.2.3 Summary of Trim Tapping Investigation

The trim tapping investigation was executed to quantify the effects of rounding the intersection at the trim tapping, where the trim pipe enters the main duct.

Two different states with different trim flows of 0 g/s and 20 g/s, respectively were investigated on the sharp edge and the rounded edge with 5 mm radius.

The results for the thermal analysis and the analysis of the total pressure loss were depicted within the previous sub-section and it can be summarized that a radius at the trim tapping:

- decreases thermal mixing
- increases production costs
- decreases the total pressure loss

Further, the effects on noise emission is unknown but certainly is not an unimportant factor and should be drawn for consideration for final decisions. Depending on the detailed geometry and weighting of the different factors a decision has to be made individually and no unique recommendation is possible.

3.3 Investigation of the TCS

This section introduces into the main issue of this paper; the thermal investigation of the TCS. It was already mentioned earlier that there are seven temperature zones plus extra ducting for other purposes. All TZ are basically investigated at two different conditions/trim flows. First, a high trim flow at a mass flow rate of approximately 40 g/s and second, a low trim flow of approximately 10 g/s, depending on the main mass flow rates of the different zones. Finally, what is of interest, is the temperature at the location of the temperature sensor. Therefore, all cases are simulated on the “XFLOW-LES” scheme with a simulation time of 2 s.

3.3.1 Geometry and Setup

The overall geometry was already depicted graphically in the introductory section in Figure 1.1. For the investigation of the different TZ only the ducting after the main mixing unit is considered individually for each TZ.

The following list describes the basic XFLOW simulation-setup valid for all simulations carried out within this investigation:

- Flow model: 3d-single phase internal
- Thermal model: Segregated energy without radiation
- Turbulence model: WALE without initial turbulence
- Initial gauge pressure field: (relative pressure) 0 kPa
- Initial temperature field: 283.15 K
- Fluid: Air 28.996 u

- State equation: Reference static pressure 80 kPa
- Newton viscosity model: $\mu = 1.7894e - 05 \text{ Pa} \cdot \text{s}$
- Thermal conductivity: 0.0243 W/(mK)
- Specific heat capacity: 1006.43 J/kgK
- Main inlet: velocity according to mass flow at $T = 283.15 \text{ K}$
- Trim inlet: velocity according to mass flow at $T = 453.15 \text{ K}$
- Outlet: Adiabatic gauge pressure outlet (ratio= 0.5) 80 kPa
- Wall: Adiabatic Non-equilibrium Enhanced Wall-function with zero roughness

The simulation time is 2 s for all cases and the resolution varies from zone to zone, depending on the overall size and complexity of the geometry. The refinement algorithm in use is the refinement near walls algorithm which results in constant numbers of mesh elements. The adaptive wake refinement would result in increasing number of mesh elements after some time and further, distributed computation is not possible with it.

The time step is set manually at fixed custom value resulting in a stability parameter below 0.2. For many cases the time step was set to $1e - 05 \text{ s}$. Finally, averaging is started after 0.5 s of simulation time.

After the general simulation setup is clarified, now the boundary conditions for the different zones are listed in the table below. The flows of the main pipes are chosen by averaging nominal values for the A350-800, -900 and -1000. With the diameters, measured in CATIA, the volume-/mass-flow can be converted into velocity boundary conditions.

A disadvantage of current XFLOW versions is that the velocity at an inlet can only be defined by vector components. This works fine for simple, rectangular geometry which is aligned to coordinate axis but for complex geometry with arbitrary orientation in space one has to evaluate the normal vector of every inlet before the components of the velocity can be split up. For further implementations it would be a nice feature if one could declare velocity boundary conditions normal to surfaces.

Table 4: Volume and mass flows for all different zones which need to be converted to velocities.

| Zone | Main [l/s] | Trim - Case 1 [g/s] | Trim - Case 2 [g/s] |
|------|------------|------------------------|------------------------|
| TZ 1 | 585.67 | 10 | 40 |
| TZ 2 | 525.00 | 10 | 40 |
| TZ 3 | 560.33 | 10 | 40 |
| TZ 4 | 570.67 | 10 | 40 |
| TZ 5 | 703.00 | 10 | 40 |
| TZ 6 | 643.33 | 10 | 40 |
| TZ 7 | 659.00 | 10 | 40 |
| FCRC | 50.00 | 5 | 10 |
| CCRC | 463.33 | 10 | 40 |
| F/D | 185.00 | 10 | 15 |

3.3.2 Hardware Issues and Cluster Problems

It was intended to run all XFLOW simulations on parts of a 128 core Linux cluster. A job scheduler should distribute resources and the distributed computation should be handled by Open-MPI v1.4.2. Unluckily the author had to face serious problems with distributed computation on the cluster which could not be resolved during the period of the internship.

There seemed to be a problem regarding communication between the different nodes of the cluster. Each of the 32 nodes runs on 4 CPU's which sums up to 128 cores. Distributed computation within one node (shared memory) was no problem but as soon as a second node was pulled up, the computation froze. This fact brought some serious cutbacks because computation could only be carried out on 4 nodes. Due to this strong limitation in CPU resources the author could not everywhere use as high resolutions as partly necessary and only parts of all planned investigations were executed.

During the simulations also software problems appeared. These problems and the final results will be depicted in the following section.

4 Results

Apart from the problems that appeared on the cluster there were also problems concerning XFLOW. All results show tremendous problems concerning the boundary conditions. The fluid domain shows immense pressure fluctuations and also the outlet mass flow is highly fluctuating. Referring to Figure 4.33, the fluctuations in TZ 4 appear with magnitudes over 1 kPa.

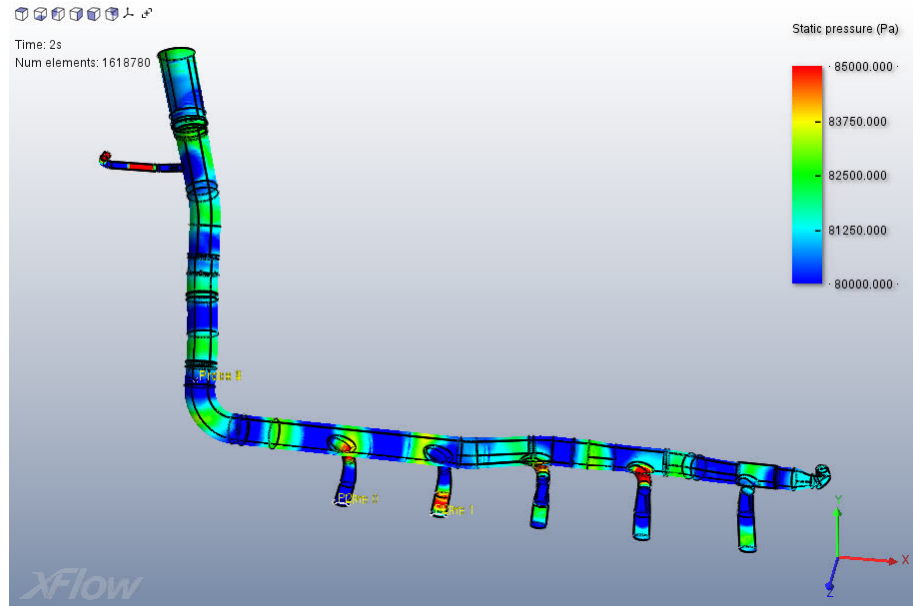


Figure 4.33: The first results with ordinary velocity boundary conditions show immense pressure fluctuations.

As a countermeasure, the inlet mass flow was increased linearly through the first 0.5 s until the desired value was reached. In XFLOW one can define functions on any input which has squared brackets. The ramp function is then defined to: $if(t < 0.5, 2 \cdot t \cdot M, M)$. Which means nothing else than, as long as the time t is less than 0.5, the mass flow has the value $2 \cdot t \cdot M$, where M is the final, desired mass flow, and after $t = 0.5$ s the mass flow remains at a constant value M . This measure brought some improvements but the fluctuations could not be abolished totally. Figure 4.34 depicts the static pressure of the probe located at the temperature sensor.

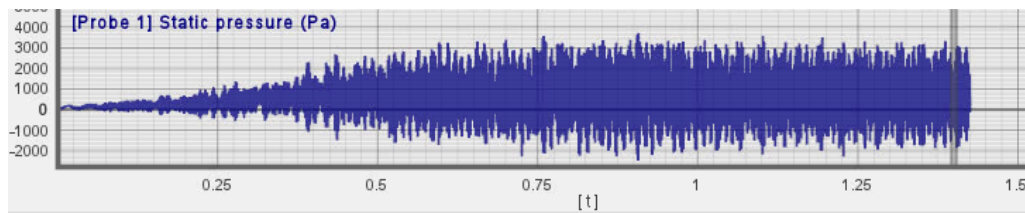


Figure 4.34: Pressure fluctuations at the probe located at the temperature sensor.

Further, in the beginning, there was no relation between the mass flow and the velocity at the inlet. For a given density ρ one can convert the mass flow to a volume flow Q which can further be converted to an inlet-velocity c for a given inlet area A , by $c = \frac{Q}{A}$.

For example, at TZ 3 according to the simulation results, at the inlet, the air has the following state:

- Total pressure $p_{tot} = 80200$ Pa
- Temperature $T = 283.15$ K

Via the state equation of the ideal gas, the density can be calculated which results in $\rho = 1.01 \text{ kg/m}^3$. With a given inlet-area $A_{in} = 0.039\text{m}^2$, the resulting, theoretical velocity for a mass flow of 0.571 kg/s is $c_{theoret} = 14.32 \text{ m/s}$. In the simulation, where a mass-flow inlet boundary-condition is used, only an average velocity of $c_{sim} = 2.1 \text{ m/s}$ can be monitored.

In the end it turned out that the pressure gauge for the initial condition and at the outlet is defined as relative pressure and not as absolute pressure. Also the pressure indication for the results is always relative pressure. The operating/reference pressure is defined via the fluid properties. Unluckily, the author could not find any information on this in the user manual and had to find out via trial and error.

Finally, one problem concerning the temperature boundary condition appeared sometimes if the mass flow boundary conditions was set instead of velocity condition at inlets. In some cases the results were similar to Figure 4.35, where the temperature is stuck to the inlet and is not transported with the fluid.

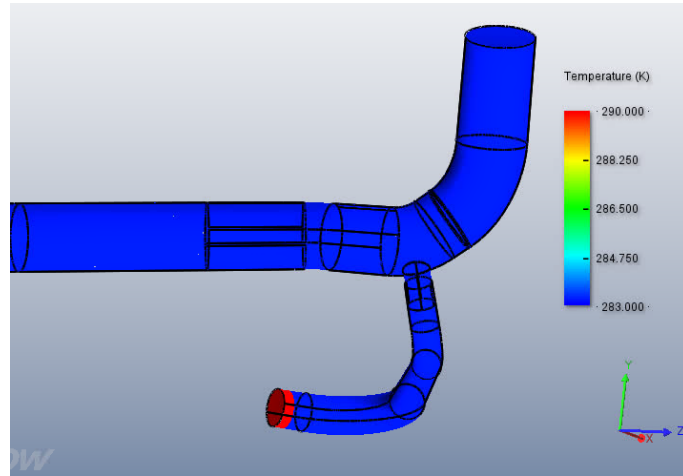


Figure 4.35: After 2 s of simulation time the temperature is still not carried inside by the fluid although the inlet speed is several m/s.

For all simulations the operating pressure is 80 kPa and all boundary conditions are implemented as follows:

- Main inlet: Velocity according to Table 4 @ $T = 283.15$ K
- Trim inlet: Velocity according 2 cases for high and low trim flow depicted in Table 4 @ $T = 453.15$ K
- Outlet: Pressure gauge: 0 Pa relative pressure and damping coefficient of 0.5

To analyse the results, each temperature sensor in every TZ has 4 probes located at the 4 sensor nodes to monitor the indicated sensor temperature. Also, on each outlet a plotting line is inserted in order to extract the outlet temperature profiles (depicted in Figure 4.43).

For all cases a summarizing table which depicts all theoretical and measured temperatures can be found at the end of the results section where also a theoretical mixing temperature is listed. This theoretical temperature can be calculated to,

$$T_{theory} = \frac{\dot{m}_{main}T_{main} + \dot{m}_{trim}T_{trim}}{\dot{m}_{main} + \dot{m}_{trim}} \quad (4.14)$$

where \dot{m} denotes the mass flow and subscript main and trim represent main flow and trim flow.

Finally, there is to say, that the impact of the non-physical pressure fluctuations on the temperature field is not known in detail and the results are to be taken with care! Only at the very end of the internship it turned out that the used wall model caused the pressure fluctuations. The reader may find a comparison of proper and improper pressure field results and the influence on the temperature field for TZ 3, TZ 4 and F/D within section 4.13 - Remark on Results. All other results presented prior to section 4.13 are influenced by the pressure fluctuations.

4.1 TZ 1

For this very first zone the pressure, velocity and temperature fields will be depicted whereas later on only the temperature fields will be shown. It will be shown that averaging results in more plausible pressure and velocity fields than the instantaneous data which is dominated by numerical instabilities.

40 g/s trim flow

A trim flow of 40 g/s is necessary to raise the initial temperature of 283.15 K to a theoretical mixing temperature of 293.8 K. As for all other zones (if not denoted differently) a resolution of 0.01 m in the far-field with wall-refinement of 0.005 m is chosen.

Because of the problems with distributed computation on the cluster and a lack of time it was not possible to continue further investigations on higher resolutions.

Figure 4.36 shows the instantaneous static pressure field after 2 s. The next Figure 4.37 depicts the same field but with average values. It can be seen that the averaging process results in more plausible fields and the numerical instabilities vanish.

In Figure 4.36 the restrictor and the sensor have no impact on the total pressure field whereas in Figure 4.37, the regions of dead air behind the restrictor, the trim intersection and the sensor are plausibly predicted.

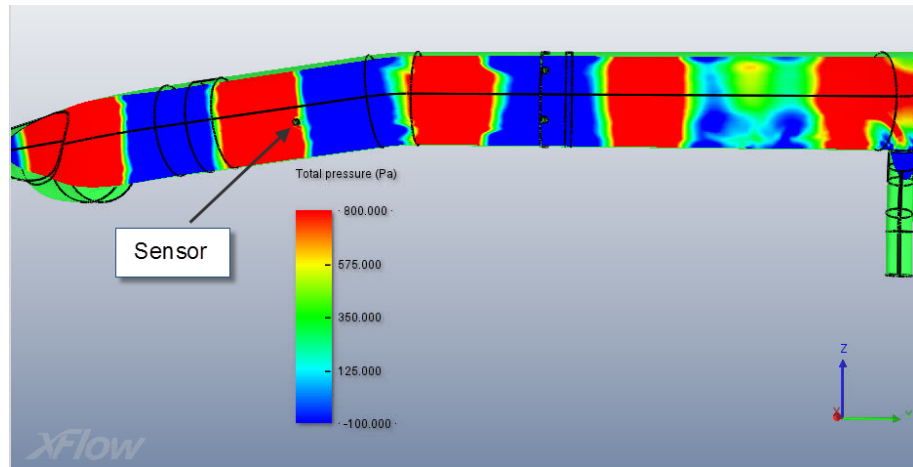


Figure 4.36: The instantaneous total pressure field of TZ 1 yields huge numerical instabilities.

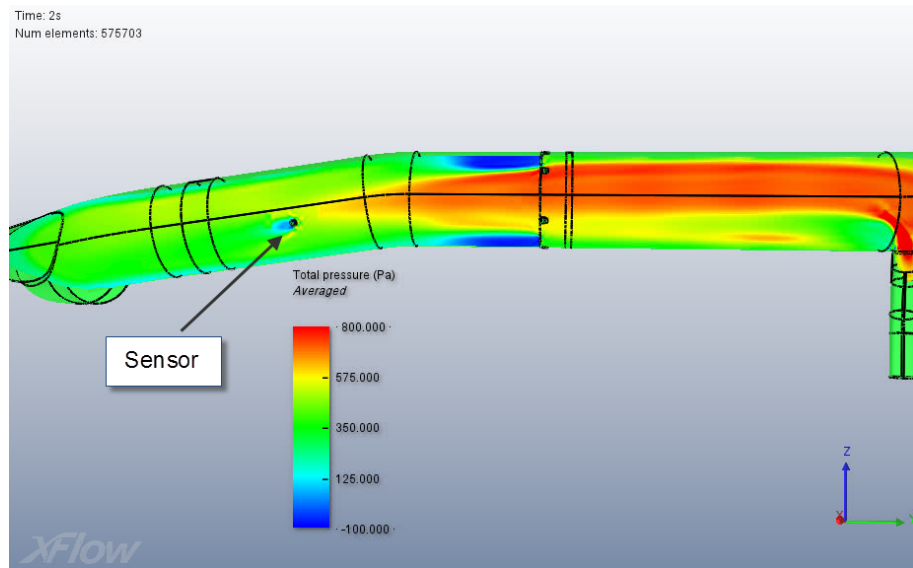


Figure 4.37: By averaging, most numerical instabilities vanish. Nevertheless, there is a big uncertainty to estimate the influence on the temperature field.

In the averaged static pressure field (depicted in Figure 4.38), the stagnation areas in front of the sensor and the restrictor also seem to be predicted properly.

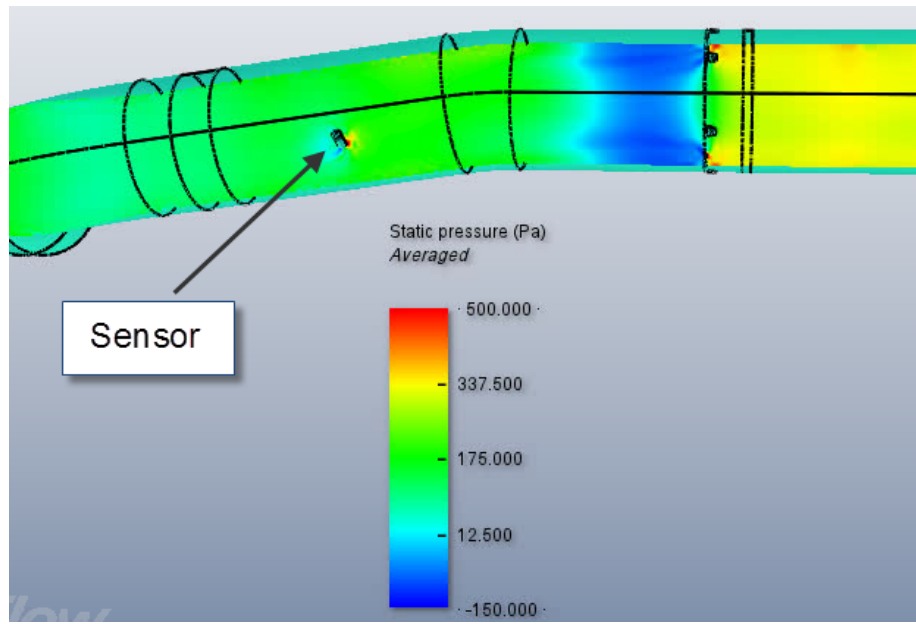


Figure 4.38: The static pressure around the sensor and the restrictor seems to be plausible for the averaged field.

The longitudinal temperature field in Figure 4.39 shows that the restrictor has positive impact on thermal mixing. In some zones, where the sensor temperature deviates from the ideal mixing temperature, the restrictor is installed downstream the sensor. According to Figure 4.39, shifting of the restrictor upstream the sensor might improve thermal mixing at the sensor cross section.

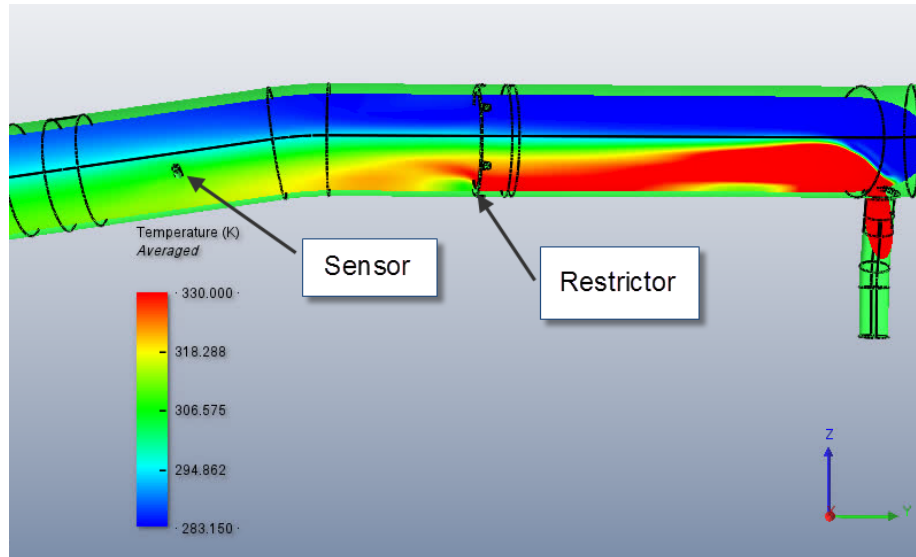


Figure 4.39: The restrictor has positive impact on thermal mixing.

Analysis of the temperatures at the sensor and the outlet brings up that the sensor

temperature is 305 K which is 11 K above the ideal temperature. At the outlet the average temperature of the plotting line is 300 K.

10 g/s trim flow

For the low trim flow, the flow profiles look quite similar to the previous case but the temperature profile is different. The theoretical temperature is calculated to 286 K. Both, the temperature at the sensor and the outlet temperature only vary approximately 0.5 K around this value.

The longitudinal temperature profile in Figure 4.40 shows that there is a small, hot stream which remains attached to the wall of the main duct until it is mixed because of the influence of the restrictor, which again plays an important role in this case.

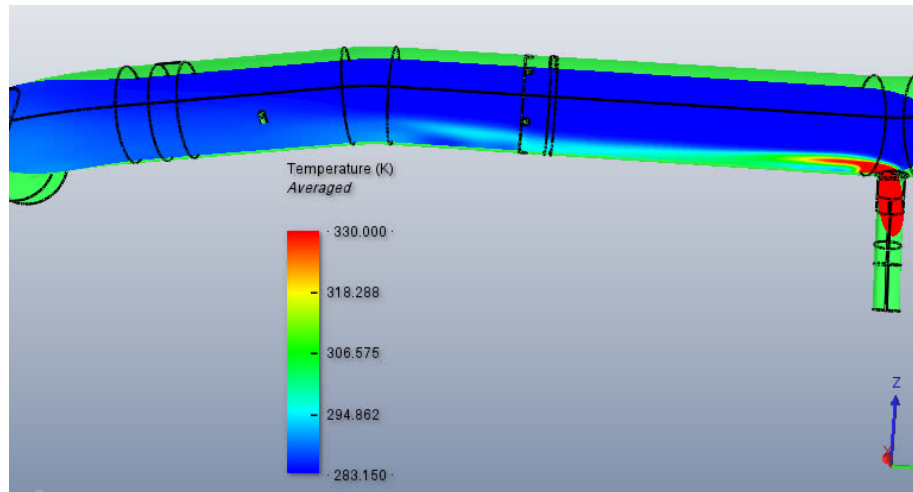


Figure 4.40: Average temperature profile for the low trim flow in TZ1.

A summary table for all cases which includes all measured temperatures can be found at the end of the Results section, in the subsection Summary of Results.

4.2 TZ 2

TZ 2 is simulated at the standard resolution of 0.01 m with wall refinement of 0.005 m. The simulations show unphysical pressure fluctuations also within this zone and predict big deviations between the sensor temperature and the mixing temperature.

40 g/s trim flow

The high trim flow of 40 g/s results in a theoretical mixing temperature of 295 K. The average sensor temperature is measured 13 K too high at 308 K. The outlet temperature is 304 K and quite uniform over the diameter. Obviously, the outlet temperature and the theoretical mixing temperature do not correspond. One reason

could be that the density at the inlet might vary from assumed values. Monitoring the hot trim inlet mass flow confirms this as the flow is around 50 g/s and not 40 g/s. Nevertheless, this does not explain the difference of 9 K between the outlet and the theoretical temperature.

As a result the average wall temperature is plotted in Figure 4.41. One can see that the trim injection is located at the inner side of the first bending of the main pipe (where the temperature sensor is located). If the trim inlet was located at the other side of the main pipe, inertia and density related buoyancy effects between cold and hot fluid would lead to better thermal mixing caused by the bending. At a bending cold air with higher density always displaces hot air to the inner side of the bending. In this case the hot air already is at the inner side of the bending, leading to no big influence of the bending on thermal mixing. In contrast, see Figure 4.58, where the bending leads to additional buoyancy related mixing.

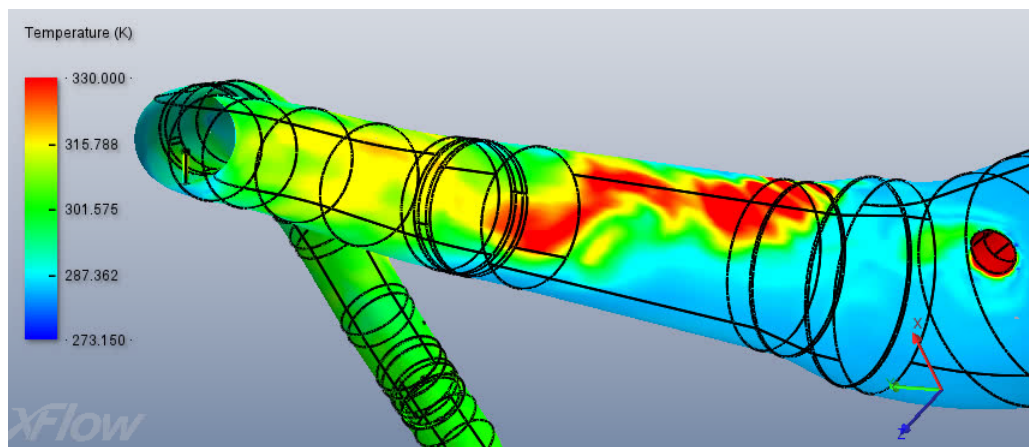


Figure 4.41: Wall temperature for TZ 2.

10 g/s trim flow

For the low trim flow the same phenomenon leads to a hot stream attached to the inner side of the bending of the main wall as Figure 4.42 shows. Because the hot stream for the low trim flow is smaller it does not reach the sensor and the temperature does not deviate too much from theoretical temperature which is calculated to 286 K. The sensor temperature is 3 K higher at a temperature of slightly above 289 K.

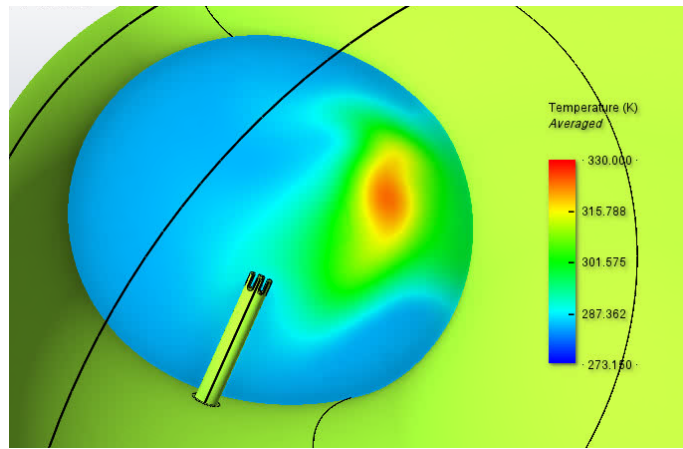


Figure 4.42: The temperature profile at the sensor cross section depicts the hot stream of lower density which is displaced even more to the inner side of the bending by the cool air due to buoyancy effects.

4.3 TZ 3 (non humidified)

TZ 3 is a critical zone because of 6 individual riser ducts which are located close to the trim tapping. At the beginning of branch 1 the fluid already has to be mixed well in order to avoid diverse temperatures in the riser ducts.

40 g/s trim flow

Figure 4.43 depicts the location of the plotting line at the outlet, where the outlet temperature over the diameter is monitored.

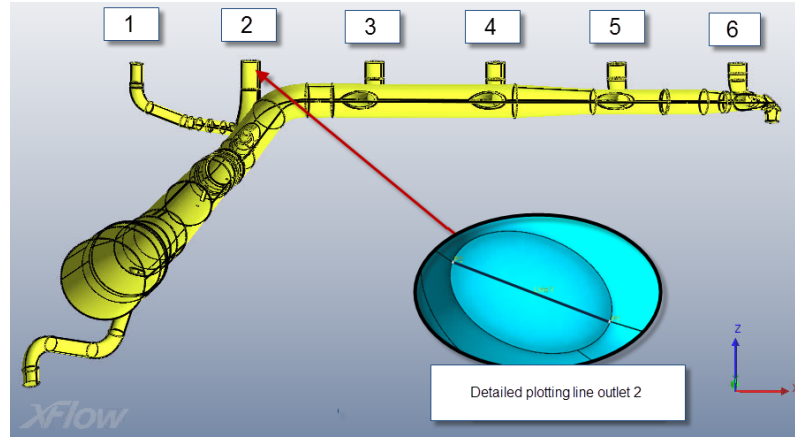


Figure 4.43: Overview of TZ3 with detailed plotting line of outlet 2.

The simulations show that there is a problem with non-uniform temperature distributions in the riser ducts. Evaluation of the outlet temperatures brings up that there is a hot stream which is mainly exhausted through outlets 1 & 2. This leads

to huge temperature differences of approximately 15 K between outlet 1 and outlet 6 at a trim flow of 40 g/s. In Figure 4.44 the average outlet temperatures are plotted over the diameter. Theoretically, the resulting mixing temperature at the given mass flow is 294 K.

The hot stream which can be monitored in Figure 4.46 leads to increased sensor indicated temperature. Analysis of probes located at the sensor results in an average indicated temperature of 317 K, which is approximately 27 K more than the overall, average temperature of all outlets and 23 K above the theoretical temperature. In this case the temperature sensor indicates too high temperatures which will lead to low resulting temperatures, especially in outlets 3 to 6.

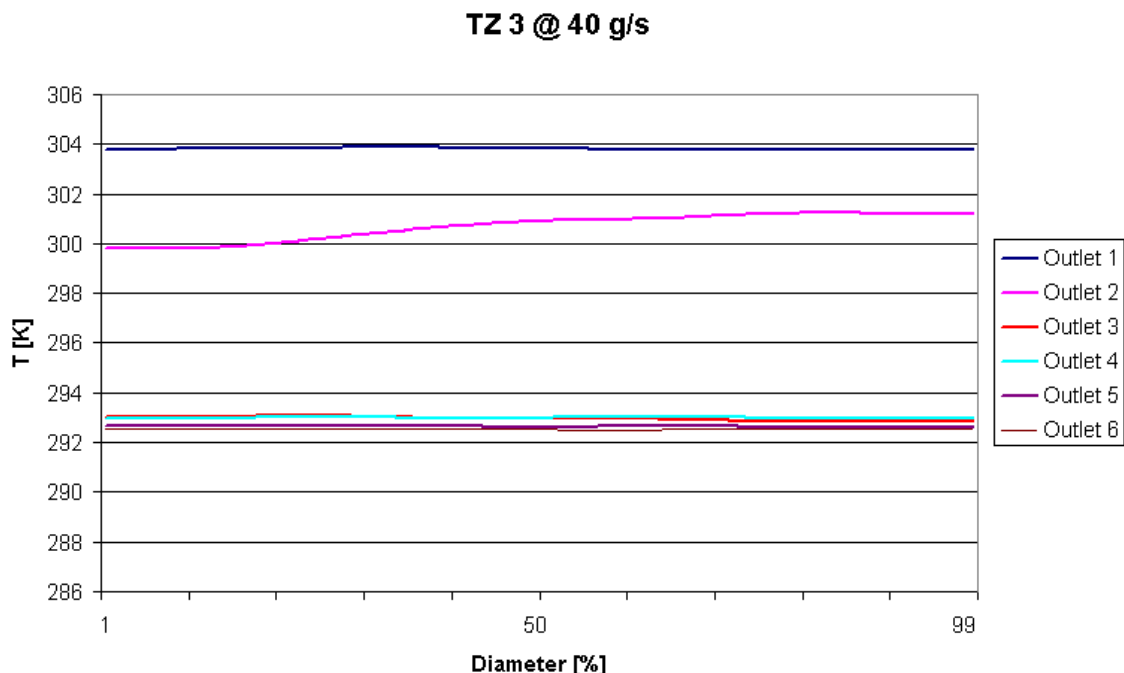


Figure 4.44: Average outlet temperatures for TZ4 at a trim flow of 40 g/s. The outlet temperature decreases for rising ducts that are located further downstream. The theoretical mixing temperature is calculated to 294 K.

The cause for the increased temperature at outlets 1 & 2 can be monitored in Figure 4.45. At this point it is necessary to dislocate the outlets or to install additional mixing devices.

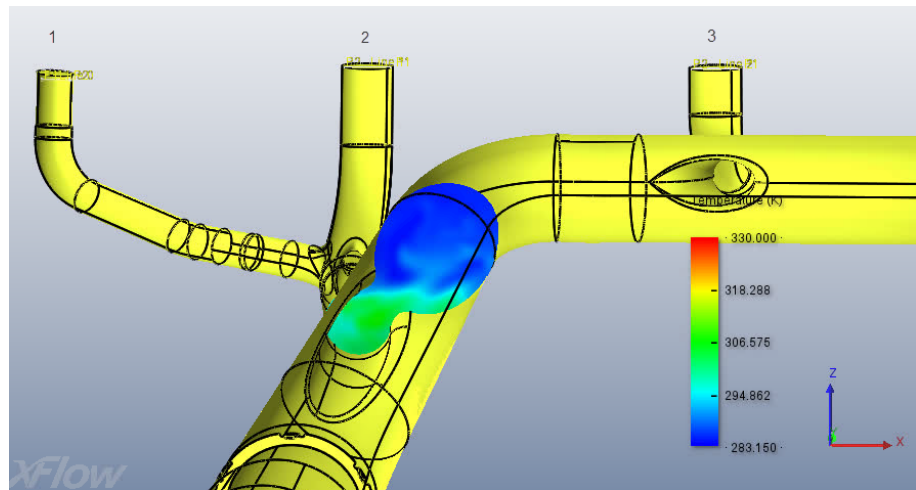


Figure 4.45: The hot stream directly enters the first branch for rising ducts 1 and 2.

Also the sensor temperature which is measured to an average value of 303 K is too high, resulting from the hot stream which surrounds the sensor (depicted in Figure 4.46).

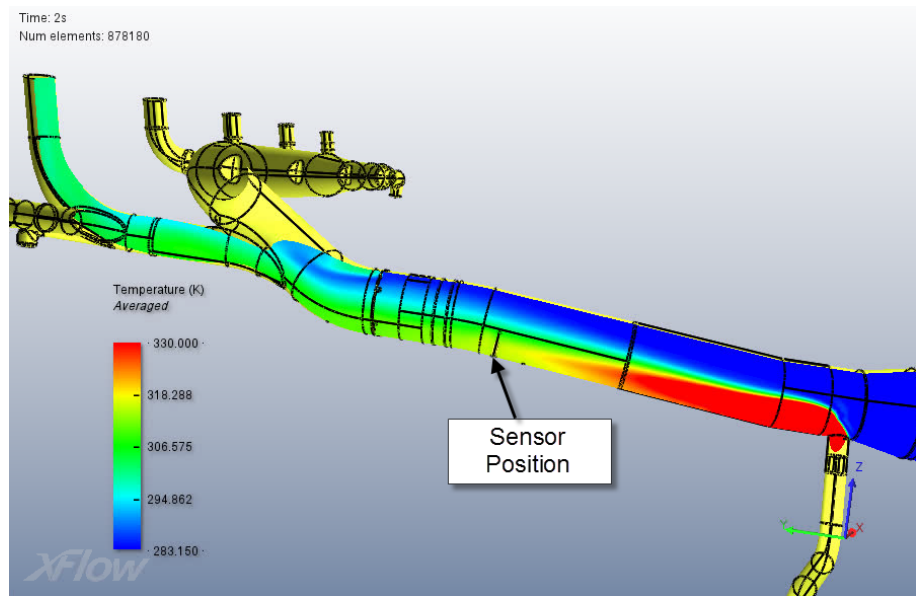


Figure 4.46: A hot stream which is not mixed with cool air develops downstream the intersection and negatively effects the temperature indicated by the sensor.

Finally, the wall temperature (shown in Figure 4.47 for this case depicts the further evolution of the temperature also downstream the branches for rising ducts 1 & 2.

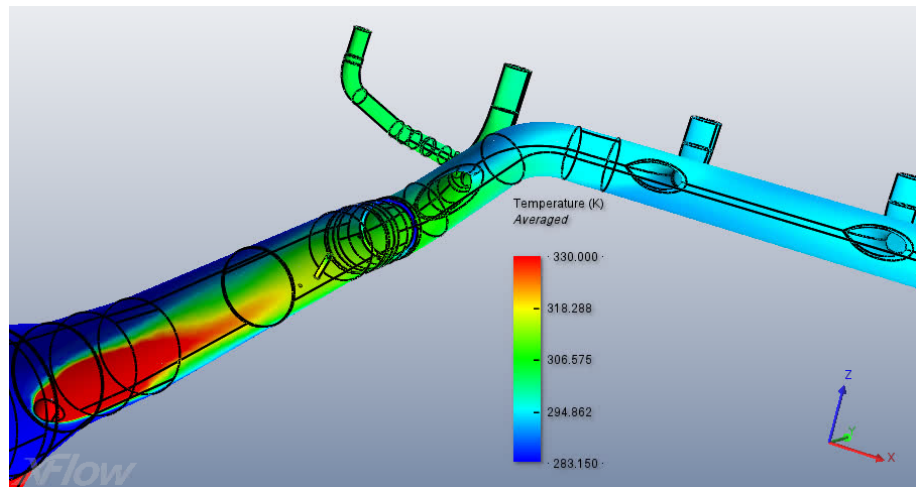


Figure 4.47: The wall temperature indicates uniform, mixed temperatures downstream the outlets 1 & 2.

10 g/s trim flow

In the case of the low trim flow, this zone seems to be as critical as in case for the high trim flow. The branch for outlets 1 & 2 is located improper and too close to the trim tapping.

The average sensor temperature results in 288 K which is approximately 2 K above the theoretical mixing temperature, calculated to 286 K. This seems to be an acceptable deviation but again, the temperature of the first two outlets is not acceptable. Figure 4.48 shows the average outlet temperatures. From this figure a maximum average deviation of 9 K can be derived between outlets 1 & 6.

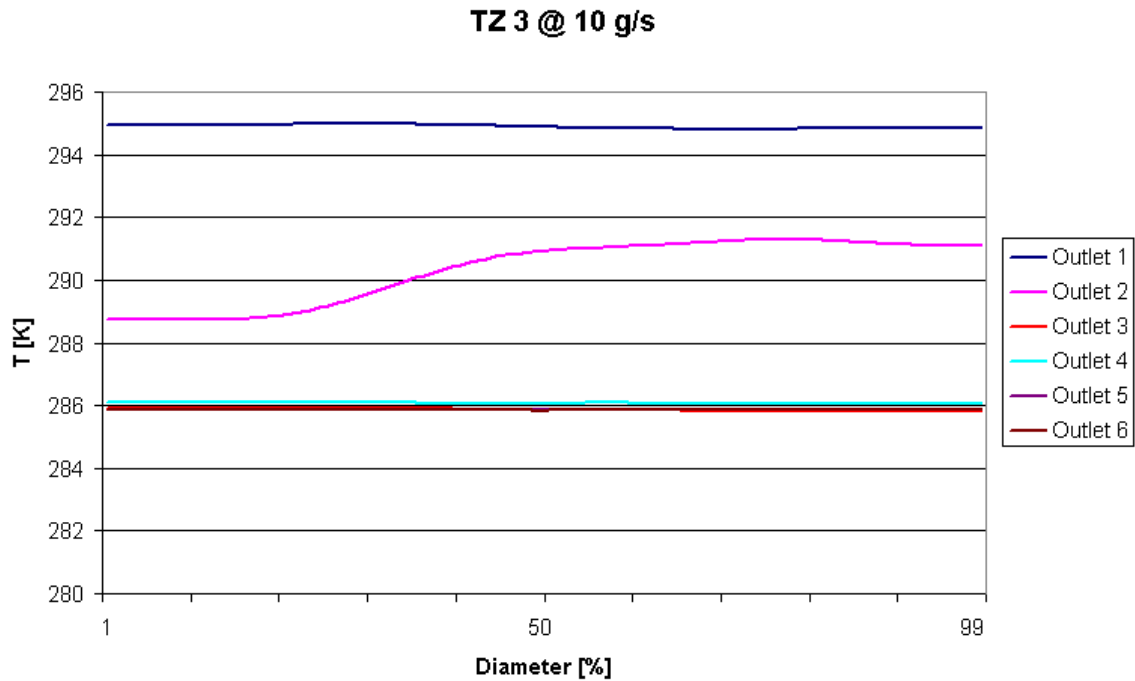


Figure 4.48: The hot stream which is exhausted through outlets 1 & 2 leads to 9 K difference between the average temperatures of outlet 1 and outlet 6. The theoretical mixing temperature is 286 K. Outlets 4-6 exhaust totally mixed air at theoretical mixing temperature.

The hot mass flow at 10 g/s is reduced but there is still a big portion of hot air exhausted through the first branch. Figure 4.49 shows a temperature profile, similar to the high trim flow, at the cross section of the first branch to outlets 1 & 2.

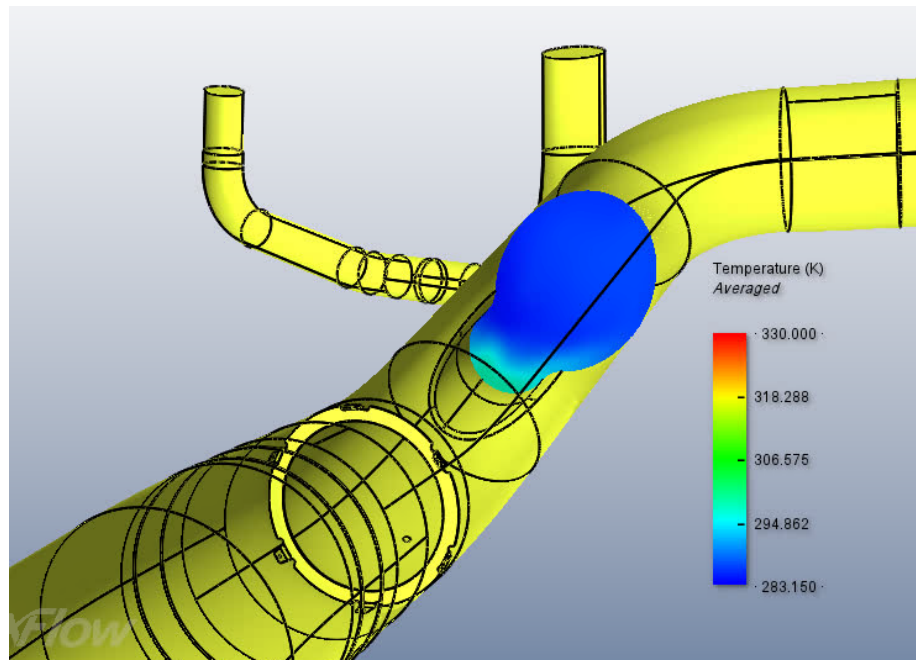


Figure 4.49: Similar to the high trim flow, the temperature profile of TZ 3 leads to increased outlet temperatures at riser ducts 1 & 2 also for the low trim flow.

Due to the low inlet velocity at the trim inlet, the hot air remains attached to the bottom wall of the main pipe as one can monitor in Figure 4.50. Because the tapping for outlets 1 & 2 is located at the bottom of the main pipe, big portions of hot air are led through these outlets.

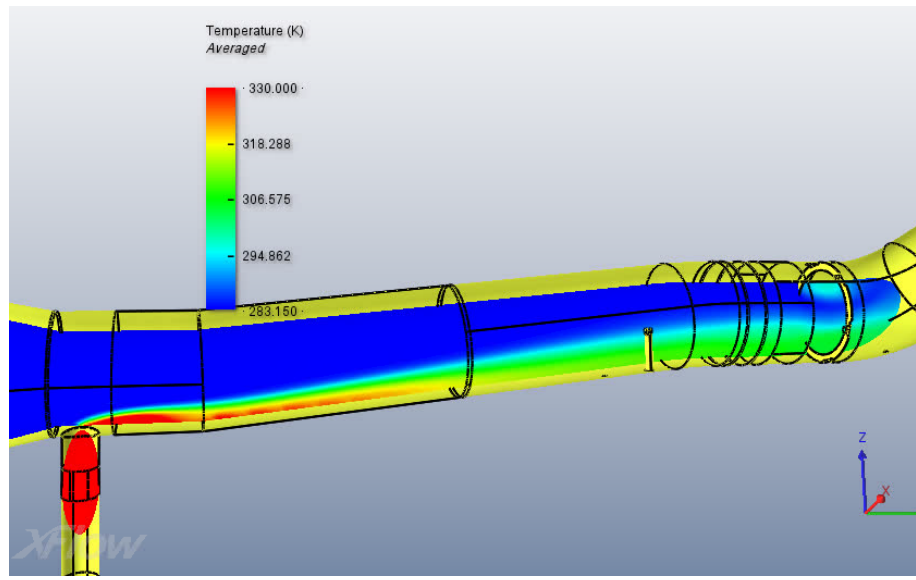


Figure 4.50: The trim flow remains attached to the bottom wall of the main pipe for low trim inlet velocities.

4.4 TZ 4

TZ 4 is the second critical zone due the close position of the riser ducts to the trim tapping. This zone is simulated until the beginning of the riser ducts to investigate the temperatures of all ducts individually.

40 g/s trim flow

The geometry for TZ 4 is more harmless due to a different location of riser ducts 1 & 2 downstream the bending of the main duct. Despite, there is a mean difference of 5 K between outlet 1 and outlet 5 which tells that there is still too much hot air leaving the main duct via outlet 1.

Figure 4.51 shows the average wall temperature downstream the trim tapping. Visually, a slight over-temperature can be monitored in the upper area of the main-pipe-bending in Figure 4.51 which causes the high outlet temperature in the first outlet.

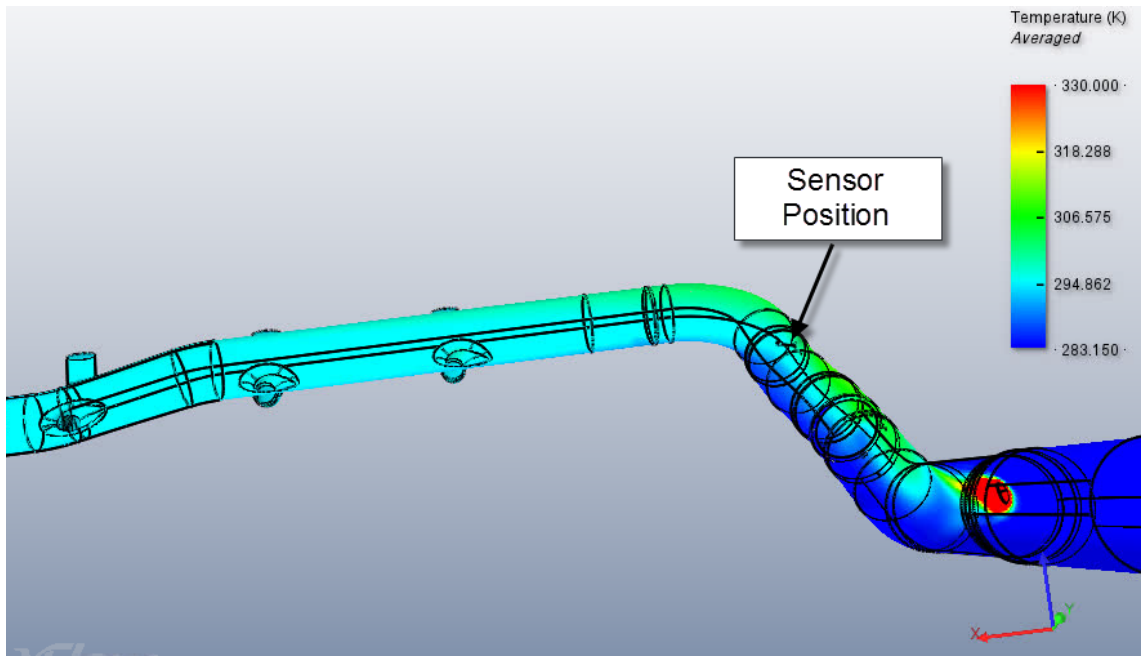


Figure 4.51: Average wall temperature of TZ 4 at high trim flow.

The following Figure 4.52 supports this assumption as it shows the temperature distribution of the outlets. The first two outlets are only slightly above the theoretical mixing temperature of 294 K but surprisingly, the last outlet is 5 K below this temperature.

Finally, Figure 4.53 shows why the measured, average sensor temperature of 296 K is 3 K above the overall average outlet temperature of 293 K, as the sensor slightly reaches into the hot air-stream.

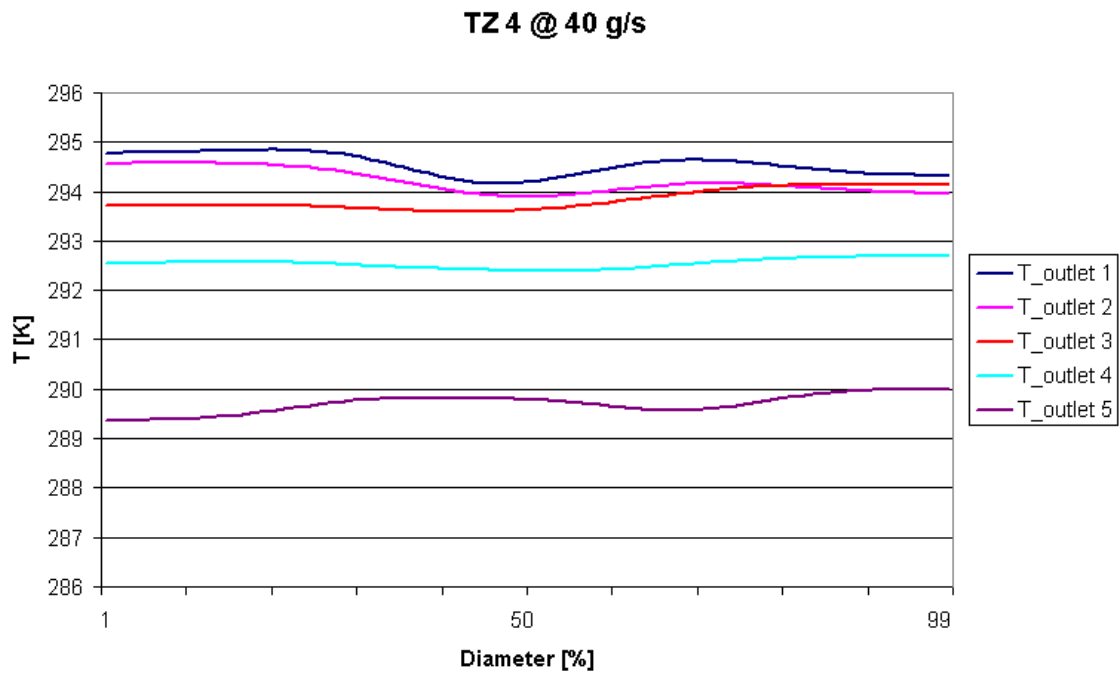


Figure 4.52: Average temperature of all outlets over the diameter. The mean average temperature in outlet 1 is 5 K above the temperature of outlet 5. The theoretical mixing temperature is approximately 294 K.

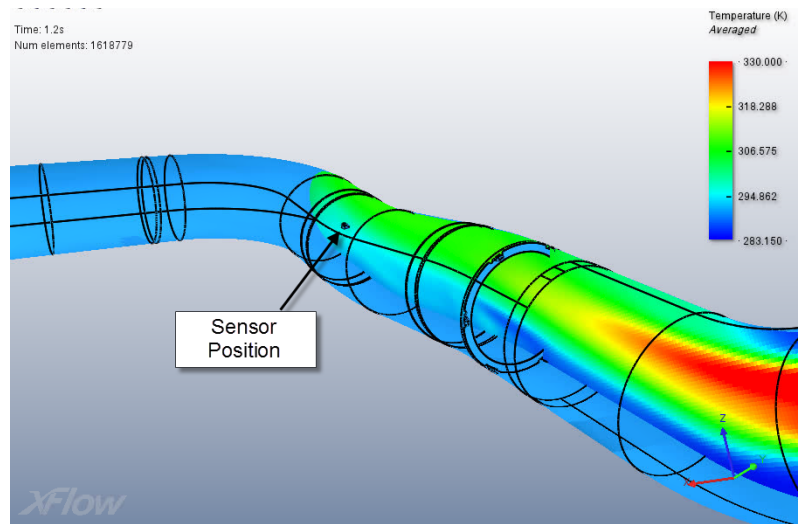


Figure 4.53: A longitudinal cross section of the average temperature profile in the sensor plane.

10 g/s trim flow

For the low trim flow the different measurements seem to be consistent all over. The temperature between the outlets varies only for 1 K between the maximum and the minimum average temperature and also the indicated sensor temperature of 287 K complies with the theoretical temperature and outlet temperatures. This is depicted in Figure 4.54 where the temperature profiles of all outlets are shown.

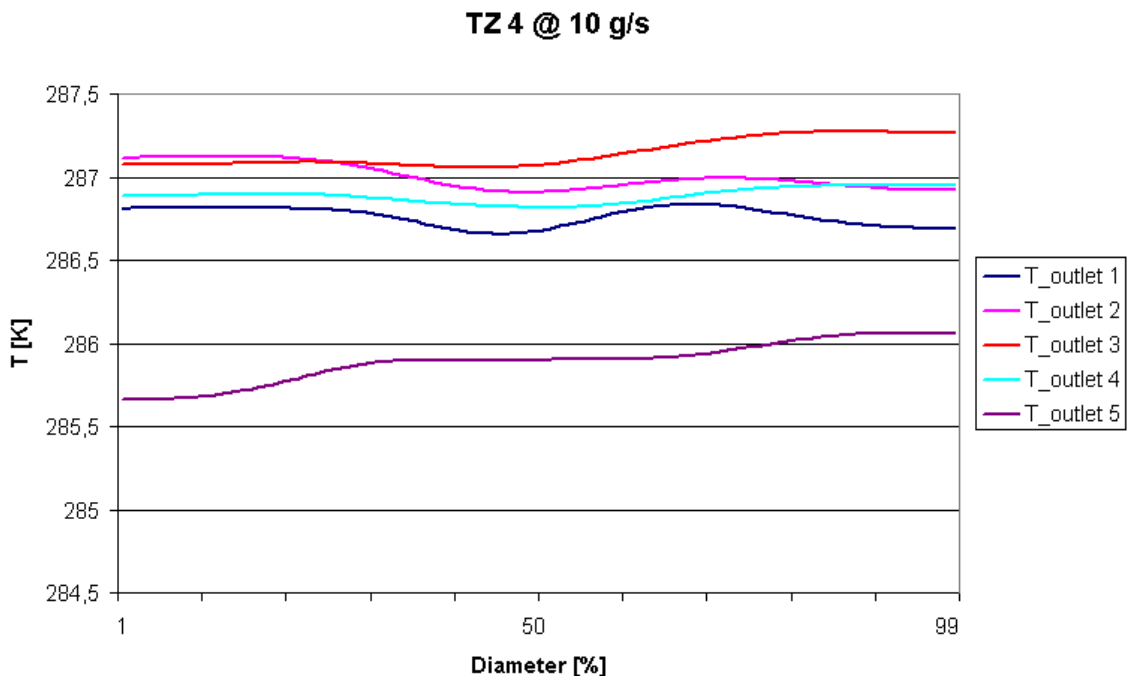


Figure 4.54: Average temperature of all outlets over the diameter. All outlet temperatures vary only slightly around the theoretical mixing temperature of 286 K.

4.5 TZ 5

TZ 5 is the zone which has the biggest main flow. In simulations the flow was set to 703 l/s. Despite the high main flow, the trim flow is kept constant at 40 and 10 g/s for high and low trim flow, respectively. For both cases the sensor seems to be located improperly as there are big deviations of the sensor temperature from the mixing temperature.

40 g/s trim flow

The temperature profile around the sensor, which is depicted in Figure 4.55, lets assume that the sensor is surrounded mainly by hot air. Evaluation of the temperatures at the usual positions affirms these assumptions.

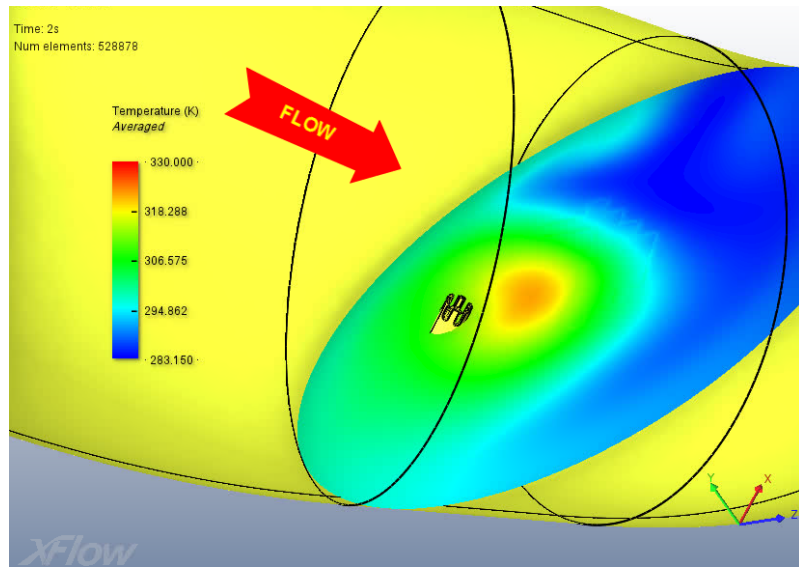


Figure 4.55: A hot stream of air surrounds the sensor of TZ 5 and leads to high sensor indicated temperatures.

For a high trim flow of 40 g/s there is a theoretical mixing temperature of 292 K. The temperature around the sensor is measured to 315 K which exceeds this temperature for 23 K in average. The outlet temperature at the plotting line reaches 294 K.

At the outlet the temperature profile is still strongly non-uniform with deviations of 15 K between hot and cold regions (see Figure 4.56).

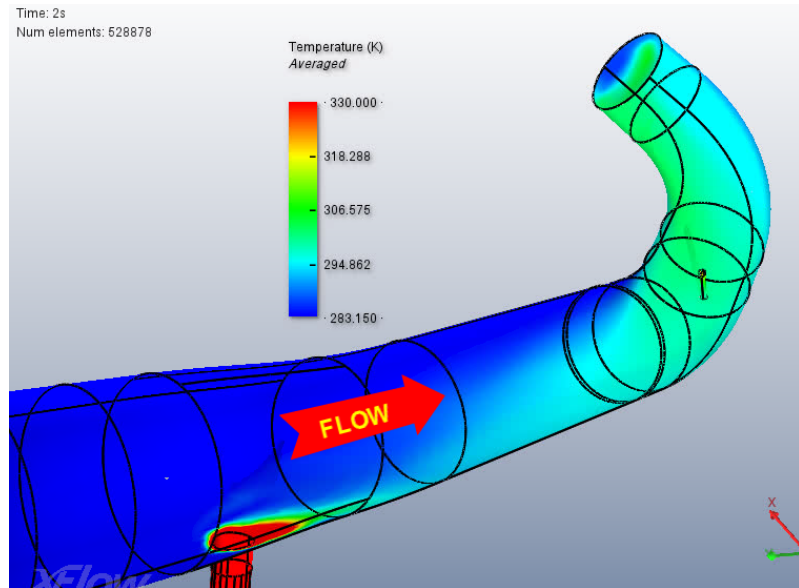


Figure 4.56: There is a hot stream which reaches until the outlet and leads to strongly non-uniform outlet temperature.

According to this results, the sensor position has to be adapted. Also for the low trim flow, the sensor indicates too high temperatures.

10 g/s trim flow

The flow develops similar to the high trim flow. There is a hot stream which directly hits the sensor. Figure 4.57 depicts the average wall temperature and the temperature profile at the sensor cross section to get an idea of the extent of the hot stream.

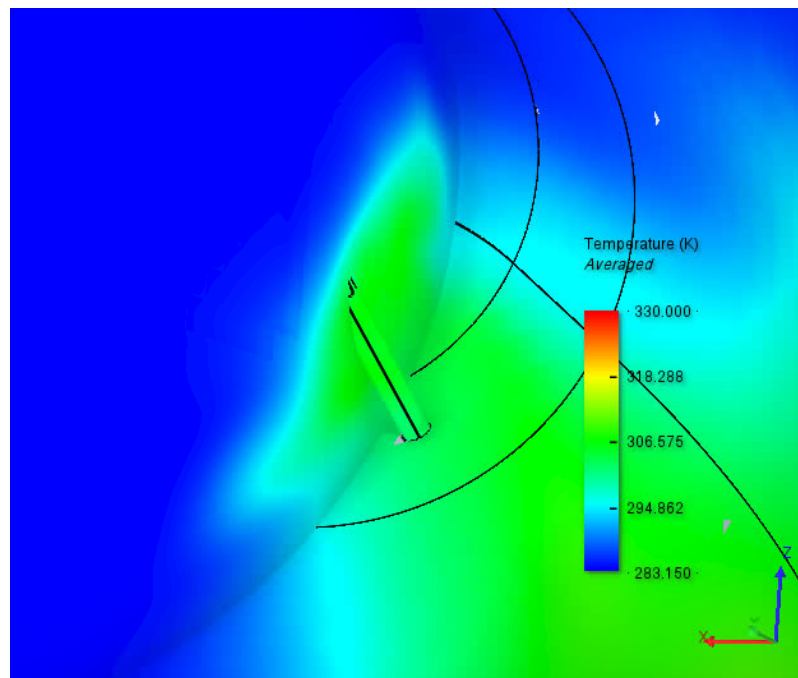


Figure 4.57: Average wall temperature and temperature at the sensor cross section for TZ 5.

There is a theoretical mixing temperature of 286 K and measured temperatures of 300 K at the sensor and 288 K at the outlet. Again, a big error of almost 15 K between actual and ideal sensor temperature.

4.6 TZ 6

TZ 6 is simulated at standard resolution of 0.01 m with refinement of 0.005 m near walls. The results for high and low trim flows appear as follows.

40 g/s trim flow

The average resulting temperature of 298 K at the outlet drastically differs from the theoretical mixing temperature of 292 K. The temperature profile at the outlet

is still non-uniform, meaning that mixing is not completed yet at this station. The difference of 6 K in the mixing temperatures could be described by taking into account, that at the outlet, areas with low temperatures have higher velocities / higher mass flows than areas with higher temperatures. This gives the lower temperatures more weight which may lead to proper mixing temperatures in the end.

Figure 4.58 shows the wall temperature with an additional cutting plane in the sensor cross section.

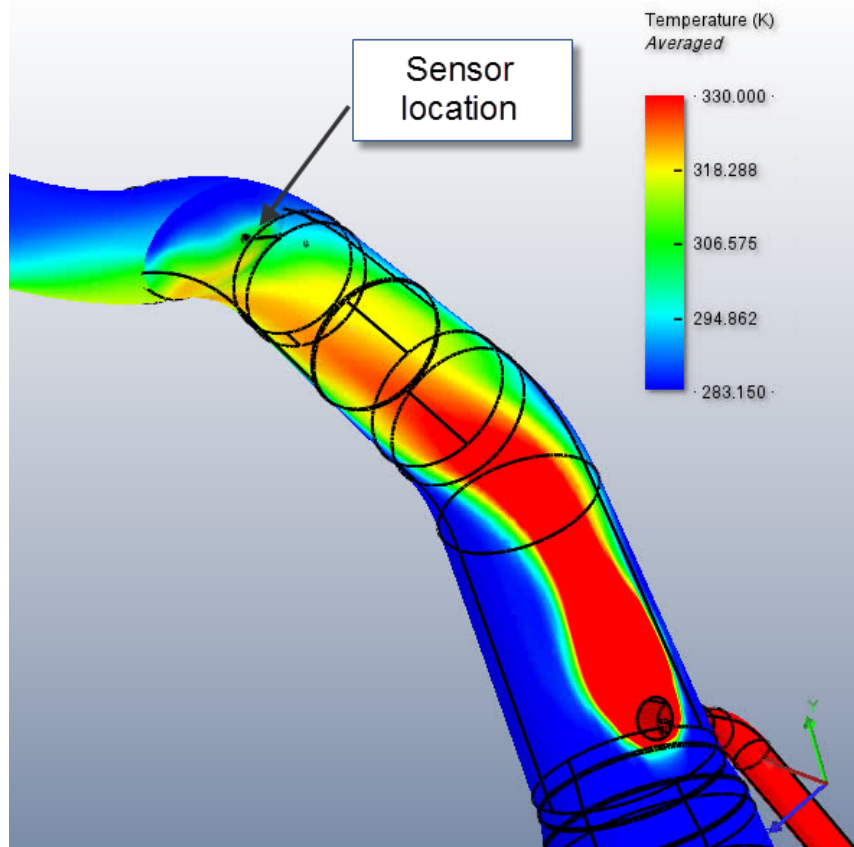


Figure 4.58: Wall temperature for TZ 6 and high trim flow.

The average sensor temperature is measured to 300 K which is less than 2 K below the average outlet temperature of 298 K but 8 K above the theoretical mixing temperature.

For this zone, in Figure 4.59, also the temporal evolution of the sensor temperature is depicted. All zones show similar fluctuations of the sensor temperature but inertia of the system should automatically smooth this curve.

Finally, Figure 4.60 depicts the non-uniform temperature field at the outlet.

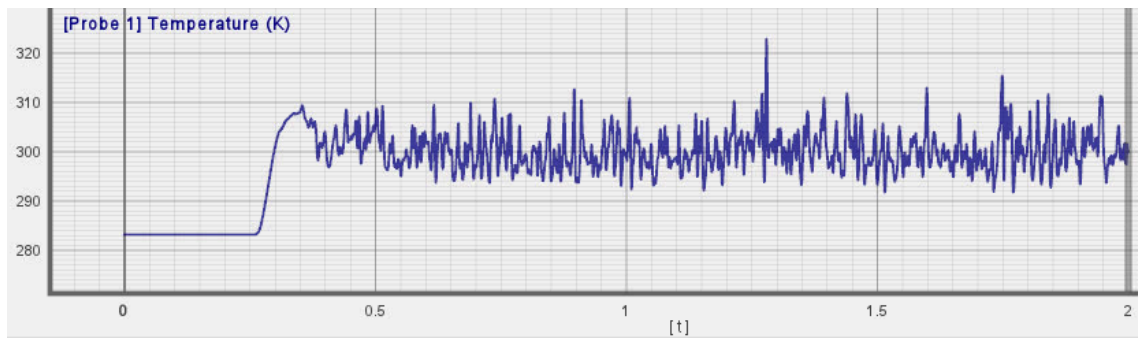


Figure 4.59: The temperature of the probe which is located at the sensor is strongly fluctuating over the time of 2 s.

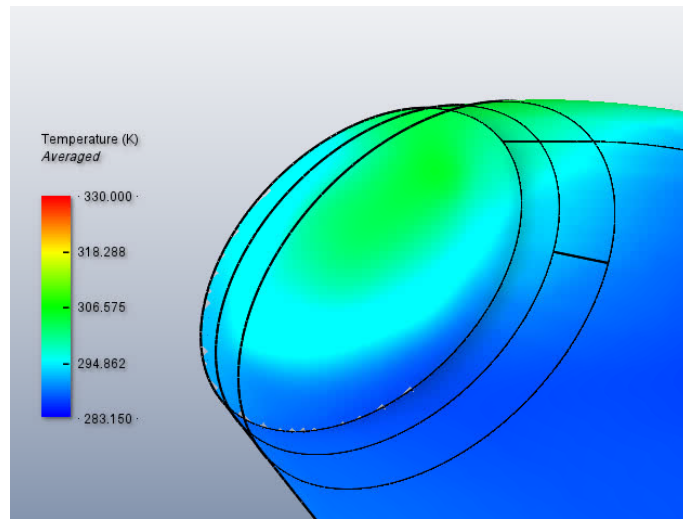


Figure 4.60: Outlet temperature for TZ 6 and high trim flow. The theoretical mixing temperature is calculated to 292 K.

10 g/s trim flow

Also in case of the low trim flow, the outlet temperature profile is strongly non-uniform which may describe the differences between the actual and theoretical mixing temperatures. But it is not seen as a problem because the real cabin outlet is still far away from the outlet of this simulation which was chosen in order to reduce the computational effort.

The average temperature of the plotting line at the outlet is 289 K, compared to the theoretical temperature of 285 K. Again, it can be monitored that areas with low temperatures have a higher mass flow, giving them more weight on the average temperature. This fact is not considered by averaging over plotting lines which, for non-uniform temperature profiles, leads to errors when calculating the mixing temperatures.

The wall temperature, shown in Figure 4.61 appears to be similar to the high trim flow case.

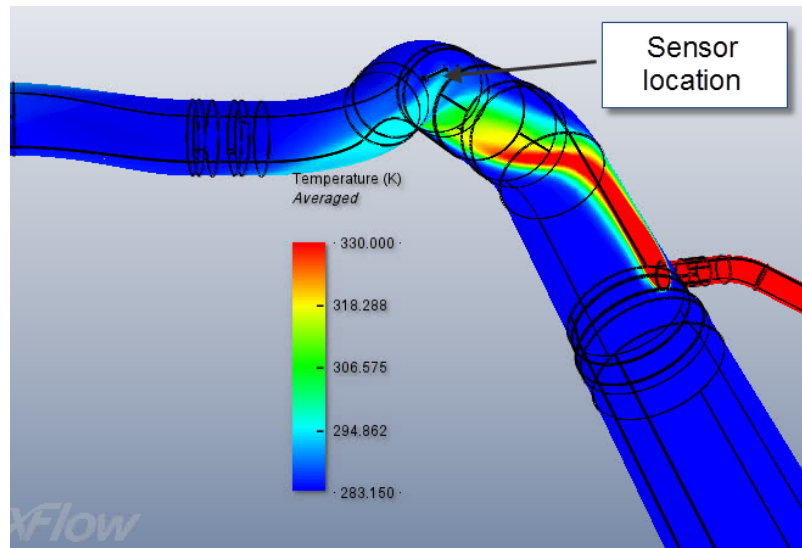


Figure 4.61: Wall temperature for the low trim flow of TZ 6.

4.7 TZ 7

The geometry of this zone is cut immediately downstream the temperature sensor. This is why the mixing distance until the outlet is rather short and the temperature profile is non-uniform at the outlet. Nevertheless, this does not influence the sensor temperature, which is the actual important value.

40 g/s trim flow

At a trim flow of 40 g/s, there is a theoretical mixing temperature of 293 K. Figure 4.62 shows, that the sensor penetrates the hot stream but does not directly hit the hot core. Nevertheless, the sensor temperature of 307 K is 14 K above the ideal temperature.

The average outlet temperature can be monitored to 295 K, but is not really of interest here, because only nearly uniform temperatures would deliver appropriate average mixing temperatures. Otherwise, it would be necessary to also consider the velocity profile at the outlet in order to achieve correct values.

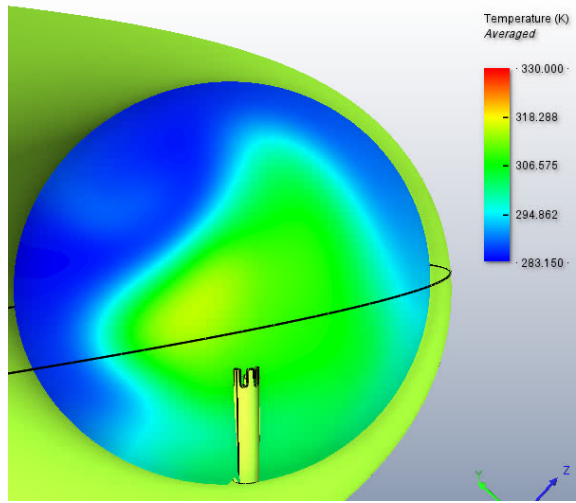


Figure 4.62: Temperature cross section at the sensor of TZ 7.

Figure 4.63 shows the evolution of the hot stream and also the temperature profile at the outlet can be seen.

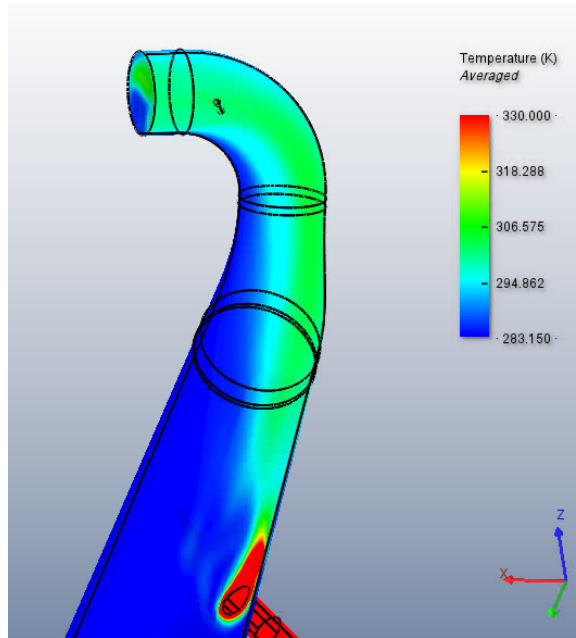


Figure 4.63: Wall temperature for the high trim flow of TZ 7.

10 g/s trim flow

Compared to the high trim flow it is interesting to monitor the wall temperature of the low trim flow in Figure 4.64. In this case, downstream the intersection, the hot stream remains attached, leading to high wall temperatures, whereas for a trim

flow of 40 g/s, the hot stream separates and the hot area at the wall downstream is smaller.

Further, this indicates that for higher trim flows the mixing efficiency is better than for low trim flows. The reason is a higher velocity at the trim pipe for high trim flows which has the effect that the hot air penetrates the main flow.

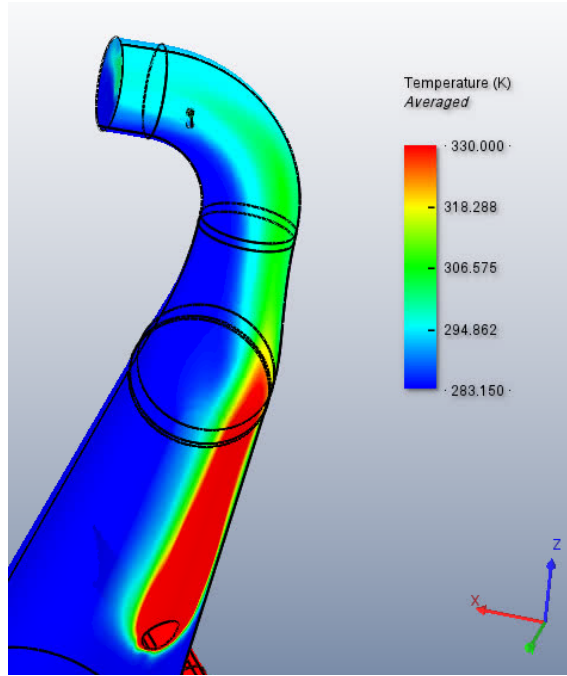


Figure 4.64: Wall temperature for the low trim flow of TZ 7.

The sensor temperature differs even more from the ideal temperature of 285 K in this case. At the sensor a temperature of 303 K can be monitored which results in an average deviation of 18 K.

4.8 Flight Crew Rest Compartment (FCRC)

For the FCRC a reduced trim flow is chosen because of the reduced main flow of only 50 l/s. The small main-pipe-diameter seems to have positive impact on thermal mixing.

10 g/s trim flow

Even though the mixing distance is very low, the temperature profile at the sensor cross section is nearly uniform as Figure 4.65 shows.

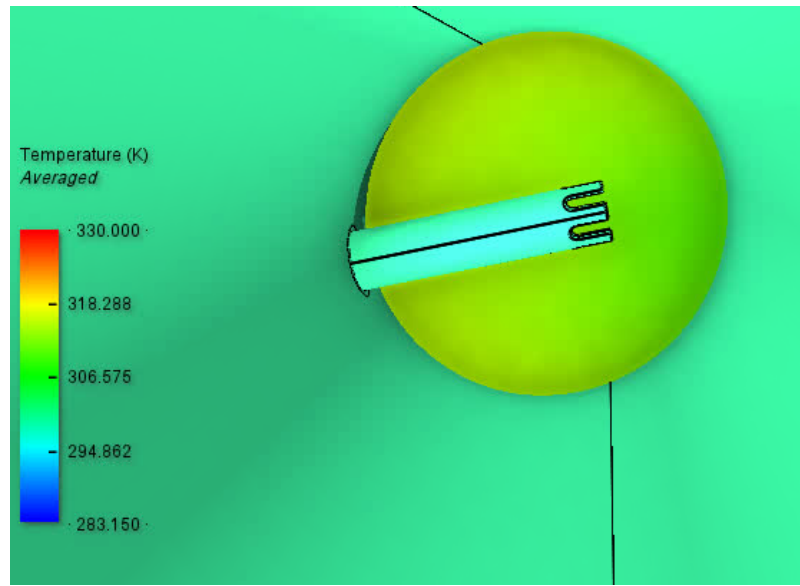


Figure 4.65: Temperature profile at the cross section of the temperature sensor.

Evaluation and comparison of sensor temperatures gives proof to that. The average sensor temperature is measured to 313 K whereas the average outlet temperature can be monitored to 314 K. The theoretical mixing temperature is 311 K.

The reason for proper thermal mixing is that the hot trim flow penetrates the main flow as the cross section in Figure 4.66 depicts.

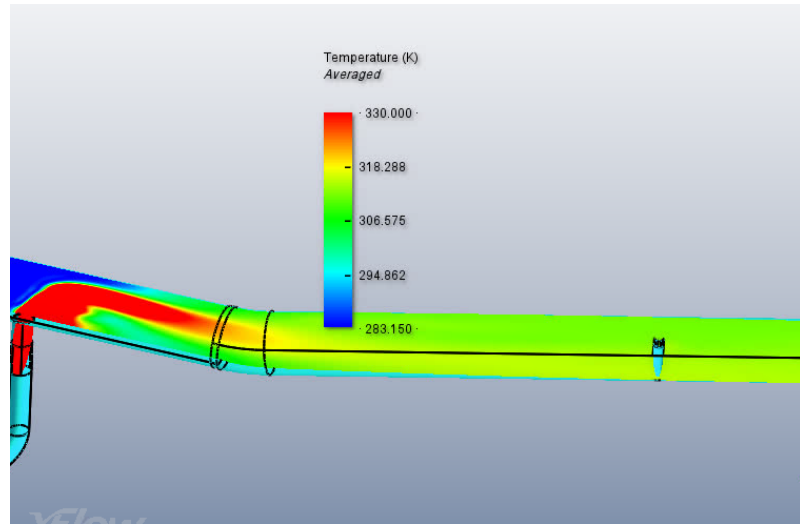


Figure 4.66: Temperature profile at the longitudinal cross section of the FCRC.

5 g/s trim flow

For the low trim flow the mixing efficiency decreases because the inlet velocity for the trim inlet decreases which has the result that the hot flow remains attached to

the bottom wall of Figure 4.67.

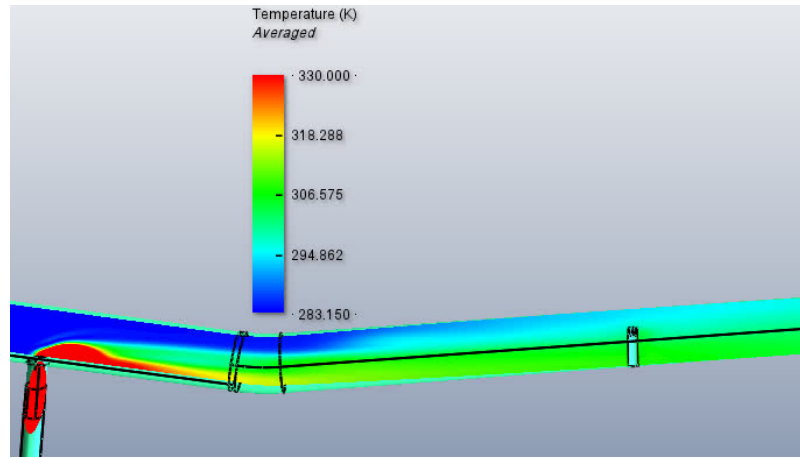


Figure 4.67: The low trim flow results in a different temperature profile at the cross section of the temperature sensor as the hot flow remains attached to the wall.

Luckily, the temperature of the sensor is still in good coincidence with the outlet and the theoretical temperatures. The resulting sensor temperature is 298 K whereas the outlet temperature is 301 K. Theoretically, the resulting temperature should be 298 K. Only little deviations seem appear in this case although the sensor cross section in Figure 4.66 shows a layered temperature profile.

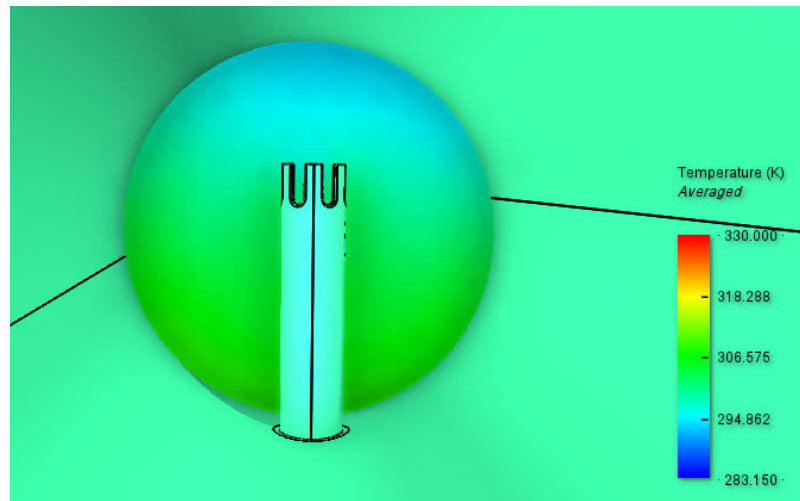


Figure 4.68: There is at least 5 K difference between the top and bottom wall temperature in the sensor cross section.

4.9 Cabin Crew Rest Compartment (CCRC)

40 g/s trim flow

For a high trim flow, within this zone, the temperature sensor is surrounded by a temperature of 303 K. The ideal mixing temperature is calculated to 296 K which results in a deviation of 7 K.

Figure 4.69 shows the average wall temperature field. This zone is a good example for the density related buoyancy mixing. In Figure 4.69 one can see that downstream the bending the wall temperature appears to be uniform at mixing temperature. This positive effect is caused because the trim tapping is located on the outer side of the bending of the main pipe.

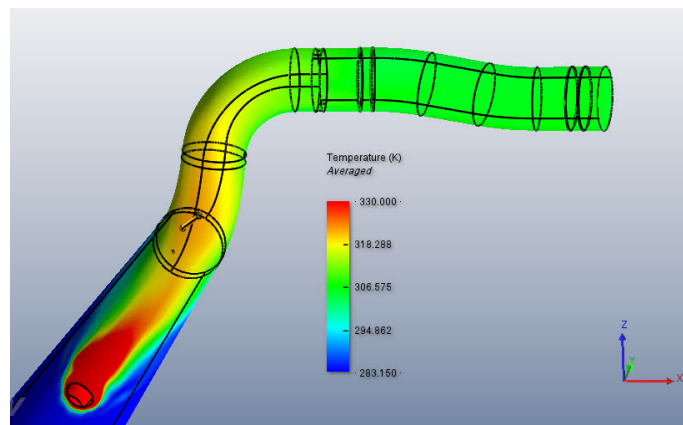


Figure 4.69: Average wall temperature for high trim flow in CCRC.

At the sensor cross section the temperature profile is depicted in detail within Figure 4.70. The air is not yet mixed at this station. Shifting the sensor position downstream the bending would definitely have positive impact on the measured sensor temperature.

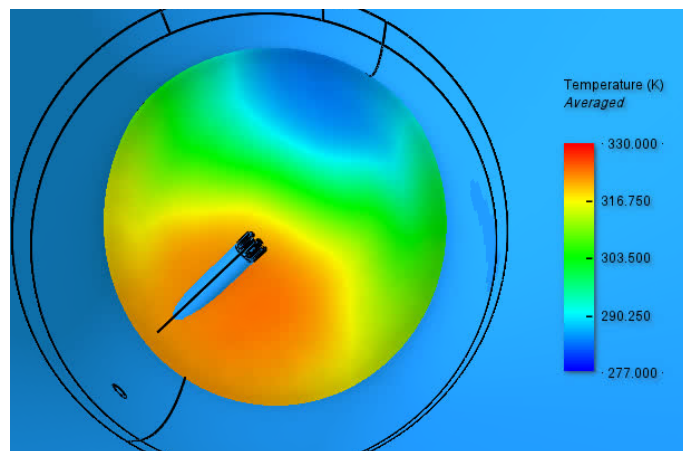


Figure 4.70: Average temperature at the sensor cross section.

10 g/s trim flow

The temperature profile at the sensor cross section in Figure 4.71 shows that there is a small, hot stream which directly hits the sensor and leads to increased sensor temperature. The deviation which appears in this case is the biggest deviation of all cases. The theoretical mixing temperature is 287 K whereas the average sensor temperature is measured to 312 K, resulting in a huge difference of 25 K. The average outlet temperature of 291 K is only 4 K above the theoretical mixing temperature.

According to this results an additional mixing device is necessary within this zone. Else, relocation of the sensor downstream the bending of the main pipe might also improve the sensor temperature with respect to the theoretical mixing temperature.

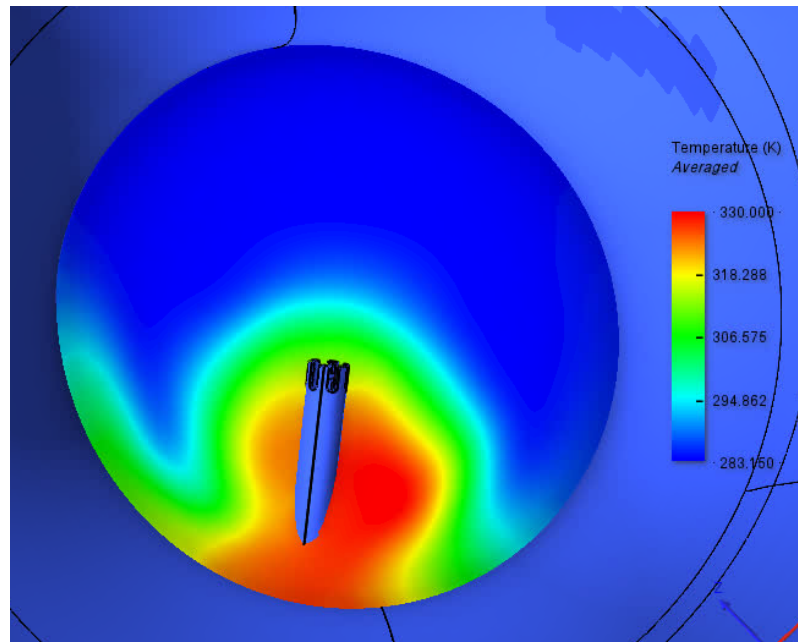


Figure 4.71: The low trim flow hits the sensor of the CCRC.

4.10 Flight Deck (F/D)

This is the last zone which is investigated. Due to a lower main mass flow the trim flow is slightly decreased in order to simulate realistic conditions.

15 g/s trim flow

At a trim flow of 15 g/s a resulting temperature of 302 K should arise. Although the hot stream gets very close to the sensor (as Figure 4.72 shows) the sensor temperature still is measured to 296 K which is 6 K too low. But it is unknown how the temperature field develops for higher trim flows. Maybe then the sensor gets directly hit by hot trim air and reports much too high temperatures. This should be considered for further research.

Surprisingly, the outlet temperature is measured at an average temperature of 308 K which is much higher than the theoretical and the sensor temperature. This time the temperature profile is quite uniform and it is unclear why there is a higher temperature at the outlet. In some other cases this deviation could be explained through different mass flows of hot and cold regions at the outlet but here this is not the case.

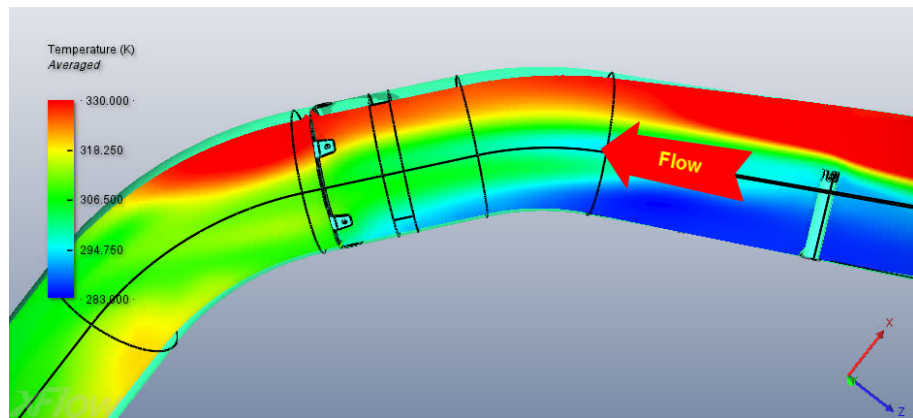


Figure 4.72: The hot stream is close to the sensor of the F/D.

10 g/s trim flow

The hot stream is developed smaller than for 15 g/s and the sensor indicates a temperature of 289 K which is 4 K below the theoretical mixing temperature of 293 K. Figure 4.73 depicts the average wall temperature. At the outlet hot and cool air is mixed very well but the average outlet temperature of 296 K is slightly too high.

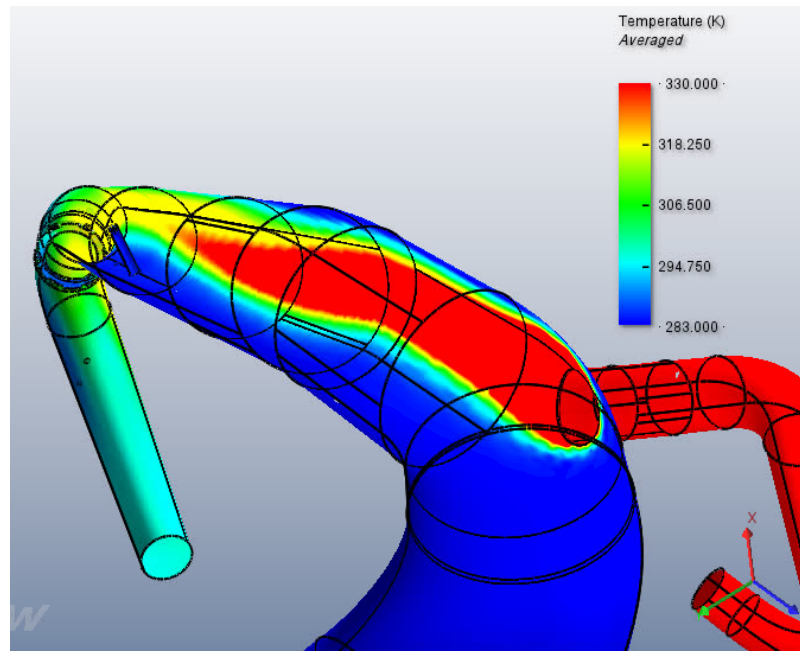


Figure 4.73: Average wall temperature for the F/D and 10 g/s.

4.11 Summary of Results

It is difficult to optimize the system based on only 2 simulations per zone because each simulation is no more than one point on a highly non-linear function depending on the main- and trim-flows. For slightly different conditions the flow field may appear totally different. Nevertheless, the results have shown that especially in TZ 3 there is a problem with the location of the outlet which is leading to riser ducts 1 & 2. For many other zones the simulations predict too high sensor temperatures which may need to be resolved by implementing additional mixing devices or shifting sensor locations.

In order to gain a better overview on the results, Tables 5 and 6 summarize the important temperatures for the different zones for high and low trim flows, respectively. The “sensor temperature deviation” depicts the deviation of the sensor temperature from the theoretical temperature and the value “max. delta-T outlets” depicts the temperature difference between the hottest and the coolest outlet if there is more than one outlet. For TZ 4 and for the high trim flow of the F/D one can find results of STAR-CCM+ for comparison. The results do not match with XFLOW but also STAR-CCM+ results show deviations in sensor temperatures. All values are in Kelvin.

Table 5: Summary of all cases with high trim flow.

| | Average outlet temperature | Average sensor temperature | Sensor temperature deviation | Theoretical temperature | Max. delta-T outlets |
|-------------------|----------------------------|----------------------------|------------------------------|-------------------------|----------------------|
| TZ 1 | 300.5 | 304.8 | 11.0 | 293.8 | - |
| TZ 2 | 303.9 | 308.4 | 13.4 | 295.0 | - |
| TZ 3 | 295.9 | 302.9 | -8.6 | 294.3 | 11.3 |
| TZ 4 | 293.0 | 296.4 | 2.3 | 294.1 | 4.8 |
| TZ 4 STAR-CCM+ | 291.9 | 290.1 | -4.0 | 294.1 | 1.0 |
| TZ 5 | 294.4 | 315.2 | 23.1 | 292.1 | - |
| TZ 6 | 298.4 | 300.2 | 7.3 | 292.9 | - |
| TZ 7 | 295.2 | 307.9 | 15.2 | 292.7 | - |
| FCRC | 313.5 | 312.6 | 1.6 | 311.0 | - |
| CCRC | 288.3 | 303.4 | 7.0 | 296.4 | - |
| F/D | 308.1 | 296.4 | -6.1 | 302.5 | - |
| F/D STAR-CCM+ | 300.9 | 315.3 | 12.7 | 302.5 | - |

Table 6: Summary of all cases with low trim flow.

| | Average outlet temperature | Average sensor temperature | Sensor temperature deviation | Theoretical temperature | Max. delta-T outlets |
|-------------------|----------------------------|----------------------------|------------------------------|-------------------------|----------------------|
| TZ 1 | 286.8 | 286.3 | 0.3 | 286.0 | - |
| TZ 2 | 292.4 | 289.8 | 3.4 | 286.4 | - |
| TZ 3 | 288.1 | 288.3 | 2.2 | 286.1 | 9.0 |
| TZ 4 | 286.7 | 287.0 | 1.0 | 286.0 | 1.3 |
| TZ 4 STAR-CCM+ | 285.2 | 283.4 | -2.6 | 286.0 | 2.3 |
| TZ 5 | 288.7 | 300.2 | 14.7 | 285.5 | - |
| TZ 6 | 289.3 | 287.7 | 2.0 | 285.7 | - |
| TZ 7 | 288.3 | 303.4 | 17.8 | 285.6 | - |
| FCRC | 300.7 | 297.7 | -0.6 | 298.3 | - |
| CCRC | 291.4 | 311.8 | 25.0 | 286.8 | - |
| F/D | 296.3 | 288.8 | -4.0 | 292.8 | - |

4.12 Mixing Devices

The results have shown that there is a need for additional thermal mixing for some zones. Because of that, some research on geometry and efficiency of mixing devices is done. As a result, the TZ 3 is simulated with 3 different mixing geometries, based on Figure 4.74. Unluckily, the author was only able to produce results for the depicted geometry. Other geometries with a different number of blades and different angles of attack produced unknown errors in XFLOW.

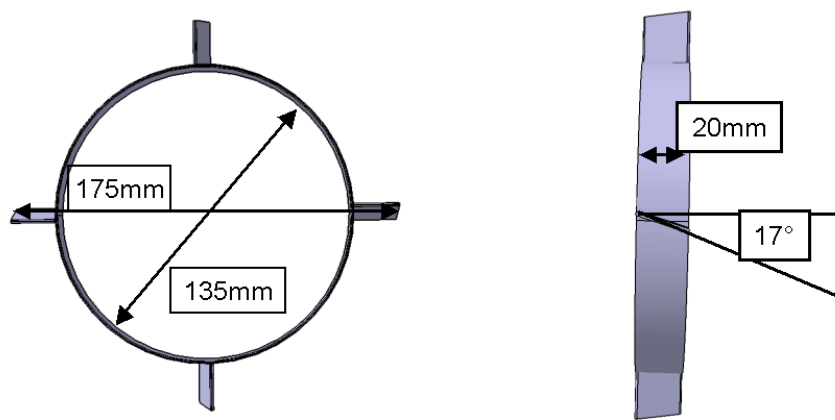


Figure 4.74: Dimensions of the simulated mixing device.

During the research a very promising device, called the Oxynator (©Air Liquide) was found. The author was not able to gather further information on this device until the end of the internship. Figure 4.75 depicts the working principle. This device is installed at the trim inlet and exhausts the trim air radially in the center of the main pipe. The producer promises highest mixing efficiency for low total pressure drop in the main pipe. The pressure drop in the trim pipe is not critical, as the trim air usually has enough over-pressure which needs to be relieved via a pressure-relief-valve.

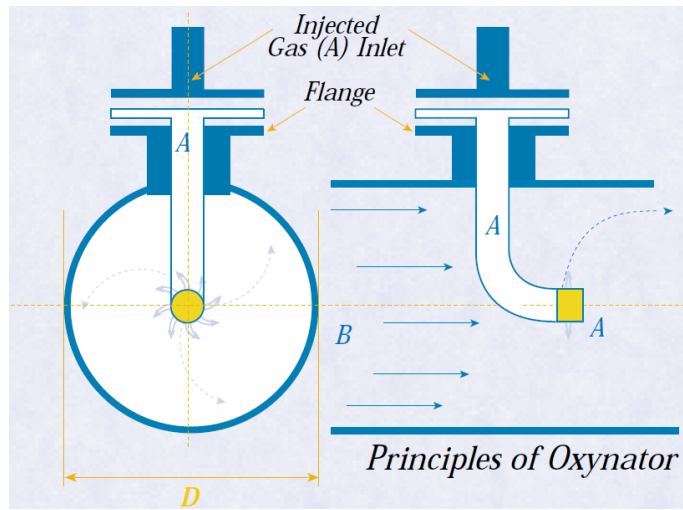


Figure 4.75: Working principle of the oxynator (Air Liquide).

4.12.1 TZ 3 with Mixing Device

TZ 3 is chosen for the simulation of the additional mixing device because of the problems in terms of thermal mixing that appear for the first riser ducts. The following Figure 4.76 shows the location and the geometrical setup of the mixing device within TZ 3.

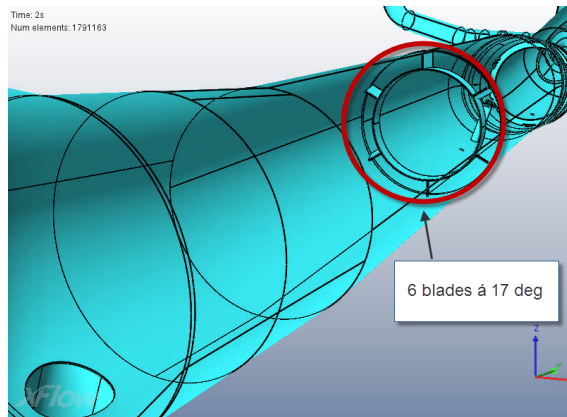


Figure 4.76: Additional mixing device within TZ 3.

The mixing device achieved its goal as the temperature profiles for the riser ducts show. The maximum difference between the coolest and the hottest outlet temperature is reduced to less than 2 K for the 6 bladed mixer. For 4 blades a maximum temperature difference of 3.5 K remains.

In the area around the sensor no realistic temperature could be monitored as all measurements varied around 580 K. This may again arise from numerical instabilities which can be seen in the temperature profile, depicted in Figure 4.78 and makes the results less trustable. Further, Figure 4.79 depicts the average outlet temperature

profiles for the riser ducts of TZ 3. Note that the average mixing temperature for a trim flow of 40 g/s is 294 K. It is unknown why the average outlet temperatures in Figure 4.79 are far below the average mixing temperature. Nevertheless, the temperature difference between the outlets is minimized.

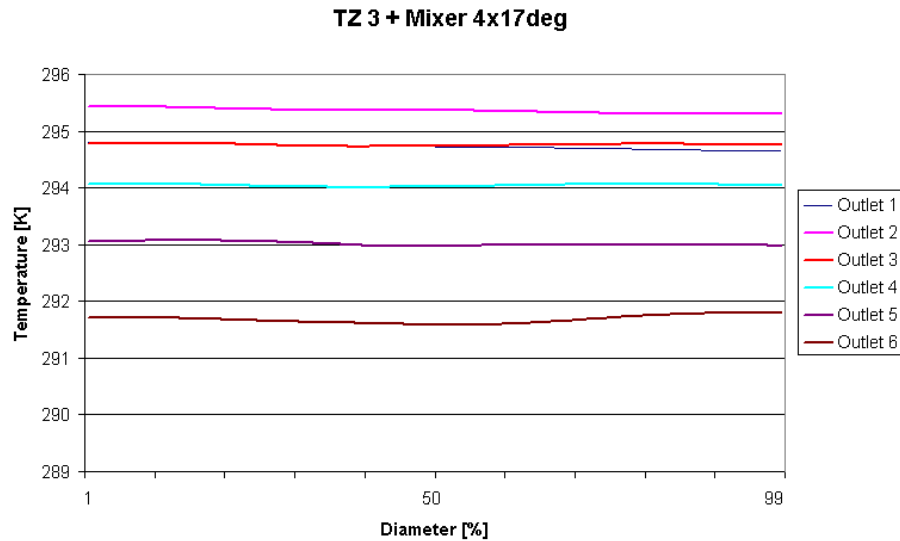


Figure 4.77: Average outlet temperature profiles for TZ 3 with 4 bladed mixer.

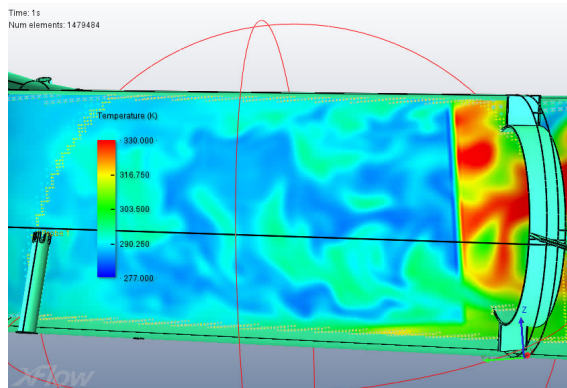


Figure 4.78: A non-physical temperature drop appears downstream the 4-bladed mixer also where the refinement region (red sphere) is located.

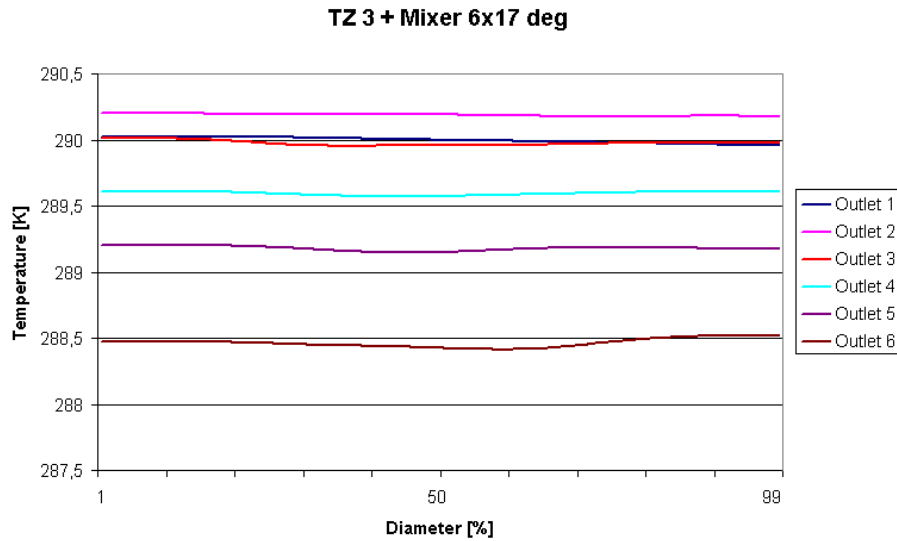


Figure 4.79: Average outlet temperature profiles for TZ 3 with 6 bladed mixer.

It is also necessary to evaluate the total pressure loss caused by the mixing device but in terms of thermal mixing. Unluckily, the immense pressure fluctuations did not allow to extract proper values for inlet and outlet pressures. Nevertheless, for this case, the main goal is achieved as the temperature difference is decreased from 11 K to less than 2 K.

4.13 Remark on Results

Towards the end of the internship it turned out that the pressure fluctuations are caused by the non-equilibrium enhanced wall-function which was chosen based on the results of the test cases earlier. As a result of those test cases, the non-equilibrium enhanced wall-function turned out to be most suitable for thermal mixing of incompressible fluids. For compressible fluids it caused the pressure fluctuations as they were depicted previously.

There was no opportunity to recompute and to reprocess all 20 cases within 2 days. As a compromise the author decided to recompute TZ 3, TZ 4 and F/D. Unluckily, the temperature field for the following results will vary from previous results (especially for F/D). Because of that, all previous results have to be considered rather critical.

The change in the simulation setup caused different densities at the inlet for TZ 4. Because of the problem with the temperature that gets stuck at the inlet when choosing mass flow boundary conditions (depicted earlier in Figure 4.35), the mass flow could not be set properly. For the new results of TZ 4 a higher mass flow of 60 g/s resulted for the same velocity boundary condition. So the results are not to be compared directly to the previous results due to different trim flows. Further, for re-computation a rough resolution of 0.01 m was chosen to gather the results quickly.

This means that the deviation from the previous results could also be caused by the coarse resolution. Therefore the F/D was also recomputed with the previous settings which caused pressure fluctuations but on a uniform resolution of 0.01 m. The result for the F/D will show that the resolution has a big influence as well.

TZ 3 @ 40 g/s

As expected, the previous results may be wrong quantitatively but they qualitatively predict correct results. For TZ 3 also the new results predict problems with riser ducts 1 & 2. The temperature profile at the cross section of the first outlets (depicted in Figure 4.80) appears to be similar to the previous result.

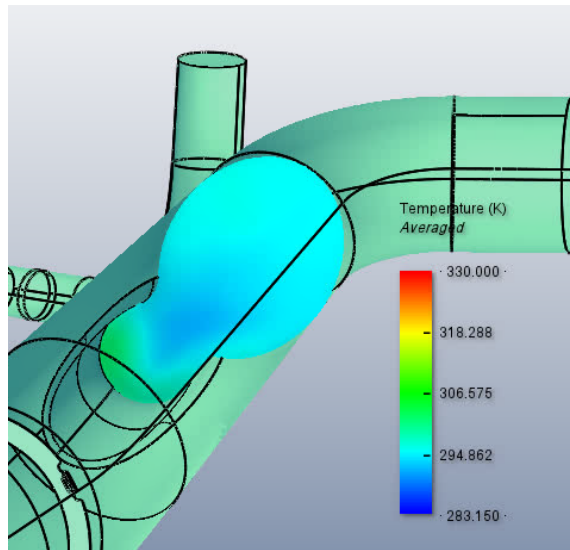


Figure 4.80: Average temperature at the cross section of the first riser ducts for TZ3 with the automatic wall function and without pressure fluctuations.

The actual temperatures vary from the previous results. The average temperature of all riser ducts is 294 K, compared to 296 K for the previous results and 294 K theoretical mixing temperature. The predicted sensor temperature now is 299 K, compared to 303 K before. So actually here, the difference between the two simulations is not that big.

Finally, the average temperature profiles for the riser ducts are depicted in the following figure. There is a temperature difference of more than 8 K between the hottest and the coolest riser duct.

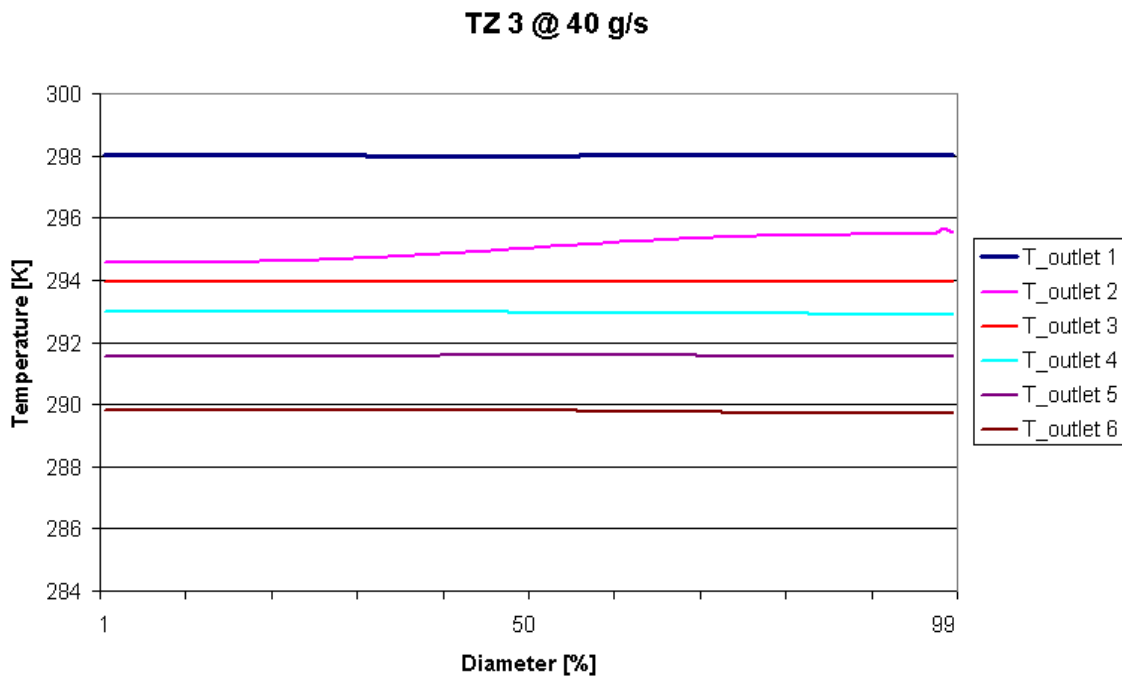


Figure 4.81: Average temperature profiles for the riser ducts of TZ 3 without pressure fluctuations.

TZ 4 @ 60 g/s

For the mass flow of 60 g/s the arising mixing temperature is 300 K. There is an average temperature of 305 K over all riser ducts and the sensor temperature gets pretty close with 305 K. The fact that for this simulation the maximum deviation between the hottest and coolest riser duct is only 0.6 K supports the previous results which predict no problems for this zone.

The wall temperature appears to be quite similar the the previous result but for the riser ducts even more uniform temperature profiles appear as Figure 4.82 shows.

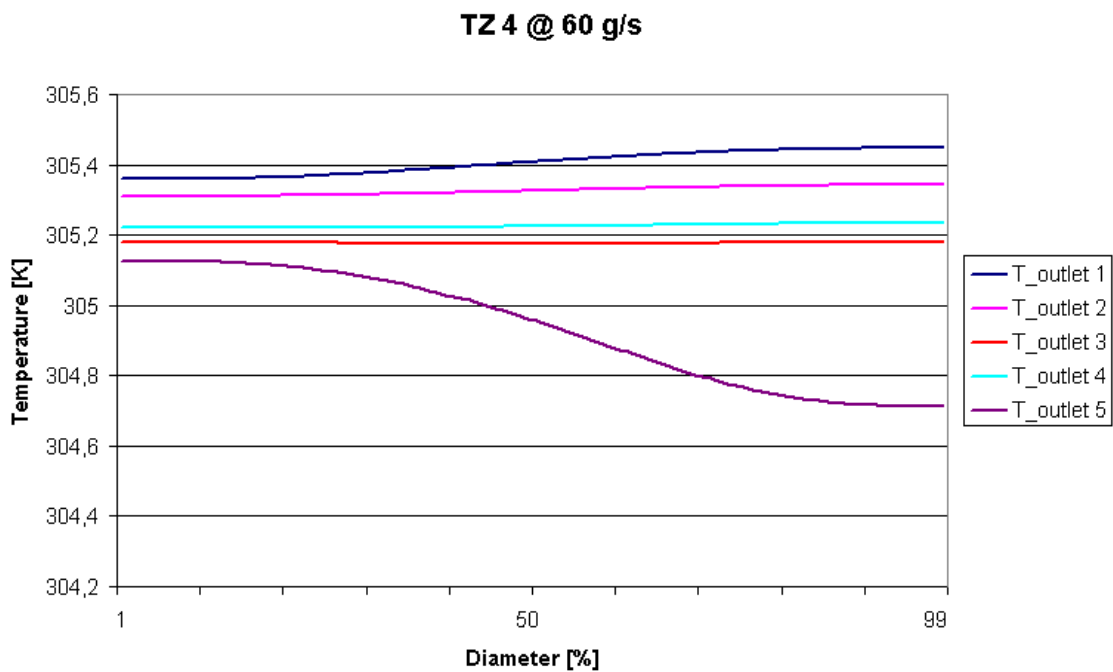


Figure 4.82: Temperature profiles at the riser ducts of TZ 4 for the automatic (equilibrium wall-function) wall model.

F/D @ 15 g/s

For the new setup at lower resolution and with the automatic wall model the temperature profile which was depicted in Figure 4.72 earlier, appears totally different as the following figure shows.

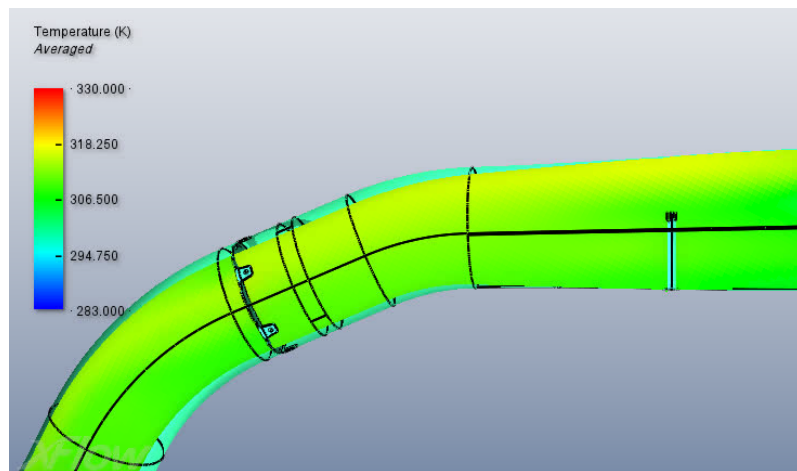


Figure 4.83: Average temperature at the longitudinal sensor cross section for the automatic wall model.

In order to investigate the influence of the decreased resolution, another simulation is launched with the original setting from previous simulations but on a uniform resolution of 0.01 m. Surprisingly, the temperature profile now appears to be similar to the one with the automatic wall model. It seems that the change of the temperature field is mainly caused by the coarse resolution. Figure 4.84 shows the temperature profile for the original case with coarse resolution.

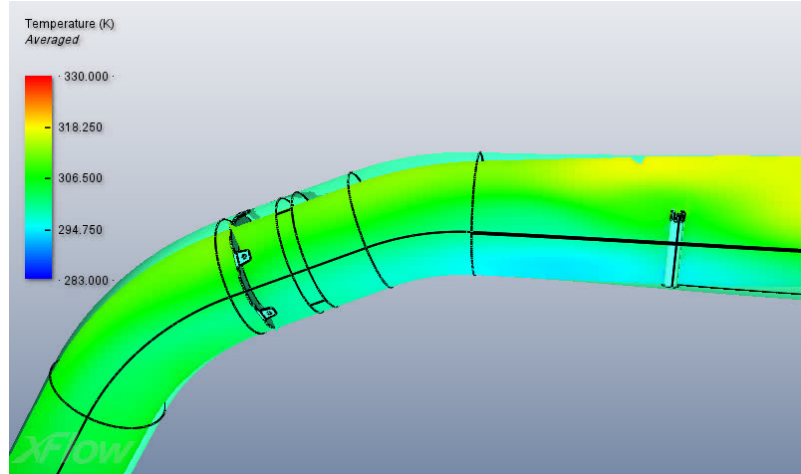


Figure 4.84: Average temperature at the longitudinal sensor cross section for the original case with a coarse resolution of 0.01 m.

Quantitatively, the following table depicts the differences between the three cases. Obviously, by comparing Figures 4.72, 4.83 and 4.84, in the last two figures, the hot air is mixed within a shorter distance compared to the original case. Table 4.13 shows that the outlet temperature remains constant but the sensor temperature varies widely.

To decide which results to trust, one last simulation (called “F/D auto-fine”) with a fine resolution of 0.0025 m through the whole domain is launched. The result can also be found in the table below.

Table 7: Results of the automatic wall function for comparison to the previous results.

| | Average outlet temperature | Average sensor temperature | Sensor temperature deviation | Theoretical temperature |
|-----------------|----------------------------|----------------------------|------------------------------|-------------------------|
| TZ 3 auto-wall | 293.5 | 299.0 | 4.7 | 294.3 |
| TZ 4 auto-wall | 305.0 | 304.8 | 5.2 | 299.6 |
| F/D original | 308.1 | 296.4 | -6.1 | 302.5 |
| F/D orig-coarse | 308.1 | 303.3 | 0.8 | 302.5 |
| F/D auto-wall | 308.5 | 306.8 | 4.3 | 302.5 |
| F/D auto-fine | 308.0 | 310.1 | 7.6 | 302.5 |

Figure 4.85 depicts the average temperature at the sensor cross section. Unluckily, the temperature profile for the fine case appears to be different from other cases, as the hot stream remains now attached to the bottom wall. Nevertheless, one can state that the automatic wall function leads to better thermal mixing compared to previous results of the non-equilibrium enhanced wall-function.

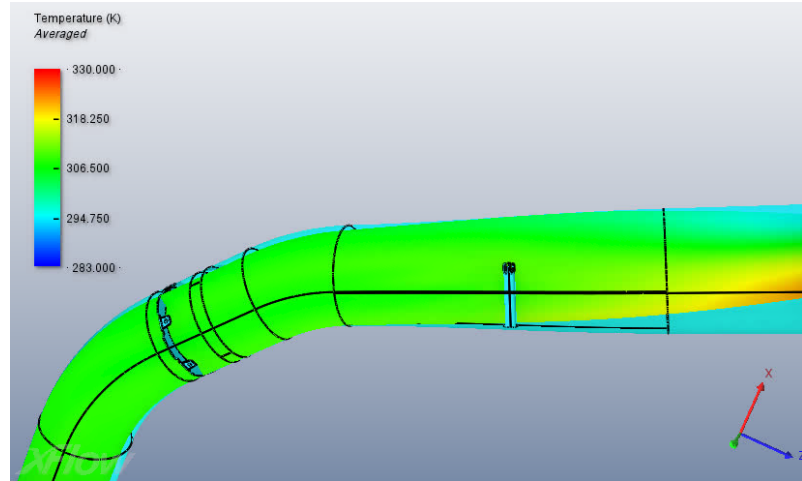


Figure 4.85: Average temperature at the longitudinal sensor cross section for the fine resolution with automatic wall model.

5 Discussion

Interpreting simulation data which obviously show numerical problems is a critical task. The results of the incompressible simulations of the T-junction investigation comply very well with experimental data and the results from the literature (note that for this case the operating fluid is water). But for the compressible flow in the TCS the setup for the incompressible case leads to numerical problems. There is a need for further research in the future in order to quantify the influence of the pressure fluctuations and to be able to interpret the results for the cases which could not be simulated with the proper simulation setup. The author was in contact with the development department of XFLOW and towards the end of the project a new version (2013, build 90.0) was coming up with a new parameter that should bring further improvements on this issue.

When monitoring the results one has to consider that those have to be taken with care. Unless, the influence of the pressure fluctuations on the temperature field is known one may not expect to have proper results. It is very likely that trends are predicted properly but one has to be careful with interpreting results quantitatively. In the very last results subsection where the F/D is simulated with the appropriate wall model and different resolutions, it turns out that the coarse resolution which was also used for the cases with automatic wall function for TZ 3 and 4 also causes big deviations from the previous results. In the end, more time was necessary to investigate this in detail.

Nevertheless, also the results of STAR-CCM+ which are depicted in Tables 5 & 6 predict big deviations of the sensor temperature with respect to the theoretical mixing temperature. Though, it is surprising that the sensor temperature predicted by XFLOW mainly tends to be above the average mixing temperature although the trim flow makes only a few percent of the main flow. These deviations appear especially in zones where the mixing distance to the sensor is rather short, like in TZ 5, TZ 6, TZ 7 and CCRC. So one could again state that the trend is predicted properly but one has to be careful when looking at the actual temperatures.

The restrictor has shown to have positive impact on thermal mixing (see Figure 4.39 of TZ 1). This is why it is recommended to move the restrictor upstream the sensor whenever this is possible in order to increase the mixing efficiency.

The mixing devices which were simulated have shown positive impact on the mixing process but implementing an external product like the Oxynator (©Air Liquide) seems promising in terms of simplicity and efficiency. With this mixing device probably most mixing problems would be solved. Until the end of the internship the company Air Liquide did not provide the author with more detailed information about the Oxynator.

Unluckily, because of the pressure fluctuations, it was not possible to determine the total pressure loss which of course is an interesting figure, especially when investigating mixing devices.

6 Summary and Outlook

To sum up the results, there is to say, that the simulations predict problems for the zones with short mixing distances (TZ 5, 6 ,7 & CCRC) and also for TZ 3, where the outlet for the first two riser ducts is located badly. The simulations of the mixing device have predicted the expected improvement of thermal mixing but the actual total pressure loss could not be evaluated because of the pressure fluctuations.

In the future all zones need to be reinvestigated with the automatic wall model. Also, it would be interesting to investigate the impact of the new “characteristic relaxation time” parameter from XFLOW build 90.0 on the pressure fluctuations.

Another uncertainty is the compatibility of XFLOW with the cluster. There is a need to do some further research why the software did not work out on the Uranus cluster which was intended to be used for this purpose. It worked out on another cluster but probably there is a general compatibility issue which is not known yet.

It will be necessary to do some further research on the mixing unit; whether the custom mixing unit which was simulated in XFLOW or the Oxynator by Air Liquide is more efficient.

All in all, the author is not fully satisfied with the results because they have to be considered non-credible. The lack of time in the end did not allow the author to finalize all zones with the latest outcome of the automatic wall model. But still, the author could show that there are some problematic zones which need to be reconsidered and some recommendations for improvements based on these investigations can be drawn.

References/Bibliography

Air Liquide, [web site], URL: <http://www.airliquide.com/en/oil-gas/equipment-11/the-gas-mixing-system-oxynator.html>, [cited 05.08.2013].

Bhatnagar, P.L., Gross, E.P. and Krook, M., "A Model for Collision Processes in Gases. I. Small Amplitude Processes in Charged and Neutral One-Component Systems" Physical Review Letters, Vol. 94, No. 3, 1954.

Frank, T., Adlakha, M., Lifante, C., Prasser, H.M. and Menter, F., "Simulation of Turbulent and Thermal Mixing in T-Junctions Using URANS and Scale-Resolving Turbulence Models in ANSYS CFX", ETH Zürich & ANSYS Germany GmbH, 2009.

Frisch, U., Hasslacher, B. and Pomeau, Y., "Lattice Gas Automata for the Navier-Stokes Equations", Physical Review Letters, Vol. 56, No. 14, 1986.

Hirota, M., Kuroki, M., Nakayama, H., Asano, H. and Hirayama, S., "Promotion of Turbulent Thermal Mixing of Hot and Cold Airflows in T-junction", Flow Turbulence and Combustion, Vol. 81, No. 1-2, July 2008, pp. 321-336.

Hussein, M. A., "On the Theoretical and Numerical Development of lattice Boltzmann Models for Biotechnology and its Applications", Dissertation, Munich, Germany, 2010.

Klören, D. and Laurien, E., "Large-Eddy Simulations of Stratified and Non-stratified T-junction Mixing Flows", High Performance Computing in Science and Engineering, 2013, pp. 311-324.

Mohamad, A. A., "Lattice Boltzmann Method", Springer, Calgary, Canada, 2011.

Scholarpedia, [web site], URL: http://www.scholarpedia.org/article/Lattice_Boltzmann_Method [cited 05.06.2013].

Succi, S., *The Lattice Boltzmann Equation for Fluid Dynamics and Beyond*, Clarendon Press, Oxford, 2001.

Wolf-Gladrow, D. A., *Lattice-Gas Cellular Automata and Lattice Boltzmann Models - An Introduction*, Springer, Berlin, Germany, 2005.

XFLOW User Guide, Next Limit Technologies SL, Madrid, Spain, 2013.